

TRACING THE MOVEMENT AND STORAGE OF MAGMA IN THE CRUST THROUGH  
SEISMOLOGY: EXAMPLES FROM ALASKA AND WESTERN MEXICO

by

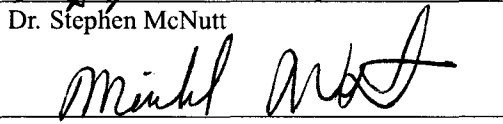
Matthew D. Gardine

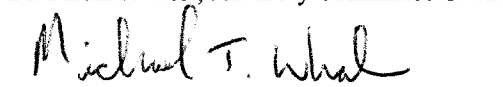
RECOMMENDED:

  
Dr. Douglas Christensen

  
Dr. Jonathan Dehn

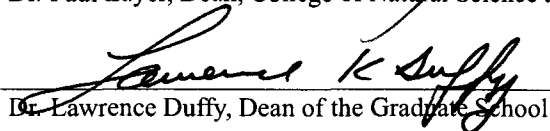
  
Dr. Stephen McNutt

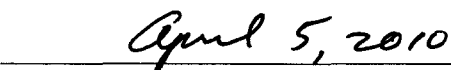
  
Dr. Michael West, Advisory Committee Chair

  
Dr. Michael Whalen, Chair, Department of Geology and Geophysics

APPROVED:

  
Dr. Paul Layer, Dean, College of Natural Science and Mathematics

  
Dr. Lawrence Duffy, Dean of the Graduate School

  
Date



TRACING THE MOVEMENT AND STORAGE OF MAGMA IN THE CRUST THROUGH  
SEISMOLOGY: EXAMPLES FROM ALASKA AND WESTERN MEXICO

A  
THESIS

Presented to the Faculty  
of the University of Alaska Fairbanks

in Partial Fulfillment of the Requirements

for the Degree of

DOCTOR OF PHILOSOPHY

By

Matthew D. Gardine, B.S.

Fairbanks, Alaska

May 2010

UMI Number: 3421520

All rights reserved

**INFORMATION TO ALL USERS**

The quality of this reproduction is dependent upon the quality of the copy submitted.

In the unlikely event that the author did not send a complete manuscript and there are missing pages, these will be noted. Also, if material had to be removed, a note will indicate the deletion.



UMI 3421520

Copyright 2010 by ProQuest LLC.

All rights reserved. This edition of the work is protected against unauthorized copying under Title 17, United States Code.



ProQuest LLC  
789 East Eisenhower Parkway  
P.O. Box 1346  
Ann Arbor, MI 48106-1346

## Abstract

Four studies are presented that examine magma movement and storage in the crust using seismology at three different volcanoes: Fourpeaked volcano in the Cook Inlet region of Alaska, Parícutin volcano in the Michoacán-Guanajato volcanic field in western Mexico, and Colima volcano at the western edge of the Trans-Mexican Volcanic Belt. In 2006, Fourpeaked volcano, Alaska, had a widely-observed phreatic eruption. A modest seismic network was installed in stages following the unrest. The eruption was followed by several months of sustained seismicity punctuated by vigorous swarms and SO<sub>2</sub> emissions exceeding a thousand tons/day. Based on the history of Fourpeaked, and observations during and after the phreatic eruption, it is proposed that the activity was caused by a modest injection of new magma beneath the volcano. Also presented are a series of studies from western Mexico, an area of high seismic and volcanic activity. A description of the creation of an automatically generated regional catalog of seismic activity is presented, along with a comparison with existing seismicity studies of the area. From this catalog, a swarm of earthquakes near Parícutin in May-June 2006 was discovered. This swarm demonstrated a steady upward migration in depth with time. Focal mechanisms during the first part of the swarm reflect the increased stress caused by dike inflation. In early June, the stress orientation changed and became more consistent with the inflation of a horizontal sill-like structure. At Colima volcano, a P-wave tomographic inversion using arrivals from 299 regional earthquakes is presented. The results of the inversion show two distinct low-velocity zones. One is in the upper 10 km under the volcano and may be caused by a magma chamber-type structure. The second anomaly, with peak values of 2.5% slower velocities, was imaged in the crust southeast of the volcano at depths of 15-30 km. This body may be due to partial melt and increased temperatures from a second, deeper area of magma storage.

## Table of Contents

	Page
<b>Signature Page</b> . . . . .	<b>i</b>
<b>Title Page</b> . . . . .	<b>ii</b>
<b>Abstract</b> . . . . .	<b>iii</b>
<b>Table of Contents</b> . . . . .	<b>iv</b>
<b>List of Figures</b> . . . . .	<b>vii</b>
<b>List of Tables</b> . . . . .	<b>x</b>
<b>Acknowledgments</b> . . . . .	<b>xi</b>
<b>Chapter 1: Using seismic data to trace the movement of magma</b> . . . . .	<b>1</b>
1.1 Introduction . . . . .	1
1.2 Chapter Overviews . . . . .	1
1.2.1 Chapter 2 . . . . .	1
1.2.2 Chapter 3 . . . . .	2
1.2.3 Chapter 4 . . . . .	2
1.2.4 Chapter 5 . . . . .	2
1.2.5 Chapter 6 . . . . .	3
<b>Chapter 2: Evidence of magma intrusion at Fourpeaked Volcano, Alaska in 2006-2007           from volcanic gases and a rapid-response seismic network</b> . . . . .	<b>4</b>
2.1 Abstract . . . . .	4
2.2 Introduction . . . . .	4
2.3 Earthquakes . . . . .	6
2.4 Earthquake Swarms . . . . .	9
2.4.1 Swarm I - September 17, 2006 . . . . .	9
2.4.2 Swarm II - October 3, 2006 . . . . .	9

2.4.3	Swarm III - November 5, 2006 . . . . .	11
2.4.4	Swarm IV - January 10, 2007 . . . . .	11
2.4.5	Swarm Comparison . . . . .	12
2.5	Gas Emissions . . . . .	14
2.6	Results of Gas Monitoring . . . . .	15
2.7	Interpretation . . . . .	16
2.8	Conclusions . . . . .	22
	References . . . . .	24
 <b>Chapter 3: Seismic data from western Mexico from February 2006 - May 2007 . . . . .</b>		<b>27</b>
3.1	Introduction . . . . .	27
3.2	Data . . . . .	27
3.3	Earthquake Catalog . . . . .	30
3.4	Catalog Analysis . . . . .	40
3.5	Tectonic Comparison . . . . .	41
3.6	Velocity Model Analysis . . . . .	41
	References . . . . .	49
3.A	Appendix . . . . .	50
 <b>Chapter 4: Dike emplacement near Parícutin volcano, Mexico in 2006 . . . . .</b>		<b>55</b>
4.1	Abstract . . . . .	55
4.2	Introduction . . . . .	55
4.3	Geologic Setting . . . . .	57
4.4	Data . . . . .	57
4.5	Hypocenter Analysis . . . . .	61
4.6	Stress Patterns . . . . .	62
4.7	Interpretation and Discussion . . . . .	66
4.8	Conclusion . . . . .	69
	References . . . . .	71

<b>Chapter 5: P-wave velocity structure of the deep crust under Colima volcano, Mexico: evidence of secondary magma storage . . . . .</b>	<b>74</b>
5.1 Abstract . . . . .	74
5.2 Introduction . . . . .	74
5.3 Geologic and Tectonic Background . . . . .	75
5.4 Data . . . . .	78
5.5 Method . . . . .	81
5.6 Model analysis . . . . .	89
5.7 Results . . . . .	89
5.8 Discussion and Conclusions . . . . .	101
5.8.1 Upper crust results . . . . .	101
5.8.2 Lower crust results . . . . .	103
References . . . . .	108
<b>Chapter 6: Summary and concluding remarks . . . . .</b>	<b>113</b>
6.1 Summary . . . . .	113
6.2 Concluding Remarks . . . . .	114

## List of Figures

	Page
2.1 A regional map of selected seismic stations and volcanoes around Fourpeaked . . .	5
2.2 A timeline of events at Fourpeaked . . . . .	7
2.3 A record section of a representative earthquake at Fourpeaked . . . . .	8
2.4 A map of earthquake epicenters showing formal one standard-deviation error ellipses	10
2.5 A summary of the seismic network performance . . . . .	12
2.6 The size of each seismic swarm with different network configurations . . . . .	13
2.7 Histogram of earthquakes located by routine AVO processing from September 2006 through October 2007 . . . . .	18
2.8 Earthquake epicenters before and after double-difference relocation . . . . .	22
3.1 A map showing CODEX (red) and MARS (blue) seismic stations deployed in west- ern Mexico from 2006-2008. . . . .	28
3.2 A zoom-in of Figure 3.1 showing CODEX stations (red circles) . . . . .	29
3.3 An epicenter map with cross-sections through the Provcats-B catalog . . . . .	33
3.4 A histogram showing the distance between a manually located earthquake and its matching automatically located earthquake . . . . .	34
3.5 An example of an automatically located slab earthquake . . . . .	35
3.6 An example of an automatically located crustal earthquake . . . . .	36
3.7 An example of an mislocated earthquake . . . . .	37
3.8 A reduced travel time curve for the automated event catalog . . . . .	38
3.9 A reduced travel time curve for the two-month manually located event catalog . . .	39
3.10 Location errors for earthquakes in the automated catalog . . . . .	42
3.11 A histogram of the strike of the semi-major axis of the location error ellipses . . . .	43
3.12 A map showing notable large thrust earthquakes in western Mexico . . . . .	44
3.13 An epicenter map showing seismicity of western Mexico . . . . .	45
3.14 A conceptual diagram showing the 3-D grid used for creation of the velocity model	46
4.1 A map of MARS and CODEX seismic stations near Parícutin in western Mexico . .	58

4.2	A map showing the original and double-difference relocated epicenters . . . . .	59
4.3	A histogram showing the number of located events per day associated with the swarm	60
4.4	Waveforms showing P-wave arrivals from two seismic stations: MA18 and MA53 .	63
4.5	Epicentral distance of the relocated earthquakes along the strike of the swarm with time (circles) . . . . .	64
4.6	A map showing relocated epicenters for 56 earthquakes with focal mechanisms . .	65
4.7	Stress tensor inversion results . . . . .	67
4.8	Conceptual model of the propagating dike with time (top) and the relocated hypocen- ters with time (bottom) . . . . .	68
5.1	Conceptual model of a hot zone . . . . .	76
5.2	Simplified tectonic map of western Mexico . . . . .	77
5.3	A map showing CODEX (red) and MARS (blue) seismic stations deployed in west- ern Mexico from 2006-2008 . . . . .	79
5.4	A zoom-in of Figure 5.3 showing CODEX stations (red circles) . . . . .	80
5.5	Ray paths for four slab earthquakes recorded on CODEX stations . . . . .	82
5.6	Epicenter map showing earthquakes used for the tomographic inversion . . . . .	83
5.7	Conceptual cartoon showing a discretized tomographic model . . . . .	84
5.8	The initial 1-D starting velocity model used for the inversion . . . . .	86
5.9	Ray hit count plot at various depth slices of the model . . . . .	86
5.10	A histogram showing arrivals recorded at each CODEX station . . . . .	87
5.11	Velocity model norm versus travel time residual variance for selected damping values	88
5.12	RMS travel time residuals for each iteration of the inversion . . . . .	89
5.13	Velocity model cross-sections running south-north . . . . .	90
5.14	Velocity model cross-sections running south-north, continued . . . . .	91
5.15	Velocity model cross-sections running west-east . . . . .	92
5.16	Velocity model cross-sections running west-east, continued . . . . .	93
5.17	Velocity model depth slices . . . . .	94
5.18	Velocity model depth slices, continued . . . . .	95
5.19	A histogram showing velocity change in the model after the inversion . . . . .	96
5.20	A histogram showing velocity change separated by depth . . . . .	97

5.21	A histogram showing velocity change separated by dense grid vs. sparse grid . . . . .	98
5.22	The P-wave velocity model from local earthquake tomography . . . . .	99
5.23	A checkerboard resolution test . . . . .	100
5.24	A resolution test for a rectangular anomaly in the lower crust . . . . .	102
5.25	The -1.5% velocity deviation isosurface plot from the tomography results . . . . .	103
5.26	A thermal model profile of the Colima-Jalisco subduction zone . . . . .	105
5.27	P-wave velocities mapped in terms of temperatures at 25 km depth . . . . .	106

**List of Tables**

	Page
2.1 Key parameters of each earthquake swarm . . . . .	9
2.2 Normalized swarm comparison . . . . .	14
2.3 Collected SO <sub>2</sub> data . . . . .	16
3.1 1-D velocity model for southern Alaska . . . . .	31
3.2 Best-fitting 1-D velocity model for western Mexico . . . . .	48
4.1 1-D velocity model for western Mexico derived from travel-time inversions . . . . .	62

## Acknowledgments

I would like to acknowledge the many people without whose help this thesis would not have been completed.

I would like to thank my advisory committee for their guidance, input, and expertise. In particular, Mike West provided an open door and an interested ear. He gave me every opportunity possible, both in the office and in the field, to help me succeed in my academic career. Doug Christensen, Jon Dehn, and Steve McNutt provided helpful alternative views and insight when needed.

I would also like to acknowledge the folks at the Colima Volcano Observatory, in particular Tonatiuh Dominguez and Nick Varley. Tonatiuh was the driving force behind the CODEX project; without his tireless and never-ending help, none of the work would have come to fruition. Nick provided additional help and logistical support, especially during my six-week stay in Colima in 2007.

Funding for my work was provided by the Geophysical Institute, the Alaska Volcano Observatory, and the National Science Foundation. Bill Menke at Columbia University provided the tomography code that was the backbone of my work at Colima.

Finally, I would like to dedicate this thesis to my family. My parents, Randy and Debi, gave me the support and encouragement to follow my dreams, even if that meant five years of graduate school, 4000 miles from home. My wonderful wife Lea gave me the strength to succeed, the motivation to graduate, and was a darned good manuscript editor. Without any of them, I could not have gotten to where I am today.

## **Chapter 1: Using seismic data to trace the movement of magma**

### 1.1 Introduction

Studying how magma interacts with the crust is a field of intense interest from both a volcano monitoring perspective as well as from a research perspective. By better understanding how and where magma moves through and is stored in the crust, the community as a whole can benefit from the increased ability to predict volcanic eruptions and better utilize geothermal energy. There is also a fundamental question as to why volcanoes occur precisely where they do. Tectonically, volcanoes are expected at subduction zones, as subducting slabs serpentinize and form partial melt in the mantle wedge. However, why magma moves in the way that it does from the mantle wedge to the surface is still an open question in volcanology.

This thesis details studies at three different volcanoes, each study looking at magma interaction at different depths in the crust. At Fourpeaked volcano in Alaska, the magma nearly breached the surface, and was shallow enough to release large amounts of volcanic gases into the atmosphere. At Parícutin volcano, Mexico, the magma stayed in the upper 10 km of the crust, but stalled before any surface manifestations could be observed. While Colima volcano, Mexico, is highly active, the deep crust was examined using seismic tomography, combined with petrological and thermal data, for evidence of lower crustal influence in the long-term eruptive activity of the volcano.

### 1.2 Chapter Overviews

#### 1.2.1 Chapter 2

A series of unexpected volcanic events occurred at Fourpeaked volcano, Alaska in September through January 2006-2007. A large gas plume, accompanied by a swarm of 17 locatable earthquakes, occurred on September 17, 2006. Degassing, along with four distinct swarms of earthquakes, continued over the next eight months. Chapter 2 examined the seismicity associated with these four swarms and analyzed how a changing, ad-hoc seismic network influenced the Alaska Volcano Observatory's (AVO) ability to detect and locate earthquakes at a previously unmonitored volcano. Additionally, SO<sub>2</sub> and CO<sub>2</sub> data were collected and, combined with the seismicity, used to conclude that the unrest at Fourpeaked was most likely caused by a small injection of new magma

into the shallow crust under the volcano.

### 1.2.2 Chapter 3

The use of earthquake catalogs is often a necessary requirement to doing many seismic analyses. However, the creation of these catalogs is usually not done by the researcher, but instead by other organizations or analysts. Chapter 3 describes a methodology whereby a catalog of over 4500 local and regional earthquakes was created using data from deployments of two temporary seismic networks in western Mexico from February 2006 - May 2007. After an initial setup described in the chapter, the entire process of detecting seismic phase arrivals, generating earthquake locations using the arrivals, and catalog database creation was completely autonomous, without any user intervention, and using less than 100 hours of CPU time.

### 1.2.3 Chapter 4

Following the creation of the catalog of earthquakes in western Mexico, a large number of earthquakes were observed originating near the Mexican volcano Parícutin in May and June 2006. Chapter 4 presents a study of the vigorous seismicity associated with the swarm. In particular, the hypocenters showed a striking, near linear, upward migration in time. By combining location data, focal mechanisms, and stress patterns, we conclude that the swarm was likely caused by an intrusion of magma into a dike. This intrusion stalled around 5 km depth, and proceeded to move into one or more possible sill-type structures at that depth.

### 1.2.4 Chapter 5

Slab events and selected crustal earthquakes were extracted from the earthquake catalog created in Chapter 3. These 299 events, consisting of 8660 P-wave arrivals, were used to invert for the velocity structure of the lower crust under Colima volcano. The resulting images highlight a low-velocity zone, with a peak anomaly of 2.5% slower velocity from 15-30 km deep, to the southeast of the volcano. This anomaly is interpreted to be a zone of secondary magma storage, an interpretation consistent with existing petrological models of the volcano.

### 1.2.5 Chapter 6

Chapter 6 is a summary of work presented in this thesis. The studies presented here represent how seismic networks of different sizes and purposes can be used to detect and interpret magmatic signals in various length scales in the crust, from the shallow near-surface to the Moho.

## **Chapter 2: Evidence of magma intrusion at Fourpeaked Volcano, Alaska in 2006-2007 from volcanic gases and a rapid-response seismic network<sup>1</sup>**

### 2.1 Abstract

On September 17th, 2006, Fourpeaked volcano had a widely-observed phreatic eruption. At the time, Fourpeaked was an unmonitored volcano with no known Holocene activity. Airborne gas sampling began within days of the eruption and a modest seismic network was installed in stages. Vigorous steaming continued for months; however, there were no further eruptions similar in scale to the September 17 event. This eruption was followed by several months of sustained seismicity punctuated by vigorous swarms, and SO<sub>2</sub> emissions exceeding a thousand tons/day. Based on the history of Fourpeaked, and observations during and after the phreatic eruption, we propose that the activity was caused by a modest injection of new magma beneath Fourpeaked. Fourpeaked remained active over several months as this magma equilibrated into the crust. By early 2007 declining seismicity and SO<sub>2</sub> signaled the end of unrest. Because the Fourpeaked seismic network was installed in stages and the seismicity was punctuated by discrete swarms, we use Fourpeaked to illustrate quantitatively the efficacy and shortcomings of modest rapid response seismic networks for tracking volcanic earthquakes.

### 2.2 Introduction

Late on the evening of September 17, the Alaska Volcano Observatory (AVO) received reports of two ash and gas plumes reaching 6000 meters above sea level, coming from the area around Fourpeaked volcano, approximately 50 kilometers northeast of the Katmai volcanic complex and 350 kilometers southwest of Anchorage. The bulk of these reports came from Homer, Alaska, located 150 km northeast of Fourpeaked. Photographs and satellite imagery suggested the origin of the two plumes to be near the summit of Fourpeaked (Neal et al., 2009). At the time, no seismic network or geophysical monitoring regimen existed for Fourpeaked. As a result, no seismic activity was initially detected. Knowledge of the geologic and eruptive history of the area is limited and

---

<sup>1</sup>Gardine, M., West M., Werner C., Doukas, M., In Review. Evidence of magma intrusion at Fourpeaked Volcano, Alaska in 2006-2007 from volcanic gases and a rapid-response seismic network, *Journal of Volcanology and Geothermal Research*.

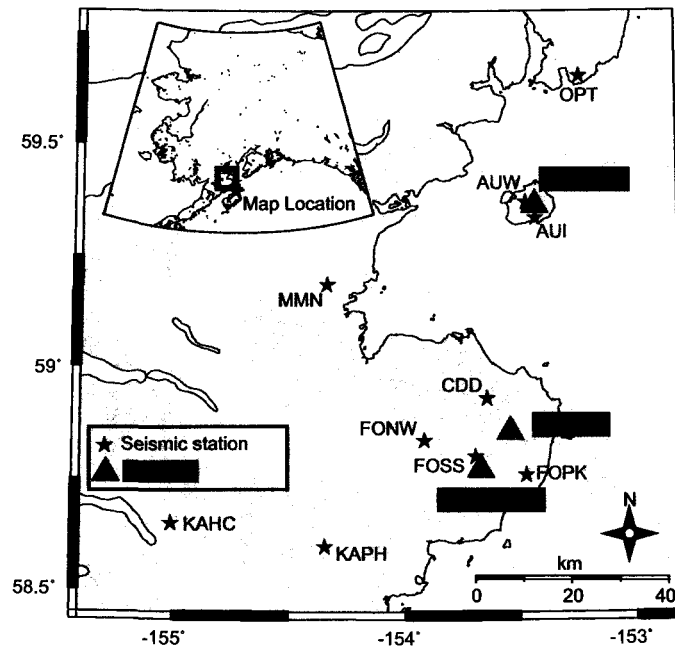


Figure 2.1: A regional map of selected seismic stations and volcanoes around Fourpeaked. The seismic stations shown are those that existed as of May 1, 2007, and were used in locating earthquakes at Fourpeaked.

there is no evidence of Holocene activity. Most of the volcano is covered by the Fourpeaked glacier, exposing only isolated outcrops, predominately of andesitic lavas (Kienle and Swanson, 1983).

Following the plume reports, the limited seismic data in the region was scanned for evidence of any signals at the time of the plumes. The closest functioning seismic station was KAPH, located more than 35 km southwest of Fourpeaked (Figure 2.1). The retrospective analysis revealed numerous earthquakes near the time of the plumes. Seismic network coverage was too sparse for most of the events to be located. Rough locations could be determined for 17 of the largest earthquakes, the strongest having a local magnitude ( $M_L$ ) of 1.7. Though the locations were poorly constrained, they offered further confirmation that Fourpeaked (as opposed to nearby Douglas, 14 km away) had been the source of the plumes. The earthquake swarm demonstrated that direct seismic monitoring could be a valuable tool in on-going assessments of Fourpeaked. It was also clear that the distant seismic data would be of limited use if not augmented by closer stations. Over the next month, a rapid response effort established a basic seismic network at Fourpeaked.

During initial overflights on September 25, 2006, at least seven distinct ice craters were observed near the summit of Fourpeaked, aligned in a north-northwest trend (Neal et al., 2009). Subsequent overflights observed fumarolic activity that continued for months after the eruption.

Targeted volcanic gas measurement flights began within a week of the initial unrest at Fourpeaked and continued for the next eight months. Unlike the seismic data, the SO<sub>2</sub> measuring capabilities were robust from the start and provide a consistent temporal data stream throughout the unrest. The seismic and gas data are highly complementary. Earthquakes illuminate regions and timeframes of rapid stress adjustments beneath the volcano, while the gas data provide a bulk measure of volcanic emissions. Seismic and gas emissions remained elevated and tapered gradually over the ensuing year. Through comparisons of the seismicity with gas emissions over time, we hypothesize that a small magmatic intrusion occurred at Fourpeaked in September 2006.

The primary purpose of this paper is to investigate the trends in seismic and gas data from September 2006 through the middle of 2007 and seek explanations that fit with the observed activity. In addition, we provide a quantitative example of the gains that can be expected from a modest rapid response seismic deployment. Eruptions at poorly monitored volcanoes are commonplace; other recent examples include Chaitén (Carn et al., 2009) and Kasatochi (Adleman et al., 2008). In the early stages of any volcanic response, when hazards are being weighed against time and money, quantitative analogies can provide unbiased, easy to understand, examples of what should and shouldn't be expected from a rapid response effort. The Fourpeaked example is particularly illustrative. Because the seismic network was installed in stages, punctuated by earthquake swarms, it is possible to gauge the evolution of the network's detection/location capabilities in response to the seismic station upgrades.

### 2.3 Earthquakes

One week after the atmospheric plumes and initial earthquake swarm on September 17, AVO began installing a modest seismic network centered on Fourpeaked. Initial upgrades included a new seismic station (FOPK) 12 km to the east of the summit and the repair of an existing site (CDD) (Figure 2.1). On October 17, two additional seismic stations were installed 16 km to the west of the volcano (FONW) and 4 km northwest of the summit (FOSS) while a third site (MMN) was repaired. All new stations were vertical component short-period sensors with analog teleme-

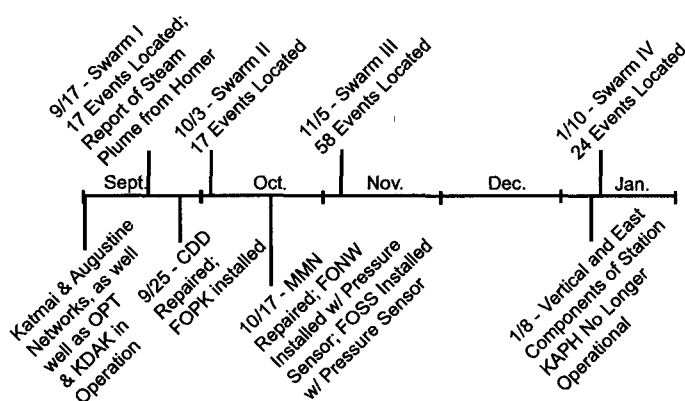


Figure 2.2: A timeline of events at Fourpeaked. Shown in the figure are dates of earthquake swarms (top) and dates of upgrades to the seismic network (bottom) in 2006-2007.

try. Stations FONW and FOSS were installed with co-located infrasound sensors. See timeline in Figure 2.2.

On October 3, a second notable earthquake swarm occurred. Because FOPK and CDD had been installed, it was possible to track seismicity with a reasonable ability to distinguish earthquakes at Fourpeaked from background seismicity in the region. Unlike September 17, this swarm was detected at the time of its occurrence. However the two final stations in the network, FONW and FOSS, had not yet been installed, so locations were still elusive for most earthquakes. Only four earthquakes in this swarm met the criteria for inclusion in AVO's analyst-reviewed earthquake catalog (Dixon et al., 2008).

Once the full network was in place in late October, AVO implemented automated earthquake triggering and routine earthquake location procedures for the Fourpeaked network. Two additional earthquake swarms occurred at Fourpeaked on November 5 and January 10. These swarms were recorded by the full network and each had several dozen locatable earthquakes.

In order to gauge the network performance during each stage of development, we needed a set of earthquakes located under standardized conditions. For each swarm, the continuous waveform data were scanned for events. Visual inspection of the continuous data removed the bias introduced by automated triggering algorithms, which were only implemented after the initial swarms. To be included in this catalog, P-wave arrivals were required on at least four stations accompanied by at

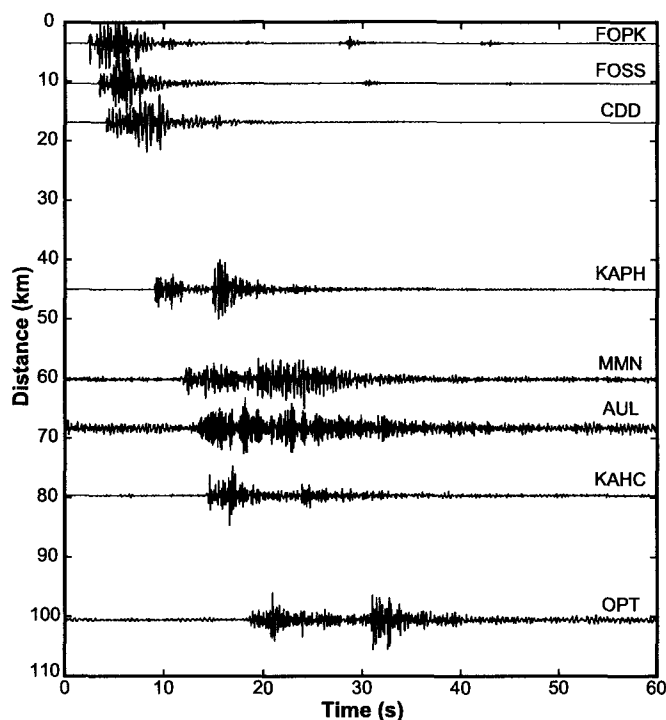


Figure 2.3: A record section of a representative earthquake at Fourpeaked. The event occurred on November 11, 2006 at 22:18:45 UTC. The data has been filtered using a 1-10 Hz. bandpass filter.

least one S-wave arrival (see Figure 2.3 for an example earthquake). P- and S-phases were picked by hand at each available station with pick errors assigned using standard, though subjective, analyst judgment. Earthquakes were located in a 1-D velocity model widely used for southern Alaska (Matumoto et al., 1968). All processing was carried out using the Antelope program suite (Boulder Real Time Technologies) using the dbgenloc package (Pavlis et al., 2004) for earthquake locations. We include all earthquakes with a location that converged in the Fourpeaked region, regardless of location error. A summary of the four swarms can be found in Table 2.1.

In addition to the custom earthquake catalogs developed for the four swarms, there is a separate catalog created through AVO's routine earthquake processing. After November 2006, this catalog is authoritative and self-consistent as detailed in Dixon et al. (2008). We use this catalog in our interpretation to constrain overall seismicity in the months following the Fourpeaked unrest.

Table 2.1: Key parameters of each earthquake swarm

Swarm	Date	Number of Located Events	Depth Range (km)	Magnitude Range ( $M_L$ )	Mean Horizontal Error (km)	Mean Depth Error (km)
I	Sept. 17, 2006	17	1-5	0.8-1.7	9.8	2.5
II	Oct. 3, 2006	17	1-5	1.0-1.4	8.3	2.8
III	Nov. 5, 2006	58	1-5	-0.2-1.7	0.6	0.03
IV	Jan. 10, 2007	24	1-5	0.7-1.7	0.2	0.01

## 2.4 Earthquake Swarms

### 2.4.1 Swarm I - September 17, 2006

The first located earthquake of swarm I occurred at 19:46 UTC on September 17, 2006, with activity tapering off four hours later. All of the 17 earthquakes that could be located used arrivals at stations at least 35 km away from the origins (mostly stations KAPH, KAHC, AUW, AUI and OPT), with the farthest arrivals from the IRIS-operated station KDAK on Kodiak Island, 130 km away. Epicenters of this swarm can be seen in Figure 2.4A, along with the one standard-deviation confidence error ellipses. The sizes of the errors reflect the poor station coverage. The errors have a strong northwest-southeast major axis which is a product of the lack of stations in these directions. The apparent skew in epicenters along this same strike is most likely a result of the location errors. Earthquake depths are very poorly constrained due to the lack of close stations. However, the presence of well-developed surface waves offers qualitative support for earthquake locations in the upper crust (Figure 2.3). All earthquakes in this swarm, and subsequent swarms, have high-frequency waveforms with impulsive P- and S-waves, typical of brittle failure earthquakes (McNutt, 2002). No long period events are observed. However this does not rule out their existence as long period earthquakes are rarely observed, and almost never located, using data from such distant stations.

### 2.4.2 Swarm II - October 3, 2006

Swarm II, on October 3, lasted a little less than four hours. The presence of two additional stations, CDD and FOPK, allowed a higher percentage of the earthquakes to be located. Roughly one-fifth of the earthquakes observed on the closest station, FOPK, could be located by the network. The 17 located events have marginally smaller errors than swarm I. A shift in the orientation of the

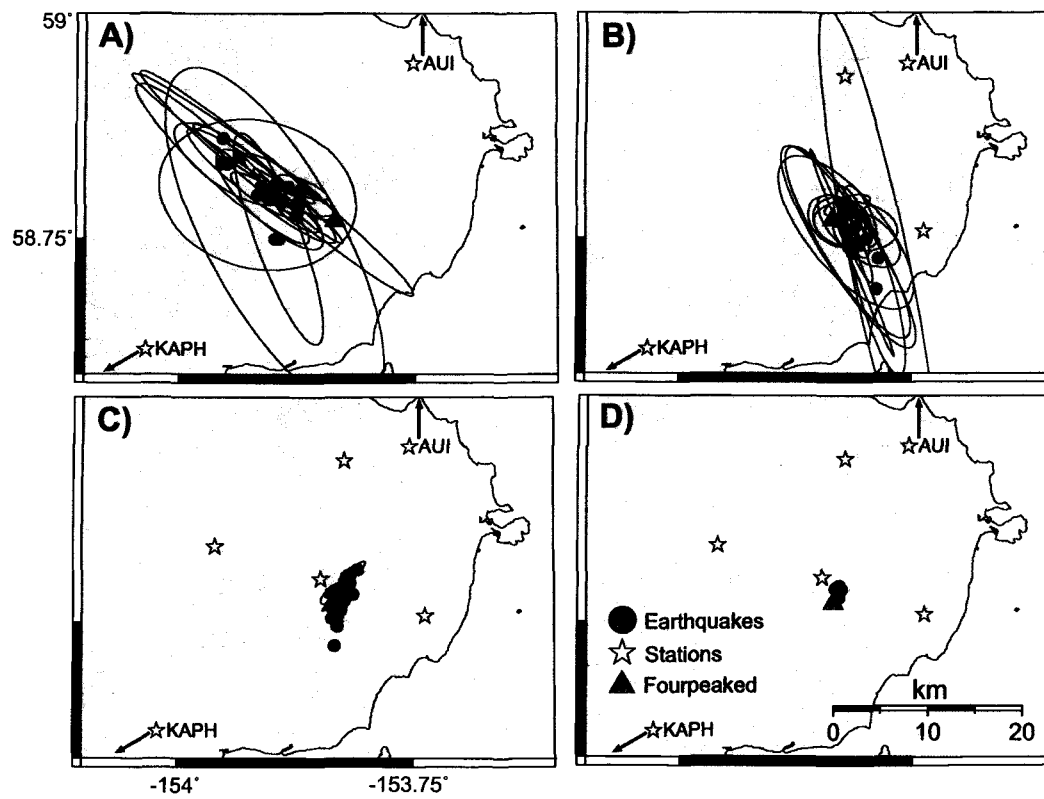


Figure 2.4: A map of earthquake epicenters showing formal one standard-deviation error ellipses. Included are epicenters for (A) swarm I (B) swarm II (C) swarm III and (D) swarm IV.

errors (Figure 2.4B) reflects the addition of two more seismic stations.

#### 2.4.3 Swarm III - November 5, 2006

The third notable swarm occurred on November 5 and had the largest number of located earthquakes of any of the swarms, with 58. The large number of located events is due, in part, to the installation of stations FONW and FOSS and the rehabilitation of station MMN. Figure 2.4C shows the epicenters and errors associated with this swarm. With two new stations, the errors were reduced by over half. This change is due to the fact that the stations now encompassed the volcano (Figure 2.4). Though the network was more complete, only half of the events observed at station FOPK could be located using our four-station minimum criteria. Despite good network geometry, station spacing remained sparse, and most of the stations were far from the source compared to typical volcano networks.

Swarm III had enough earthquakes to compute a magnitude of completeness. The magnitude of completeness is estimated as the minimum magnitude that fits the linear Gutenberg-Richter relationship between magnitude and the logarithm of the cumulative number of earthquakes (Stepp, 1972, Weimer and Wyss, 2000). Earthquakes above this magnitude are consistently detected and located, assuming the station coverage and background noise conditions of this time period. The magnitude of completeness for the array during swarm III is approximately 0.4. The background noise level during this swarm was low, making 0.4 a best-case estimate. This magnitude of completeness is near the median for volcano seismic networks in Alaska. The b-value for this swarm is 1.2, a value typical for tectonic earthquake swarms (Frolich and Davis, 1993), suggesting a common brittle failure source for the earthquakes. Given the lack of Holocene activity, we expect that the shallow crust is relatively cool. Cool crust would make volcano-tectonic (VT) earthquakes a likely accompaniment to any sort of deformation or magmatic injection.

#### 2.4.4 Swarm IV - January 10, 2007

Swarm IV occurred on January 10 and lasted approximately 2 hours. During this time, 24 earthquakes were located, with an additional 49 seen at FOPK that were not locatable. Prior to the swarm, station KAPH lost its vertical and east components. Nevertheless, some P-arrivals, typically seen best on the vertical component, were picked on the north component. Furthermore, station

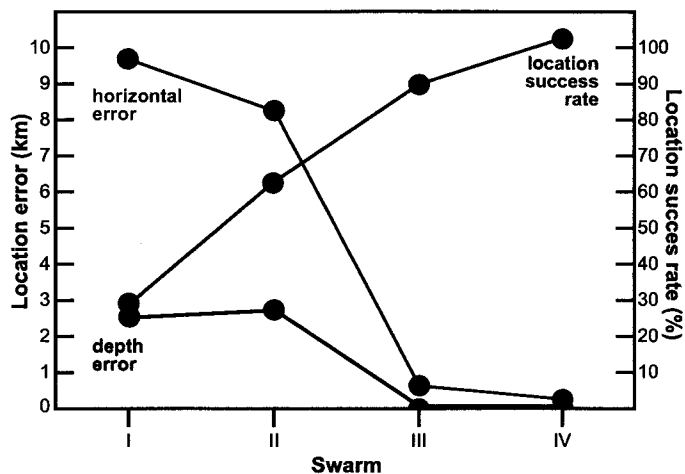


Figure 2.5: A summary of the seismic network performance. Location success rates, mean values for the semi-major axis of the one-standard deviation horizontal error ellipse, and mean depth errors are shown for each swarm.

FOSS, closest to the summit, showed an increase in background noise, making it harder to detect signals. As a result of these station problems, the ability to detect earthquakes meeting the minimum standards was compromised. However, because no stations were actually lost, the location errors remained roughly the same (Figure 2.4D).

#### 2.4.5 Swarm Comparison

The evolution of the seismic network at Fourpeaked can be broken into three time frames corresponding to the network configurations on September 17, October 3, and November 5. The objective is to assess the detection and location abilities of the network to provide an empirical example that can be used in the future when trying to predict the efficacy of a rapid response seismic installation, or even in general field planning.

The easiest metrics to compare are the mean horizontal and depth errors. These are shown in Figure 2.5. The major improvement in errors came with the addition of stations FONW and FOSS in mid-October. Station FONW eliminated the nearly 180 degree azimuthal gap that previously existed to the northwest of the volcano and dramatically reduced the formal horizontal location errors to less than 1 km. At the same time, station FOSS provided seismic arrivals from on top of the source region, which greatly reduced the depth error and the origin time error (not shown).

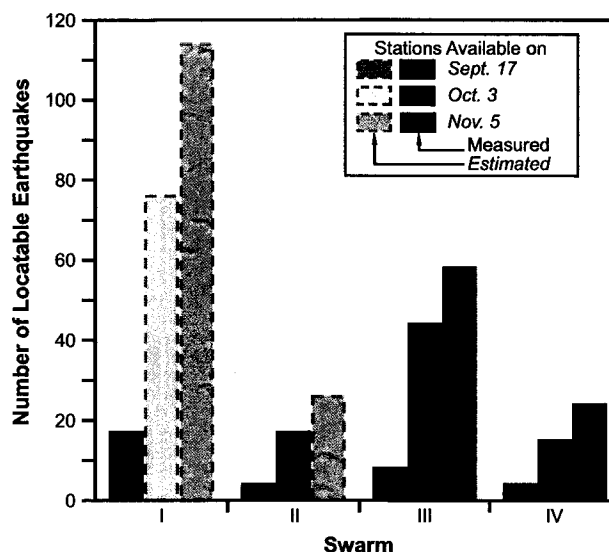


Figure 2.6: The size of each seismic with different network configurations. Measured and estimated number of locatable earthquakes for each swarm are shown based on the network configurations of September 17, October 3, and November 5. The dashed boxes indicate extrapolated values using the mean location success rate for the given network configuration.

In addition to location errors, we seek a measure for how well each network configuration accounts of the total number of earthquakes. One approach is to compare the number of earthquakes that can be located for each swarm using subsets of stations available at other times. For example, the November 5th network was able to locate 58 events during swarm III. Using the reduced network available on October 3rd, only 44 of these events would have been located. Similarly, if swarm III had occurred on September 17th, only 8 of the events would have been located (Table 2.2, Figure 2.6).

Because the network evolved piecemeal during the period of unrest, we cannot use the number of earthquakes to compare the size of the swarms directly. Instead, we normalize the size of the swarms using a parameter common to the entire dataset. For this parameter we use the number of S-wave arrivals observed on station KAPH. Station KAPH was the closest station in operation through the entire period of unrest at Fourpeaked. S-waves, which are recorded more clearly on horizontal components, are used because the vertical component of KAPH was compromised during swarm IV. For each swarm, we calculate the ratio of S-wave arrivals at KAPH to the number of locatable

Table 2.2: Normalized swarm comparison. The estimated number of locatable earthquakes based on the mean location rate for the given time period is denoted by a †. The location success rate is defined as the number of located earthquakes divided by the number of S-arrivals seen at KAPH. The September 17 location success rate for swarm I is not used in computing the mean location rate for September 17 stations due to a high background noise level at KAPH during the swarm.

Swarm	P-Arrivals at FOPK	S-Arrivals at KAPH	Number of Locatable Earthquakes (Location Success Rate)		
			Sept. 17	Oct. 3	Nov. 5
I	-	40	17 (43%)	76†	114†
II	84	28	4 (14%)	17 (61%)	26†
III	116	69	8 (17%)	44 (64%)	58 (84%)
IV	73	23	4 (12%)	15 (65%)	24 (104%)
Mean Location Rate			(14%)	(63%)	(94%)

earthquakes. We define this ratio as the earthquake "location success rate" (Table 2.2).

Using swarm III as an example, of the 69 S-waves observed at station KAPH, 58 were locatable. This gives a location success rate of 84%. There are several caveats to this analysis due to background noise, focal mechanisms and station performance. Nevertheless, it provides a rough quantitative basis for comparing the performance of different network configurations. We then use the location success rate multiplied by the number of S-picks on KAPH to estimate the number of events that would have been located in earlier swarms using the expanded network configurations (Table 2.2). The totals are shown in Figure 2.6. Faded bars are used to illustrate earthquakes counts that were not measured directly but rather estimated using the location success rates in Table 2.2. This retrospective interpretation assumes a similar b-value across the swarms. We cannot verify this assumption except to comment that the style and frequency of the waveforms changed little across the swarms, suggesting a consistent source type. Based on this analysis, swarm I was nearly twice the size of subsequent swarms. Swarm III was the next largest, while swarms II and IV were comparable at about one quarter the size of swarm I.

## 2.5 Gas Emissions

Two instruments were used to measure SO<sub>2</sub> emissions. First, a Barringer correlation spectrometer (COSPEC V) was used for measuring SO<sub>2</sub> column abundance from an airborne platform.

Typically, four to six traverses were flown under the downwind plume perpendicular to the direction of plume travel with the upward-looking COSPEC to measure an average column abundance of SO<sub>2</sub>. On a few occasions the plume was not accessible due to cloud cover and in these situations the instrument was pointed downward. On two occasions we were able to make measurements both above and below the plume, so that the two methodologies for making measurements could be compared (Table 2.3). In addition to COSPEC measurements, for two of the flights SO<sub>2</sub> concentrations were measured using an Interscan analyzer and the contour method. Using this technique, measurements were made at intervals of approximately 60 m up through the plume. CO<sub>2</sub> measurements were made on three days using a LICOR 6252 and the contouring method. In all measurements, a GPS receiver was used to mark the location each second. Details on the emission measurements and calculations can be found in McGee et al. (2001), and references therein. Wind circles were flown at the elevation of the plume to calculate the velocity of plume travel so that a SO<sub>2</sub> emission rate could be computed (Doukas, 2002).

## 2.6 Results of Gas Monitoring

SO<sub>2</sub> emissions were measured using upward-looking and/or downward looking techniques. Reliable SO<sub>2</sub> emissions were measured in both directions on September 23 and 30, 2006. Downward-looking measurements were made over a consistent ice-covered background and resulted in emission rates that were between 15-38% higher than upward looking COSPEC measurements. In the time series, upward measurements are reported when reliable (i.e. when flown beneath the plume and no SO<sub>2</sub> was detected on the Interscan instrument). If reliable upward-looking measurements were not available, the contoured SO<sub>2</sub> was used to estimate emissions. If both upward-looking and contouring data were not available due to difficult flying conditions, downward-looking measurements are reported, but are corrected for an average 25% overestimation due to the poorly constrained source path (Table 2.3). One week following the initial seismic swarm and eruption at Fourpeaked, gas emissions were high and variable (1620-2350 t/d SO<sub>2</sub> and 792 t/d CO<sub>2</sub> between Sept. 23 and 30, Table 2.3). Emissions remained at high levels following the second seismic swarm (approximately 1700 t/d on Oct. 12). By November, SO<sub>2</sub> emissions had dropped to 1200 t/d and CO<sub>2</sub> to near 600 t/d. By May 2007, after a slow, steady decline, emissions were both  $\leq 50$  t/d (Table 2.3).

Table 2.3: Collected SO<sub>2</sub> data. C-U=COSPEC upward-looking, C-D=COSPEC downward-looking, CN=contoured emission rate.

Date	Method	SO <sub>2</sub> (t/d)	Std. Dev	CO <sub>2</sub> (t/d)	C/S (molar)
Sept. 23, 2006	C-U	2350	330	792	0.49
Sept. 24, 2006	CN	1620	126	—	—
Sept. 30, 2006	C-U	2210	302	—	—
Oct. 12, 2006	C-D	1700	—	—	—
Nov. 4, 2006	C-D	1230	—	—	—
Nov. 18, 2006	CN	1000	—	595	0.87
Feb. 22, 2007	C-U	420	96	—	—
May 18, 2007	C-U	50	5	30	0.87

## 2.7 Interpretation

All indications point to the occurrence of a singular event on September 17, 2006. The 17th of September is the only time that large gas and/or ash plumes were observed thousands of feet above the volcano. Though most earthquakes in the September 17 swarm could not be located, the analysis in Section 2.4.5 demonstrates that it was considerably more vigorous than subsequent earthquake swarms. Though SO<sub>2</sub> output remained elevated for many months, the emission rate was at its maximum in September 2006 and showed a steady decrease to background levels in the 8 months that followed. Together, these observations demonstrate fairly unambiguously that on September 17th, 2006 a pathway through the shallow crust was opened rapidly allowing a large volume of gas, and limited ash (none juvenile, Neal et al., 2009), to quickly vent from the Fourpeaked system in a matter of hours. The seismicity of this (and all events at Fourpeaked) was volcano-tectonic in nature. Clear P- and S-waves, peak frequency contents between 5-15 Hz, a low b-value of 1.2, and variable waveforms suggest distributed brittle failure with a range of source mechanisms. This is quite consistent with the failure of shallow crustal rock required to open a pathway to the surface.

In the ensuing months, SO<sub>2</sub>, seismicity, and steaming remained elevated. There is no evidence of additional large phreatic explosions such as occurred on September 17. The seismicity is poorly constrained in the first month because the network was not yet in place. However, any swarms comparable in size to the first would likely have been observed. Additional seismic swarms did occur in October, November and January. These were less energetic than the first. Since a path to the surface already existed, phreatic activity would not necessarily have been accompanied by

significant seismicity.

The logistics of airborne SO<sub>2</sub> sampling precluded frequent sampling. It is possible that bursts of elevated SO<sub>2</sub> could have occurred in the days and weeks between sample points. This is particularly true in the two weeks following the eruption when SO<sub>2</sub> values illustrate some variability. The tail off in SO<sub>2</sub> beginning at the end of September, however, is consistent with a steady decline from a single source. Visual validation of any additional phreatic plumes is less reliable, especially during winter weather and light conditions late in 2006. Remote sensing methods provide continuous observation, however. The September 17 eruption was observed in Nexar radar and OMI images (Neal et al., 2009). Nexar, a weather radar system, is predominantly sensitive to water vapor [see reference for details]. The OMI system is sensitive to SO<sub>2</sub> and registered on the order of 2000 tons on September 17, but none after that (Neal et al., 2009). Thus, the importance of Nexar and OMI in the current context is that, while both systems registered prominent anomalies comparable to those seen using airborne gas measurements on September 17th, neither showed any notable features in the weeks and months following.

Together, the seismicity, gas data, and phreatic activity suggest a singular event. The sudden onset of large atmospheric plumes on September 17th, accompanied by the short, but strong, seismic activity imply that the eruption was driven by an over pressurization of gas (as most all explosive volcanic events are). It is significant, however, that each of these metrics remained elevated for several months and tailed off gradually. The gradual tail off in SO<sub>2</sub> and CO<sub>2</sub> emissions and stress-driven seismicity indicate that the eruption was insufficient to relieve the gas overpressure. Gas continued to vent over a few months, which is typical following eruptions, e.g. Redoubt in 1989 (Casadevall et al., 1994), or with suspected dike intrusions, e.g. Iliamna in 1996 (Roman et al., 2004). Seismicity not only continued, but was punctuated by significant swarms (Figure 2.7). There are two candidate explanations for the continued activity. Either the initial eruption was insufficient to fully equilibrate the magmatic system, or the crustal source continued to grow and/or exsolved gas after the initial eruption.

The outstanding question is to identify the likely sources of gas pressure that drove this modest eruption. Several scenarios could create a large volume of stored gas at depth. Given the lack of historic eruptions, the absence of notable fumaroles at Fourpeaked (although it does contain a hydrothermally altered summit, Kienle and Swanson, 1983), and the broad glacier cover over the

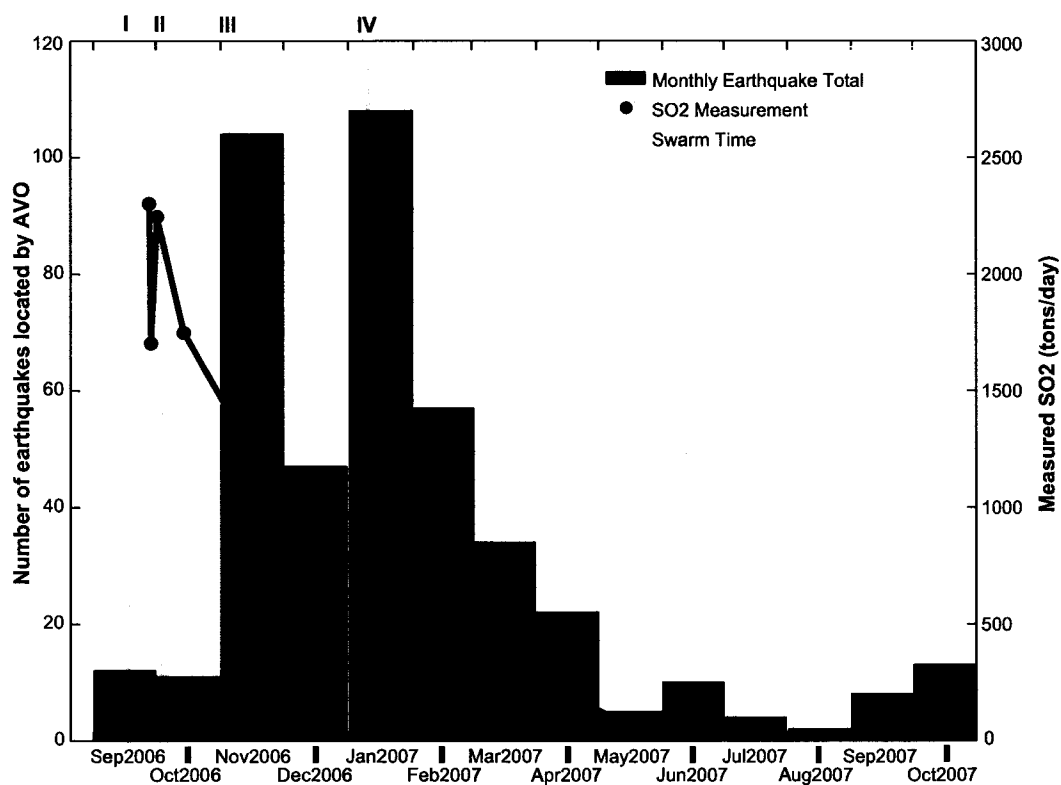


Figure 2.7: Histogram of earthquakes located by routine AVO processing from September 2006 through October 2007. The blue bars are monthly totals. The red dots represent SO<sub>2</sub> COSPEC measurements recorded by AVO. The cyan lines correspond to the swarms analyzed in this paper.

summit, it is not surprising that the edifice might have been impenetrable to gas. Indeed, even the most active Cook Inlet volcanoes, whether glaciated or not, display very little degassing between eruptions (Doukas and McGee, 2007). There was no evidence of any existing gas pathways to the surface, and any eruption would have had to first build up sufficient pressure to break through to the surface.

One explanation is that a latent magma reservoir, perhaps associated with a centuries-old eruption, had been degassing in the mid or lower crust. In this scenario, gas was given off by slowly crystallizing magmas - a so-called "second boiling" (Bowen, 1928). This gas pooled in the shallow crust and accumulated in connected crack networks at, or below, a depth of 5 km (the dominant depth of seismicity). When the stored gas reached a critical pressure, a rapid (on the order of minutes to hours) cascade of rock failures breached the upper crust and opened a pathway to the surface. The subsequent eruption was short-lived, and steam and SO<sub>2</sub>-rich. The ash in the plume could have been fragments of remobilized ash and rock generated during the explosive activity. Alternatively, it could have been magma entrained from the crustal source, though no such juvenile material was found.

We find several shortcomings with this explanation. The absence of known Holocene activity suggests that this latent magma reservoir would be very old and that any gas accumulation occurred on a timescale of centuries. It is also not clear what would have driven the sudden failure of the top several kilometers of crust. As soon as gas began to expand into pathways toward the surface, the pressure would have decreased, slowing the ascent. This is inconsistent with the rapid cascade of failures implied by the earthquake swarm and the large initial plumes. This model would be possible if the gas build up was beneath a strong impermeable layer. Once fractured, the rest of the crust would have required less gas pressure to open. At this time, there is no evidence for such a cap beneath the Fourpeaked region. Furthermore, a vapor reservoir at depth would likely have a carbon/sulfur ratio similar to other arc systems (Fischer and Marty, 2005), and the Fourpeaked gas was not typical (Werner et al., in review).

Another possibility is that fresh basaltic magma from depth was injected into a more silicic reservoir in the mid- to shallow crust. The arrival of hot, basaltic magma would have heated the existing residual, leading to the rapid exsolution of gas. This model requires the existence of andesitic magma mush that is still mobile enough to mix with newly arrived basalt. Given the lack of known

Holocene activity, this seems unlikely as well. It is also hard to explain how this presumably viscous magmatic mush could rapidly produce a large volume of gas without entraining significant portions of either juvenile magmatic component. Again, an intrusion of a primitive nature would likely have produced a gas with a composition richer in  $\text{CO}_2$ . The initial emissions were conspicuously enriched in  $\text{SO}_2$  over  $\text{CO}_2$ , an oddity for any arc volcano (Fischer and Marty, 2005).

Our preferred explanation involves new magma. In this scenario, new magma moved into the shallow crust beneath Fourpeaked on the scale of days to months. Gas, which exsolved rapidly as a result of depressurization, pooled in crack pathways near 5 km depth. The initial pressure of this gas was insufficient to break through to the surface. However, considerable gas remained stored in the magma ready to be exsolved as soon as a modest pressure decrease allowed. When the pressure was finally sufficient to breach the crust, gas moved into the shallowest levels. The displaced gas allowed magma to rise somewhat higher in the system triggering the release of significantly more volatiles and likely remobilizing native sulfur from the existing hydrothermally altered edifice, thus accounting for the initial sulfur-rich composition. This created a positive feedback in which increased pressure drove crack propagation, which allowed gas and magma to rise higher, leading to more exsolved gas and more pressure. This feedback can explain the rapid chain of events on September 17th and the apparently spontaneous generation of large steam and  $\text{SO}_2$  plumes. With time, the C/S ratio of the gas increased to a value that is more typical of Cook Inlet volcano (Werner et al., in review).

There are several variants of this model that cannot be ruled out with existing data. For example, it is possible that the new pulse of magma encountered an aquifer in the shallow crust. The intersection of these two could have rapidly generated sufficient pressure to drive the September 17th eruption and provided a source for the excess of  $\text{SO}_2$  through remobilization of native sulfur near the surface. Seismicity and gas emissions over the next several months are easily explained as the system slowly cooled and the hydrothermal system cauterized the fringes of the magma zone, thus removing the hydrothermal source of sulfur and transitioning to a more typical magmatic gas signature. Typically, hydrothermal scrubbing is observed when volcanic gas enters a water-saturated zone (Symonds et al., 2001); here the force of the initial eruption must not have allowed for much interaction of the volcanic gas with hydrothermal fluids.

Though we prefer this model, there are several caveats. The most notable is the lack of juvenile

ash. Petrographic analysis of the air fall tephras revealed only hydrothermally altered volcanic rock and crystal fragments (Neal et al., 2009). The absence of obvious juvenile ash argues for well-segregated gas and magma. If the gas had sufficient time to segregate fully from the magma then it would be possible to erupt without entraining considerable magma. The "new magma" model, however, relies on gas exsolving from the magma shortly before eruption. It is not clear what range of timescales and viscosities might allow this to occur without entraining large volumes of the magma itself. From this perspective, the hydrothermal aquifer model is attractive.

In the three months following the eruption, seismic and volatile activity at Fourpeaked remained high. SO<sub>2</sub> levels remained above 1000 tons/day at least through mid-November. Seismicity did not begin to tail off until after January. Had the September eruption successfully relieved the overpressure, both of these parameters should have decreased rapidly. Sustained degassing is an indication that gas exsolution continued. Continued seismicity is an indication that stress accumulation continued at depth. If the seismic activity were merely the result of wide spread settling after the eruption, we would not expect this pattern to be punctuated by short bursts of earthquakes. Swarms lasting a few hours are typically associated with highly focused stresses, such as those which accompany the movement of magma or gas. These swarms are common in the build up to eruptions and between explosive episodes. Such patterns were observed during the 2006 Augustine eruption (Dixon et al., 2008) and the 2009 Redoubt eruption. Re-equilibration following eruptions is more often accompanied by seismicity well distributed in space and time.

The post-eruptive swarm activity is best illustrated by swarm IV on January 10. This swarm comprised 49 earthquakes in less than two hours, many with similar waveforms. Repeating (or multiplet) waveforms indicate the earthquakes occurred in close proximity and with a similar source mechanism. The similar locations, high frequency, impulsive arrivals and similar amplitudes suggest progressive failure along a crack. We applied the double difference relocation technique (Waldhauser and Ellsworth, 2000) to improve the precision of the earthquake locations. Figure 2.8A shows the original epicenters of swarm III and swarm IV. Figure 2.8B shows the results after relocation. The relocated hypocenters fall along a line striking NNE but do not demonstrate an obvious progression through time. We note that the NNE trend is parallel to the chain of surface craters observed throughout the period of unrest, suggesting a dominant crack orientation.

Swarm IV showed a high degree of similarity between waveforms (correlation coefficients >

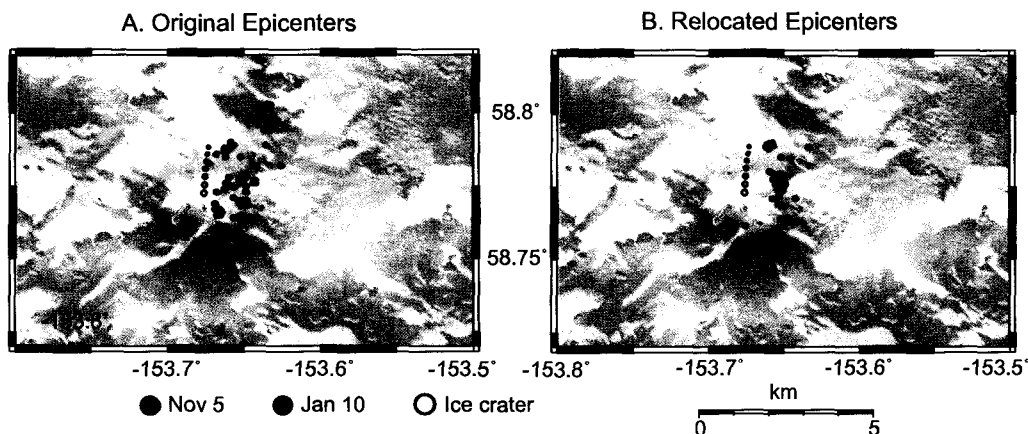


Figure 2.8: Earthquake epicenters before and after double-difference relocation. **(A)** Located earthquakes for swarm III (blue) and swarm IV (red). **(B)** The double-difference relocated hypocenters for the two swarms.

0.8). Such similarity can only be a result of earthquakes occurring within a few hundred meters of each other, otherwise differences in path scattering would destroy the similarities (Snieder and Vrijlandt, 2005). Highly similar waveforms have been seen at many volcanoes, including Mt. St. Helens in 2004 (Iverson et al., 2006, Thelen et al., 2008) and Augustine in 2006 (Buurman and West, 2010). These tight earthquake clusters do not reflect widespread stress readjustment. The highly localized swarms were more likely caused by small gas and/or magma intrusions into surrounding rock. We propose that as Fourpeaked began to seal back up following the September eruption, continued degassing and magma cooling led to modest over pressure that was accommodated by reactivating local crack networks. Some of these dike events produced bursts of seismicity observed in the four months following the eruption.

By February 2007, gas measurements continued to decline and seismicity began to decrease. The fact that both decreased simultaneously gives strong evidence that they signal the end of the current unrest.

## 2.8 Conclusions

The unrest at Fourpeaked provides a good example of how a rapid-response seismic network at a previously unmonitored volcano, combined with an additional data source such as gas emission measurements, can be used to analyze volcanic activity. An important caveat is that much of

this analysis could not have been done without the upgraded seismic network. At the time, it was essential to know what activity was being missed and how improving the network would increase our ability to monitor and understand the volcanic activity. These issues can start to be addressed using the earthquake location success rate and the location errors described above. The Fourpeaked example illustrates the importance of considering these as two separate goals in monitoring and in network design. A good location success rate is essential to determine the source of the observed earthquakes. This is especially true in an environment such as Cape Douglas where the daily seismic record can contain activity from the Katmai cluster of volcanoes to the southwest, Augustine Volcano to the northeast and several different regional sources of earthquakes. Though a seismic swarm was evident on regional seismic stations on September 17, the earthquake locations were essential in confirming that the source was indeed from the Cape Douglas area. The installation of station FOPK and the repair of CDD improved the location success rate threefold prior to swarm II (Figure 2.5). While these stations had little impact on the location errors, they increased the likelihood that earthquakes could be located at all.

The high seismicity levels during the initial unrest along with high levels of gas emissions suggest that a small, single intrusion of new magma is the most likely cause of the activity. The intrusion created or reactivated fractures, allowing for the release of volcanic gases. Continued local stress accumulation led to additional earthquake swarms over the following months while continued high levels of gas indicate the continued exsolution of volcanic gases. This activity continued until the magma had sufficiently cooled and degassed to the point where it could no longer overcome the overburden pressure, allowing the pathways to seal.

#### Acknowledgements

We thank Andrew Newman, David Wilson, Kate Bull, Stephanie Prejean, and Tina Neal for their helpful reviews. We also thank Scott Stihler and Natasha Ruppert for assistance locating earthquakes, Kristi Wallace and Rick Wessels for Fourpeaked visual observations, and Lea Burris for help assembling figures.

## References

- Adleman, J., Cameron, C., Neal, T., Shipman, J., 2008. Hazards communication by the Alaska Volcano Observatory concerning the 2008 eruptions of Okmok and Kasatochi volcanoes, Aleutian Islands, Alaska. In: *Eos Transactions, AGU 89(53), Fall Meeting Supplement, San Francisco, U.S.A.* pp. Abstract A53B-0275.
- Bowen, N., 1928. *The evolution of the igneous rocks.* Princeton University Press, Princeton, NJ.
- Buurman, H., West, M., 2010. Seismic precursors to volcanic explosions during the 2006 eruption of Augustine Volcano. In: Power, J., Coombs, M., Freymueller, J. (Eds.), *The 2006 eruption of Augustine Volcano.* Vol. 1769 of U.S. Geological Survey Professional Paper.
- Carn, S., Pallister, J., Lara, L., Ewert, J., Watt, S., Prata, A., Thomas, R., Villarosa, G., 2009. The unexpected awakening of Chaitén Volcano, Chile. *Eos 90 (24)*, 205–212.
- Casadevall, T., Doukas, M., Neal, C., McGimsey, R., Werner, C., 1994. Emission rates of sulfur dioxide and carbon dioxide from Redoubt Volcano, Alaska, during the 1989-1990 eruptions. *Journal of Volcanology and Geothermal Research 62 (1)*, 519–530.
- Dixon, J., Stihler, S., Power, J., Searcy, C., 2008. Catalog of earthquake hypocenters at Alaskan volcanoes: January 1 through December 31, 2006. U.S. Geological Survey Data Series 326.
- Doukas, M., 2002. A new method for GPS-based wind speed determinations during airborne volcanic plume measurements. U.S. Geological Survey Open-File Report 02-395.
- Doukas, M., McGee, K., 2007. A compilation of gas emission-rate data from volcanoes of Cook Inlet (Spurr, Crater Peak, Redoubt, Iliamna, and Augustine) and Alaska Peninsula (Douglas, Fourpeaked, Griggs, Mageik, Martin, Peulik, Ukinrek Maars, and Veniaminof), Alaska, from 1995-2000. U.S. Geological Survey Open-File Report 2007-1400.
- Fischer, T., Marty, B., 2005. Volatile abundances in the sub-arc mantle: Insights from volcanic and hydrothermal gas discharges. *Journal of Volcanology and Geothermal Research 140 (1-3)*, 205–216.

- Frolich, C., Davis, S., 1993. Teleseismic b-values: or much ado about 1.0. *Journal of Geophysical Research* 98, 631–634.
- Iverson, R., Dzurisin, D., Gardner, C., Gerlach, T., LaHusen, R., Lisowski, M., Major, J., Malone, S., Messerich, J., Moran, S., Pallister, J., Qamar, A., Schilling, S., Vallance, J., 2006. Dynamics of seismogenic volcanic extrusion at Mount St. Helens in 2004–2005. *Nature* 444, 439–443.
- Kienle, J., Swanson, S., 1983. Volcanism in the eastern Aleutian arc: Late Quaternary and Holocene centers, tectonic setting and petrology. *Journal of Volcanology and Geothermal Research* 17 (1–4), 393–432.
- Matumoto, T., Gumper, F., Sbar, M., 1968. A study of microaftershocks following Fairbanks earthquake of June 21, 1967. *American Geophysical Union Transactions* 49, 294.
- McGee, K., Doukas, M., Gerlach, T., 2001. Quiescent hydrogen sulfide and carbon dioxide degassing from Mount Baker, Washington. *Journal of Geophysical Research* 105 (B4), 8447–8456.
- McNutt, S., 2002. Volcano seismology and monitoring for eruptions. *International Handbook of Earthquake and Engineering Seismology* 81A, 383–406.
- Neal, C., McGimsey, R., Dixon, J., Manevich, A., Rybin, A., 2009. 2006 Volcanic activity in Alaska, Kamchatka, and the Kurile Islands: Summary of events and response of the Alaska Volcano Observatory. U.S. Geological Survey Scientific Investigations Report 2008-5214.
- Pavlis, G., Vernon, F., Harvey, D., Quinlan, D., 2004. The generalized earthquake-location (GEN-LOC) package: an earthquake-location library. *Computers and Geosciences* 30, 1079–1091.
- Roman, D., Power, J., Moran, S., Cashman, K., Doukas, M., Neal, C., Gerlach, T., 2004. Evidence for dike emplacement at Iliamna Volcano, Alaska in 1996. *Journal of Volcanology and Geothermal Research* 130, 265–284.
- Snieder, R., Vrijlandt, M., 2005. Constraining the source separation with coda wave interferometry: Theory and application to earthquake doublets in the Hayward fault, California. *Journal of Geophysical Research* 110 (B04301).

- Stepp, J., 1972. Analysis of completeness of the earthquake sample in the Puget Sound area and its effect on statistical estimates of earthquake hazard. In: Proceedings of the First Microzonation Conference, Seattle, U.S.A. pp. 897–909.
- Symonds, R., Gerlach, T., Reed, M., 2001. Magmatic gas scrubbing: Implications for volcano monitoring. *Journal of Volcanology and Geothermal Research* 108, 303–341.
- Thelen, W., Crosson, R., Creager, K., 2008. Absolute and relative locations for earthquakes at Mount St. Helens, Washington using continuous data: Implications for magmatic processes. In: Sheod, D., Scott, W., Stauffer, P. (Eds.), *A volcano rekindled; the renewed eruption of Mount St. Helens, 2004-2006*. Vol. 1750 of U.S. Geological Survey Professional Paper.
- Waldhauser, F., Ellsworth, W., 2000. A double-difference earthquake location algorithm: Method and application to the northern Hayward fault. *Bulletin of the Seismological Society of America* 90, 1353–1368.
- Weimer, S., Wyss, M., 2000. Minimum magnitude of completeness of earthquake catalogs: Examples from Alaska, the western United States, and Japan. *Bulletin of the Seismological Society of America* 90, 859–869.
- Werner, C., Kelly, P., Doukas, M., in review. Gas emissions from failed and successful eruptions from Cook Inlet volcanoes, Alaska, 1989-2006: Emission magnitudes, thresholds, and equilibrium degassing. *Bulletin of Volcanology*.

### Chapter 3: Seismic data from western Mexico from February 2006 - May 2007

#### 3.1 Introduction

Many seismic studies carried out in research worldwide require the use of chosen seismic phase arrivals associated with known earthquake origins. Everything from arrivals from S-waves traversing the outer core (SKS) from teleseismic events for shear-wave splitting, to simple P- and S-waves from small volcanic earthquakes to study volcanic unrest, require earthquake catalogs. Creating these catalogs is a time-consuming process, often requiring full-time seismic analysts whose sole job it is to locate earthquakes. The purpose of this chapter is to describe the methodology that I used to create a catalog of earthquakes throughout western Mexico in 2006 and 2007.

#### 3.2 Data

The seismic data for the remaining chapters comes from two concurrent NSF-funded experiments. A large-scale array of 50 broadband seismometers, consisting of Güralp CMG-3T and Streckeisen STS-2, was deployed across western Mexico, from Puerto Vallarta in the north into the Mexican state of Michoacan to the south, as part of the Mapping of the Rivera Subduction Zone (MARS) project. The project was run by Steven Grand at the University of Texas at Austin, James Ni at New Mexico State University, and Marco Gúzman at the Universidad Nacional Autónoma de México. All of the MARS seismometers were connected to Quanterra Q330 digitizers and were recorded at 40 samples/second. The goal of this project was to study the geometry of the subducting Rivera and Cocos plates underneath western Mexico.

In addition to the MARS array, 20 Güralp CMG-40T seismometers were deployed around Colima volcano as part of the Colima Volcano Deep Seismic Experiment (CODEX) run by Michael West at the University of Alaska Fairbanks and Tonatiuh Dominguez at the Observatorio Vulcanológico de la Universidad de Colima. The CODEX stations were also connected to Quanterra Q330 digitizers and were recorded at 100 samples/second. A station map of both networks is shown in Figures 3.1 and 3.2. The MARS array had an aperture of approximately 300 km, while the CODEX array's aperture was closer to 50 km.

The MARS array ran from January 2006 through June 2007, while the CODEX array was

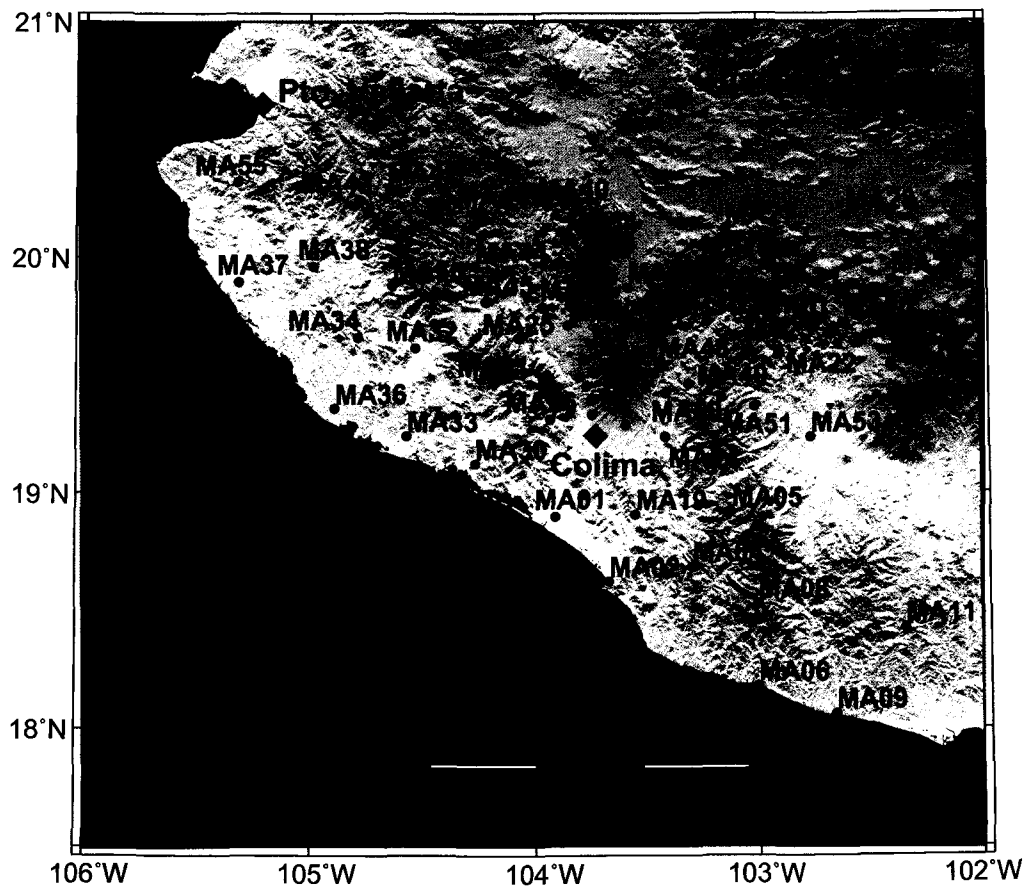


Figure 3.1: A map showing CODEX (red) and MARS (blue) seismic stations deployed in western Mexico from 2006-2008.

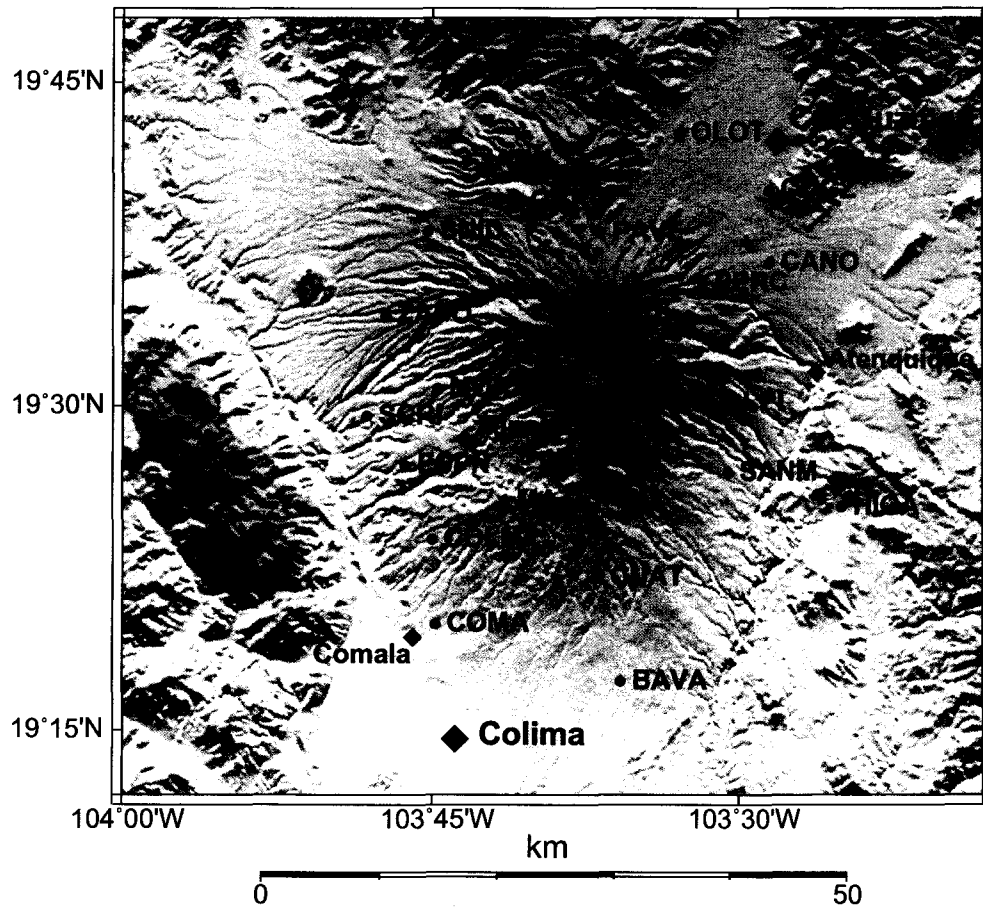


Figure 3.2: A zoom-in of Figure 3.1 showing CODEX stations (red circles). Colima volcano is located at (19°30' N, 103°37' W).

deployed longer, from January 2006 through February 2008. Data from both networks were stored locally at each site and then periodically downloaded. Archives of the data sets are stored at the Incorporated Research Institutions for Seismology Data Management Center (IRIS-DMC).

Data from both networks were saved in day long miniSEED files. While many seismic formats exist, miniSEED is convenient because it is natively supported by Boulder Real Time Technologies' (BRTT) Antelope seismic processing suite, a software package used extensively at the University of Alaska. Antelope utilizes a relational database system built off of the Datascope package. Databasing was accomplished by using the Center for Seismic Studies schema, version 3.0 (css3.0). This schema includes, among other things, tables for storing information about station locations, instrument responses, origin information, arrival information, and the waveforms themselves.

### 3.3 Earthquake Catalog

For an initial attempt to create an earthquake catalog, a standard methodology was used for locating earthquakes. The continuous waveforms for all stations were scanned by eye in three minute windows. P- and S-wave arrivals were picked for any earthquakes that could be seen on at least five stations. P-waves were only picked on vertical components and S-waves were picked on horizontal components, following standard seismic practice for three-component stations. When all arrivals for a given event had been picked, the earthquake was located using the genloc algorithm (Pavlis et al., 2004) and the 1-D velocity model used for southern Alaska shown in Table 3.1 (Matumoto et al., 1968). This velocity model was used as a proxy because southern Alaska has a similar tectonic setting to western Mexico, as opposed to a global-scale velocity model such as IASPEI91. Following this procedure, 429 events were located in February and March 2006. However, creating a catalog of earthquakes in this manner proved to be extremely time-consuming (taking on the order of 6 man-hours to process 1 day of seismic data), and so a faster, more efficient method was sought.

The first step was to create a list of possible arrival phases in the data, hereafter referred to as detections. To create a detection, the waveforms were filtered using a 1-10 Hz bandpass filter. This filtering was necessary because of the large amount of high-frequency cultural noise present in much of the data. After filtering, the waveforms were then run through a short-term average / long-term average (STA/LTA) routine. STA/LTA routines are useful, when properly configured, for their ability to pick impulsive features in time series data (for seismic data, this would correspond to

Table 3.1: 1-D velocity model for southern Alaska.

Depth (km) to layer top	P velocity (km/s)
0.0	5.3
4.0	5.6
10.0	6.2
15.0	6.9
20.0	7.4
25.0	7.7
33.0	7.9
47.0	8.1
65.0	8.3

a possible P- or S-wave arrival). This function calculates the average amplitude over a sliding short time window (0.7 seconds), and the average amplitude over a long time window (8 seconds). If the ratio of the short-term average divided by the long-term average exceeded 4, then a detection was declared. The value of 4 was chosen as a compromise after trial-and-error between detecting too much noise (lower values) and missing too many arrivals because they were not impulsive enough (higher values). Ideally, this function would create a detection whenever an impulsive arrival (from an earthquake, or simply noise that happens to be impulsive) is observed, while ignoring "spikey" data. The STA/LTA routine was run independently on all channels of all stations for each month. The resulting tables contained 1.5-4 million detections per month.

Next, a rectangular grid was created for the study area in order to parameterize the area for travel time calculations. The grid was  $\pm 3$  great-circle degrees ( $\approx 330$  km) in both the  $x$  (north-south) and  $y$  (east-west) directions and centered at Colima Volcano ( $19.5^\circ\text{N}$ ,  $103.6^\circ\text{W}$ ). The grid consisted of  $51 \times 51$  equally-spaced horizontal nodes and 19 depth nodes ranging from 0 to 200 km depth. At each node point, P and S-wave travel times were calculated to each station in the MARS and CODEX arrays. Due to a limitation in the program, the IASPEI91 global velocity model was used instead of a better-fitting local model.

Using this grid, detections were associated together to form possible origins using the `dbgrassoc` algorithm in the Antelope software package. Appendix 3.A contains all of the parameter files used in this chapter. For each detection, `dbgrassoc` searches for detections on other stations that

would roughly correspond to an origin at one of the grid nodes using the travel times previously calculated. For this data set, a minimum of ten detections corresponding to either P or S arrivals on any number of stations were required for an origin to be created. P-waves were only associated with detections on vertical (BHZ or HHZ) channels, while S-waves were only associated with detections on horizontal (BHE, BHN, HHE, or HHN) channels. The ten detection requirement was instituted after exhaustive trial-and-error testing in order to minimize the number of false origins while not missing too many of the smaller or more distant origins.

Once a preliminary origin was created, the arrival information was used to locate the event again with the grid node as the starting location using the genloc location algorithm with the southern Alaska velocity model shown in Table 3.1. The resulting origin was considered to be the final origin and placed in the earthquake catalog, called the PROVisional earthquake CATalog, version B (Provcats-B). A hypocenter map with cross-sections of the full catalog (4509 earthquakes) is shown in Figure 3.3. Local magnitudes ( $M_L$ ) were also computed for every arrival. The magnitudes were calculated by finding the maximum peak-to-peak amplitude over a time window around an event. In order to get an accurate estimation of background amplitudes as well as the P and S arrivals, the window was defined by 10 seconds prior to the predicted P arrival (computed by using the IASPEI91 velocity model) to  $3*(S \text{ arrival time} - P \text{ arrival time})$  seconds afterward. All components of every station with a picked arrival were used for this calculation. The overall magnitude is the median of the individual station magnitudes, giving equal weight to all stations. The catalog contained magnitudes ranging from  $M_L$  1.0-6.9, and had a magnitude of completeness of 2.6.

The origin data output by dbgrassoc were compared with the manually-picked data for February and March 2006 in order to gauge how effective the associator was working. For the same time period, the automated catalog contained 483 origins. Of these origins, 279 (58%) matched up with the corresponding 429 origins in the hand located catalog. Earthquakes in the manual catalog that were missed by the automated catalog often had magnitudes less than 2.5, were located more than 50 km outside of the MARS network, or were not seen on enough stations to have the necessary number of arrivals to meet the minimum 10-arrival criteria for inclusion in the automated catalog. Additional earthquakes in the automated catalog that did not appear in the manual catalog often contained enough false arrival picks to generate an erroneous origin.

To assess the quality of the origins that matched between the manual and automated catalog, I

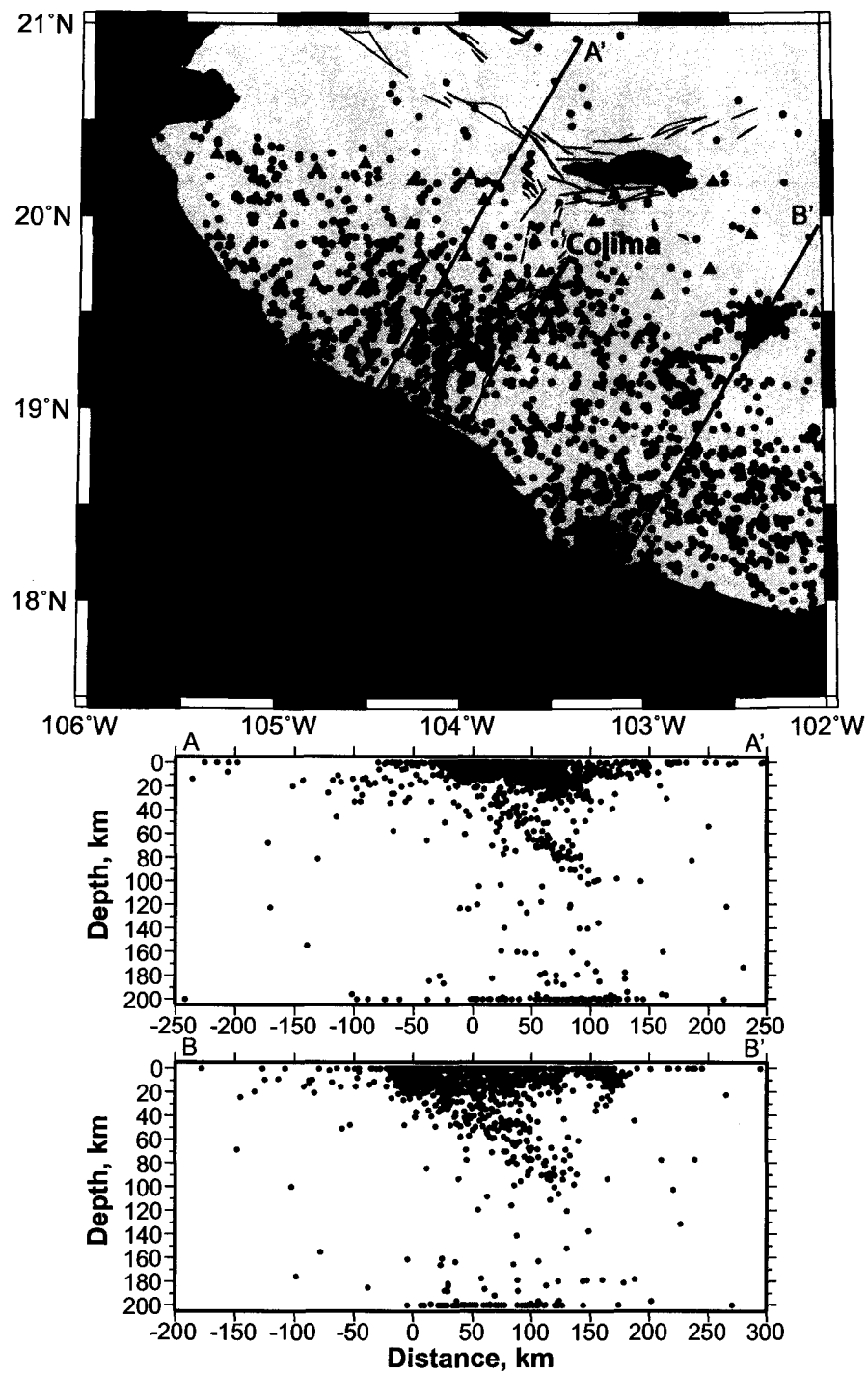


Figure 3.3: An epicenter map with cross-sections through the Provcats-B catalog. While the earthquake locations were completely automated, a Wadati-Benioff zone can be seen extending from 40-100 km depth in both cross-sections.

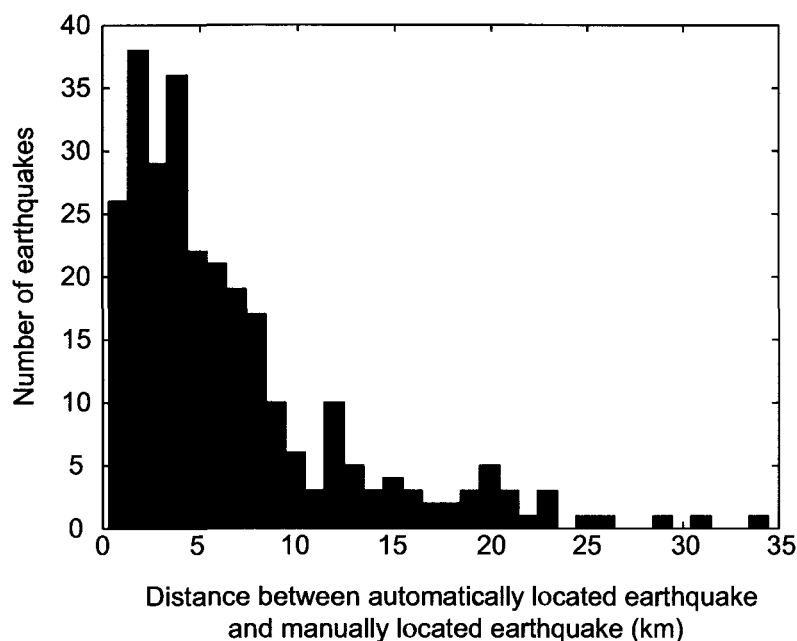


Figure 3.4: A histogram showing the distance between a manually located earthquake and its matching automatically located earthquake.

calculated the distance between the automatically located earthquake and its corresponding match in the manual catalog. A histogram showing the results is shown in Figure 3.4. A vast majority (82%, 228 events) of the earthquakes located within 10 km of each other, and only two exceeded 30 km.

While there are certainly many poorly located or false origins (the numerous earthquakes at 200 km depth in Figure 3.3, for example, are an artifact of setting a depth floor and are typically either false or of teleseismic origin), a Wadati-Benioff zone can clearly be seen. Furthermore, even though the velocity model used to locate the earthquakes was not developed for western Mexico, it does a reasonable job at predicting seismic travel times (RMS travel time residuals of 0.63 seconds). Figures 3.5, 3.6, and 3.7 show example waveforms from three automatically located earthquakes. As can be seen, arrivals for the slab and crustal earthquakes are generally picked well, although a few arrivals that could have been picked manually are missed. Arrivals for the poorly located event in Figure 3.7 are actually picked quite well, however, our routine forces all origins to be located within the travel time grid, therefore it cannot handle teleseismic events like the one shown. In

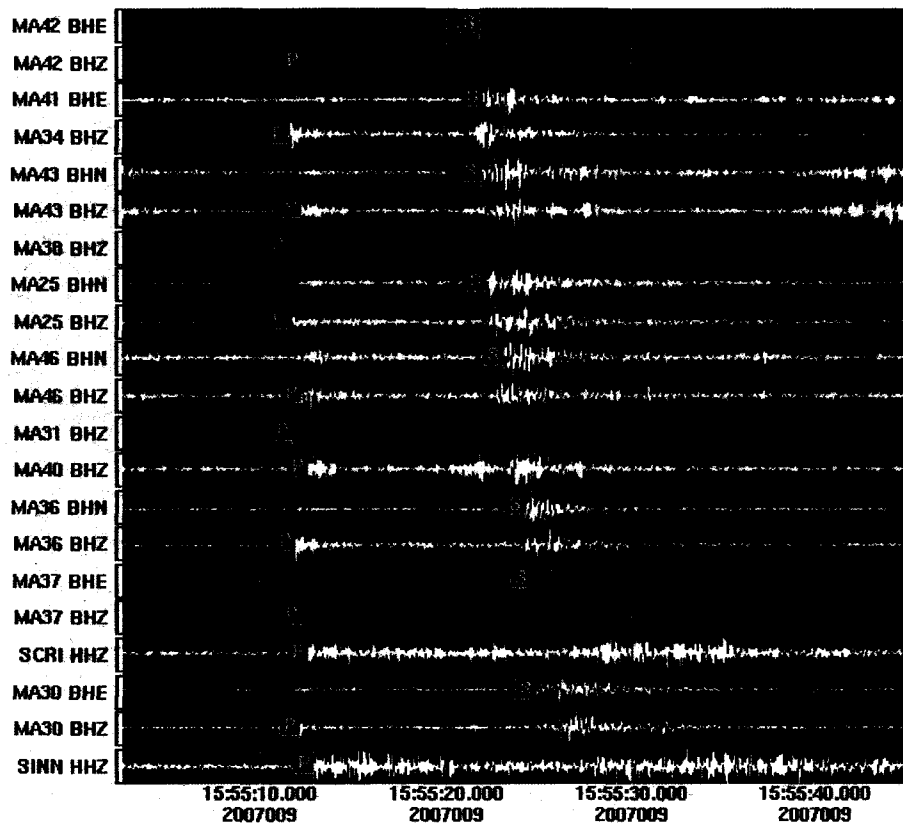


Figure 3.5: An example of an automatically located slab earthquake. The data are displayed using a 1-10 Hz bandpass filter. While some phase arrivals were missed, the arrivals that were picked are all correct.

order to fit the arrivals best, it puts the origin as deep as possible, i.e., at 200 km depth. To further demonstrate the robustness of the catalog, a reduced travel time plot is shown in Figure 3.8. In this plot, crustal-traveling arrivals ( $P_g$ ) can be seen in the purple box, mantle-traveling arrivals ( $P_n$ ) are in the green box, reasonably located deep events are in the cyan box, and mislocated 200 km deep origins are clearly seen in the red box. For a comparison, a reduced travel time plot using the arrivals picked by hand in February and March 2006 are shown in Figure 3.9. While the automated catalog has more scatter, similar crustal and mantle trends are observed.

The biggest strength of this catalog, however, is that it contains over 4500 origins, using over 81,000 arrivals, and yet it took only 100 hours of CPU time to generate on a mid to upper-grade desktop computer.

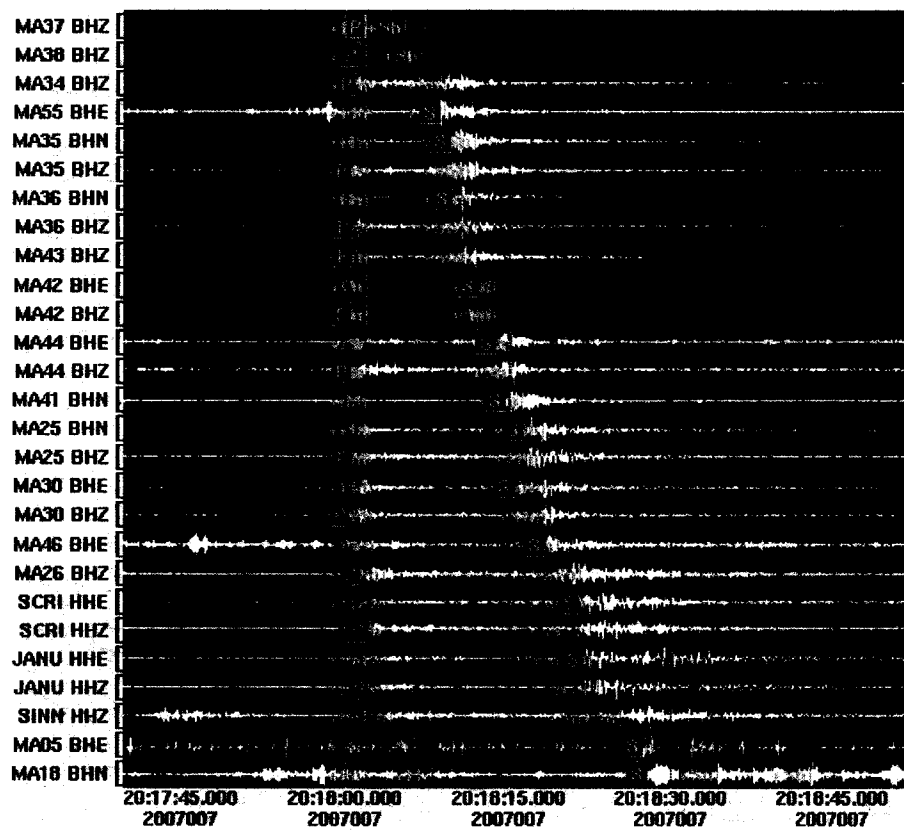


Figure 3.6: An example of an automatically located crustal earthquake. The data are displayed using a 1-10 Hz bandpass filter. All of the arrivals that were automatically picked are correct except for the S-wave arrival on station MA05.

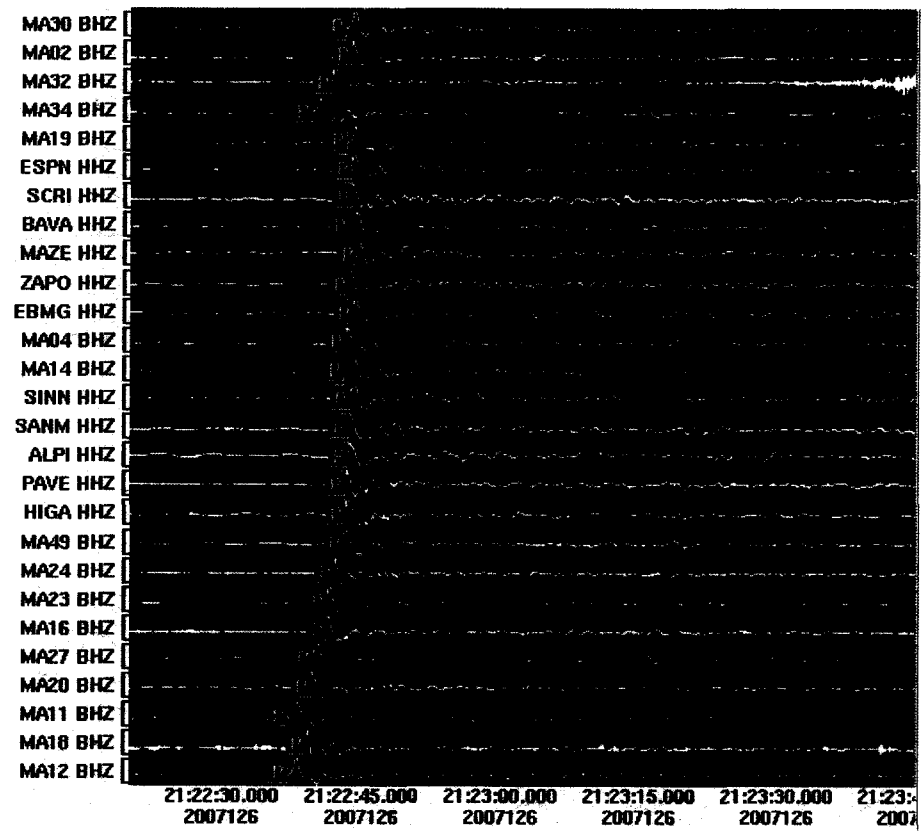


Figure 3.7: An example of a mislocated earthquake. This event is actually a  $M_w$  6.1 deep-subduction zone earthquake that occurred near Fiji. The automated algorithm placed this event off the coast of western Mexico at a depth of 200 km.

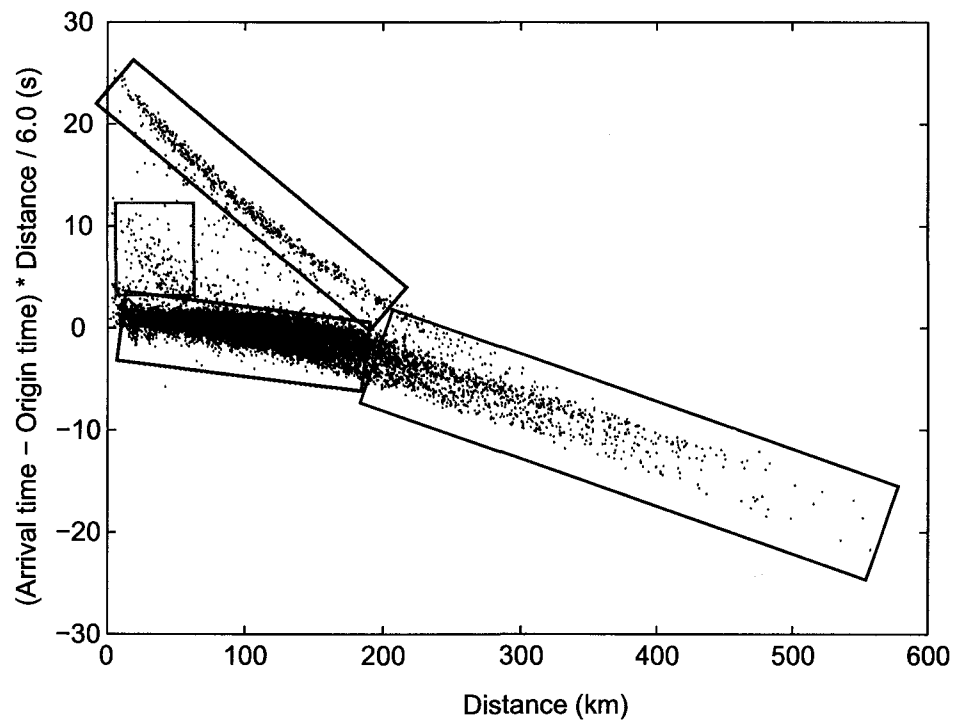


Figure 3.8: A reduced travel time curve for the automated event catalog. The travel times have been reduced by a constant 6.0 km/s. Note: for plotting clarity, the number of arrivals plotted has been decimated by a factor of 5. The colored boxes correspond to (purple) arrivals with waves that pass primarily through the crust, (cyan) arrivals from deep events, (green) arrivals with waves that travel through the mantle, and (red) false events that are artificially placed at 200 km depth.

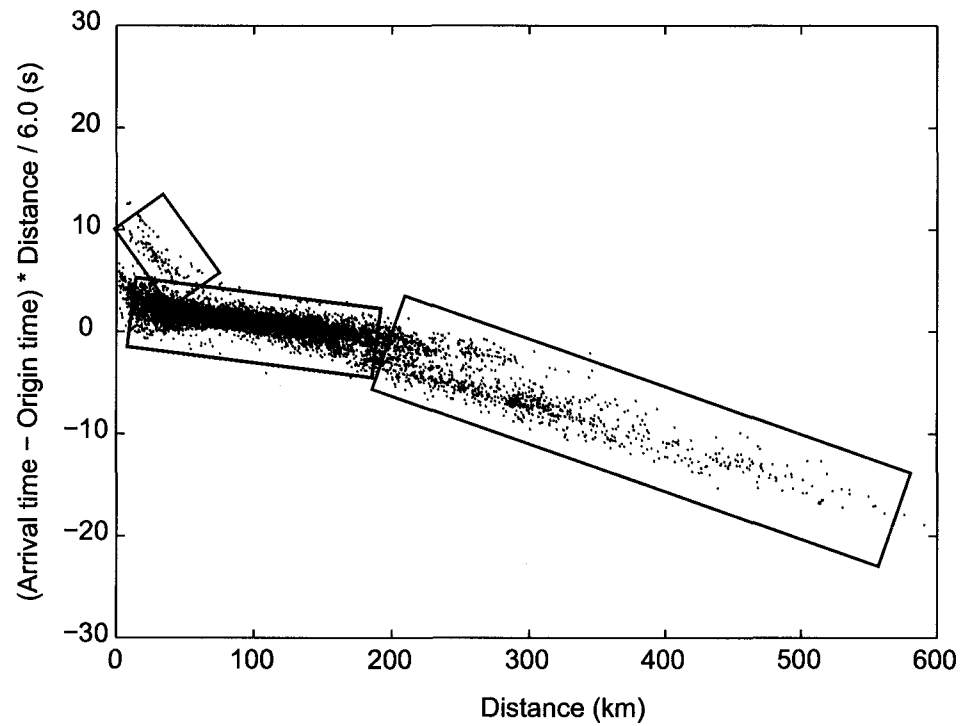


Figure 3.9: A reduced travel time curve for the two-month manually located event catalog. The travel times have been reduced by a constant 6.0 km/s. The colored boxes correspond to (purple) arrivals with waves that pass primarily through the crust, (cyan) arrivals from deep events, (green) arrivals with waves that travel through the mantle.

### 3.4 Catalog Analysis

One issue with the catalog was how to tell if an origin is reliable; that is, if the location, depth, and associated arrivals are comparable to what would be generated by manually picking the arrivals and locating the event. In order to address this issue, I compared two months of manually located events with the same two months of Provcats-B origins, and created an empirical grading system based on the results of the comparison.

Three different grades of earthquake quality were defined based on trial-and-error procedures. The lowest level, grade 1, simply required that an origin have the required ten arrivals for being included in the catalog. The next level, grade 2, were considered to be "well located" earthquakes that were created using the automated procedure described above. In order to meet this criteria, an origin had to have at least 10 P-wave arrivals, at least 4 S-wave arrivals, and the number of P-waves must be greater than or equal to the number of S-waves. These conditions were settled on after comparing the automated catalog for February and March 2006 with the manually picked locations from the same months and attempting to find criteria common to the majority of the 279 earthquakes that matched between both catalogs.

Of the 430 events in the automated catalog, only 121 (28%) met the criteria to be classified as grade 2. However, of those 121, 119 (98%) were within  $\pm 0.25^\circ$  latitude and longitude and  $\pm 10$  seconds of an origin in the manually picked catalog. These criteria for grading the origins represent an optimization between catching the most number of "well located" earthquakes versus minimizing the number of poor origins that get classified as grade 2. In all, a total of 1022 origins were considered to be grade 2.

The final level, grade 3, was reserved for origins that had been reviewed by me for quality and correctness. In total, 1042 earthquakes were classified as grade 3 (429 in the February and March 2006 full catalogs, 314 events that were part of a swarm of earthquakes at Parícutin [see Chapter 4], and 299 events that were used for travel-time tomography [see Chapter 5]).

To check for any biases in the hypocenters, I looked at the formal location errors in the full catalog. Figure 3.10 shows the maximum horizontal and depth errors with time. In general, depth errors are less than 5 km and the horizontal errors are less than 10 km. No correlation with time in either error can be seen. I also examined the strike of the horizontal error ellipse. Figure 3.11 is a histogram plot of the strike of the semi-major axis of the error ellipse. There is a moderate bias of

errors in the 20-60 degree range. This could be explained by large number of events located west of 103.5 degrees W longitude, near the eastern edge of the MARS array. With a relative lack of stations to the northeast/southwest of these events, the error ellipses would be expected to also trend in that direction.

### 3.5 Tectonic Comparison

As a final verification of the catalog, I also compared our detected seismicity with the known seismic activity of western Mexico. The Jalisco - Colima - Michoacán portion of the Mexican subduction zone is known to be quite active, with multiple large thrust earthquakes occurring since 1900 (Santoyo et al., 2005). Notable earthquakes include two in 1932 in the north towards Puerto Vallarta, estimated to be around  $M_w$  8.0, an  $M_w$  8.0 near Colima in 1995, an  $M_w$  7.6 near Tecomán in 2003, and two in Michoacán to the south in 1985 and 1986 (Figure 3.12). It is possible that some of the seismicity, including the large cluster of events in the southeast near the coast (Figure 3.13, red box), could be aftershocks from some of these large earthquakes. In addition, our catalog detected a large swarm of over 700 earthquakes near Parícutin volcano in the northeastern portion of the MARS array (Figure 3.13, green box). Highly vigorous swarms in this area have been known to occur in the past (Pacheco et al., 1999). Finally, the Wadati-Benioff zone seen in our catalog has a rough angle of subduction of 45 degrees. This angle matches well with previously observed seismicity (Pardo and Suárez, 1995), as well as with tomographic images of the slab (Yang et al., 2009).

### 3.6 Velocity Model Analysis

While the southern Alaska 1-D model does a reasonable job fitting the travel times for seismic waves in western Mexico, improvements can be made. Many methodologies exist for improving existing velocity models. I chose to use the same set of codes that I used to perform the P-wave travel time tomographic inversion in Chapter 5, the RAYTRACE3D algorithm written by William Menke (Menke, 2005). I used this code to insure maximum compatibility between the 1-D code and the 3-D code used in Chapter 5. As its name implies, RAYTRACE3D uses raytracing of waves through a three dimensional model to compute seismic travel times and invert for velocity perturbations in the model.

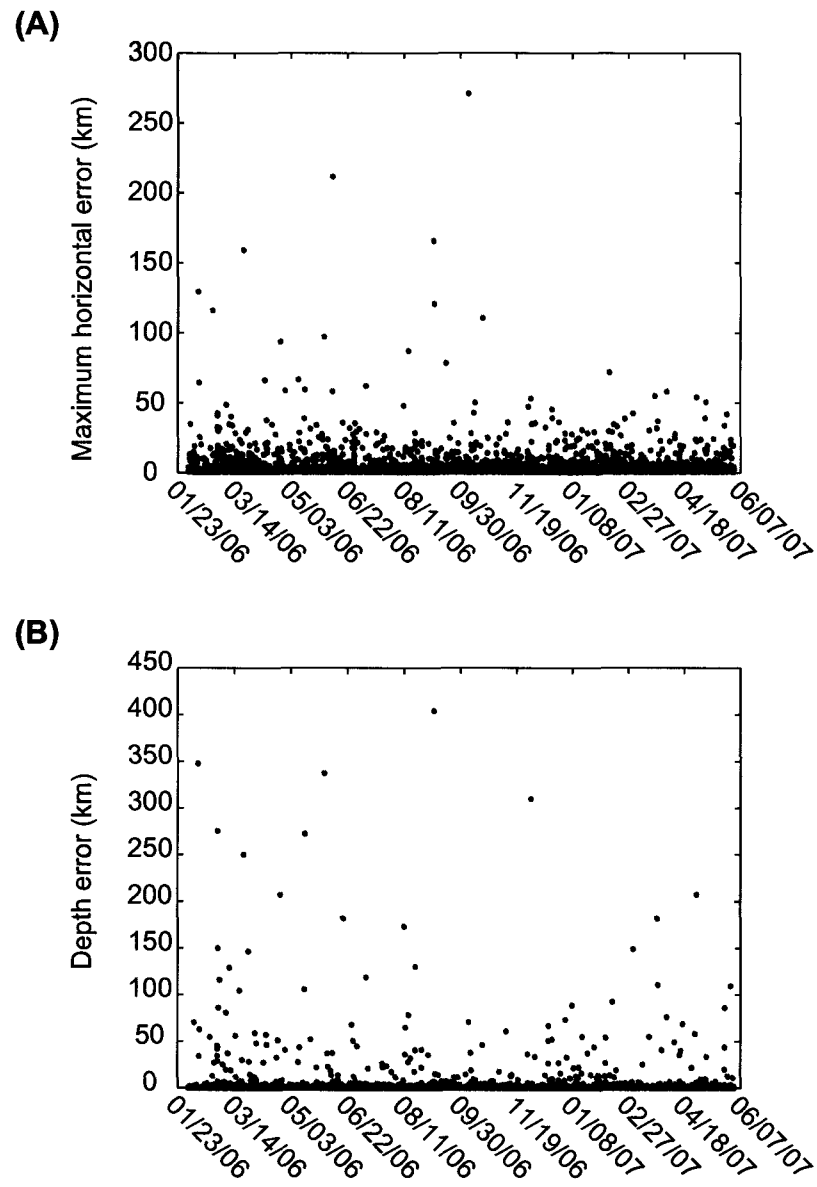


Figure 3.10: Location errors for earthquakes in the automated catalog. (A) Shows maximum horizontal errors with time, (B) shows depth errors with time. Neither plot show a systematic change in errors with time.

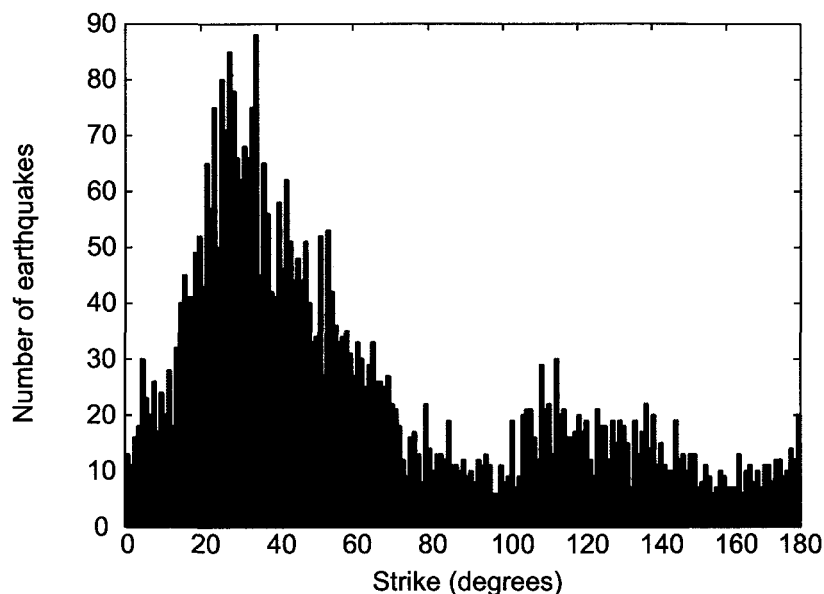


Figure 3.11: A histogram of the strike of the semi-major axis of the location error ellipses. The angles are calculated clockwise from north. A majority of the errors have strikes from 20-60°, consistent with the large number of earthquakes located near the eastern edge of the MARS array.

To create a starting model, I first divide the area of interest into a three dimensional grid of tetrahedra. The coordinate system chosen is a right-handed Cartesian  $(x, y, z)$  system where  $x$  is north/south,  $y$  is east/west, and  $z$  is down (depths are positive). The overall model must bound all of the points of interest, which includes all CODEX and MARS stations, as well as all earthquake hypocenters. Therefore, the initial model ranges from 17°N - 21°N and 106°W - 101°W. This area must then be divided into a grid containing  $L \times M \times N$  nodes. The simplest grid is one of equal  $L$  and  $M$  spacing, however, since the area of interest is near the volcano and not at the edges of the model, I use an irregularly spaced grid containing 50x50 nodes, with a dense grid containing 75% (37) of the nodes with 2 km spacing in an area centered around Colima Volcano, from 19.143 – 19.809°N and 103.951 – 103.235°W. The remaining 25% of the nodes are in a sparse grid covering the rest of the area. A conceptual cartoon representation of this grid is shown in Figure 3.14.

Topography was added to the top depth layer using 3 arc-second Shuttle Radar Topography Mission (SRTM) data. Subsequent depth layers ran from 3 to 45 km with 3 km spacing, and additional layers at 60, 80, 100, and 300 km. Starting P-wave velocities were taken from the southern Alaska velocity model, interpolating where necessary. S-wave velocities were calculated using a constant

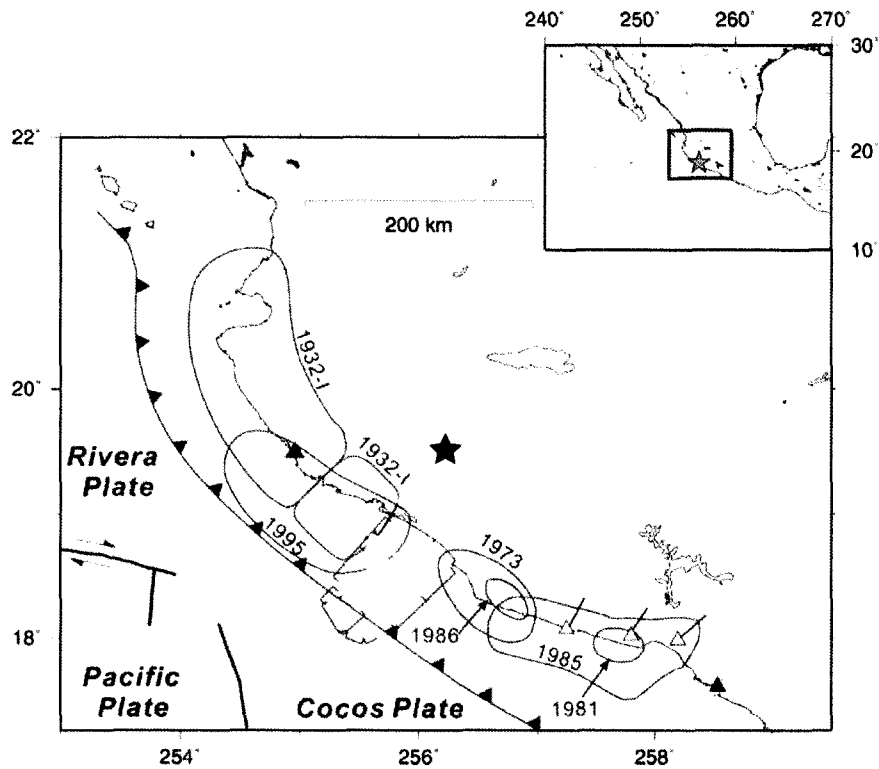


Figure 3.12: A map showing notable large thrust earthquakes in western Mexico. The figure was modified from Yagi et al. (2004). The contours show the extent of the aftershocks for each earthquake. The small triangles and stars are epicenters for each earthquake, and the large star indicates the location of Colima volcano. The subduction trench is shown by the sawtooth line.

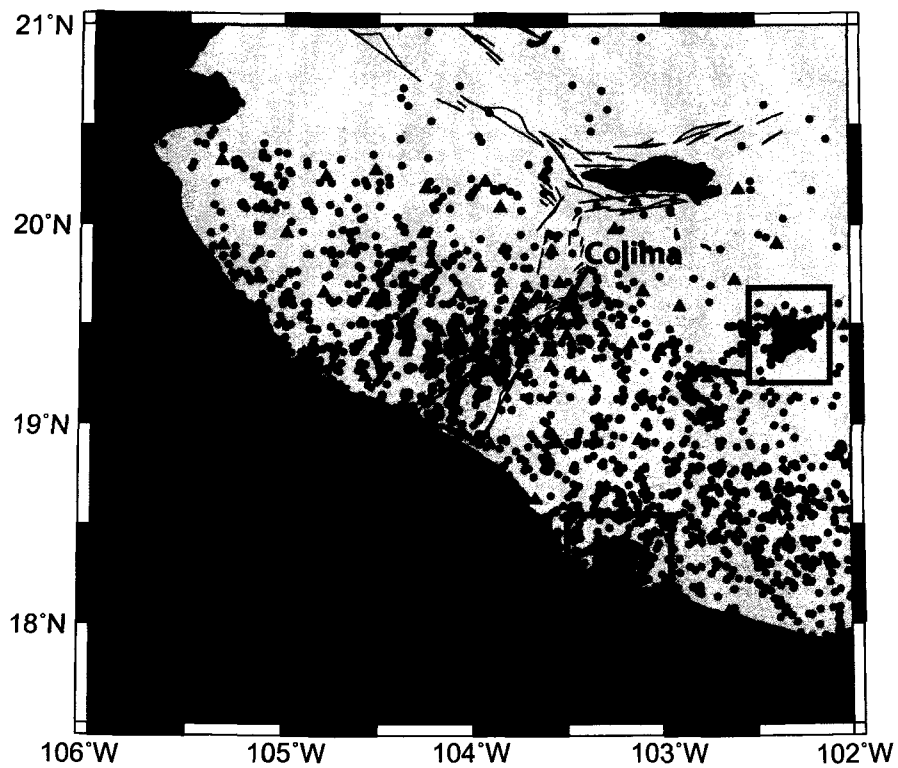


Figure 3.13: An epicenter map showing seismicity of western Mexico. The red box corresponds to a possible aftershock cluster of earthquakes. The green box corresponds to a swarm of earthquakes near Parícutin volcano.

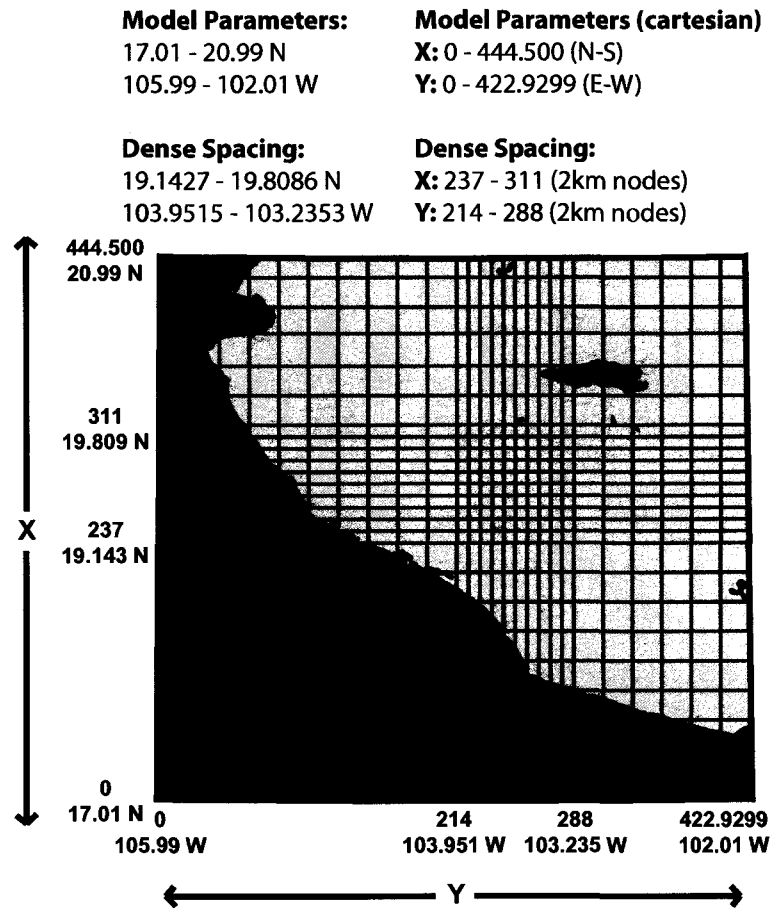


Figure 3.14: A conceptual diagram showing the 3-D grid used for creation of the velocity model. The coordinate system used is a cartesian right-handed system where the north, east, and down (depth) directions are positive. The grid contains 50x50 horizontal nodes, with 75% (37) of the nodes in each direction forming a dense grid with 2 km node spacing centered around Colima volcano.

1.73 P:S velocity ratio. In between layers, the velocities were calculated using a linear gradient.

For consistency, the set of origins used were the same as those used for the full 3-D inversion. These consisted of 198 earthquakes associated with the Wadati-Benioff zone and 101 selected crustal events (depths less than 40 km). For a full description of these events and why they were chosen, see Chapter 5. The origin locations, times, and all associated arrivals were used as the input data for the inversion.

Inverting the data required selecting both a smoothing and damping parameter. RAYTRACE3D allows for model smoothing by requiring that certain grid nodes in the model change together. In effect, this means that a velocity perturbation in the model must be large enough to influence most of the nodes that are locked together in order to change the final model. In order to invert for a 1-D velocity model using a 3-D grid, I forced all nodes within each depth layer to change together, but allowed every depth layer to change independently. A damping parameter was selected through trial-and-error in order to limit the velocity gradients between layers to reasonable values. The final velocity model, shown in Table 3.2, decreased travel time residual RMS values from 0.63 seconds with the southern Alaska velocity model to 0.46 seconds, a modest but noticeable 27% improvement.

This final 1-D model is used as the starting model, except where noted, in the final chapters and methodologies in this thesis.

Table 3.2: Best-fitting 1-D velocity model for western Mexico.

Depth (km) to layer top	P velocity (km/s)
0.0	5.26
3.0	5.56
6.0	5.87
9.0	6.07
12.0	6.41
15.0	6.71
18.0	7.01
21.0	7.11
24.0	7.22
27.0	7.32
30.0	7.41
33.0	7.51
36.0	7.69
39.0	7.74
42.0	8.08
45.0	8.11
60.0	8.21
80.0	8.28
100.0	8.63
300.0	8.83

## References

- Matumoto, T., Gumper, F., Sbar, M., 1968. A study of microaftershocks following Fairbanks earthquake of June 21, 1967. *American Geophysical Union Transactions* 49, 294.
- Menke, W., 2005. Case studies of seismic tomography and earthquake location in a regional context. In: Levander, A., Nolet, G. (Eds.), *Seismic Earth: Array Analysis of Broadband Seismograms*. Vol. 157 of Geophysical Monograph Series. American Geophysical Union, Washington, DC, pp. 7–36.
- Pacheco, J., Valdés-González, C., Delgado, H., Singh, S., Zuñiga, R., Mortera-Gutiérrez, C., Santoyo, M., Domínguez, J., Barrón, R., 1999. Tectonic implications of the earthquake swarm of 1997 in the Michoacan Triangle, Mexico. *Journal of South American Earth Sciences* 12, 567–577.
- Pardo, M., Suárez, G., 1995. Shape of the subducted Rivera and Cocos plates in southern Mexico: Seismic and tectonic implications. *Journal of Geophysical Research* 100 (B7), 12357–12373.
- Pavlis, G., Vernon, F., Harvey, D., Quinlan, D., 2004. The generalized earthquake-location (GEN-LOC) package: an earthquake-location library. *Computers and Geosciences* 30, 1079–1091.
- Santoyo, M., Singh, S., Mikumo, T., Ordaz, M., 2005. Spacetime clustering of large thrust earthquakes along the Mexican subduction zone: an evidence of source stress interaction. *Bulletin of the Seismological Society of America* 95 (5), 1856–1864.
- Yagi, Y., Mikumo, T., Pacheco, J., Reyes, G., 2004. Source rupture process of the Tecomán, Colima, Mexico earthquake of 22 January 2003, determined by joint inversion of teleseismic body-wave and near-source data. *Bulletin of the Seismological Society of America* 94 (5), 1795–1807.
- Yang, T., Grand, S., Wilson, D., Guzman-Speziale, M., Gomez-Gonzalez, J. M., Dominguez, T., Ni, J., 2009. Seismic structure beneath the Rivera subduction zone from finite-frequency seismic tomography. *Journal of Geophysical Research* 114 (B01302).

### 3.A Appendix

This appendix contains the parameter files used for the automated detection and location algorithms.

#### Travel-time grid

The following parameter file was used as an input for the ttgrid routine for the creation of a travel-time grid.

File: ttgrid.pf

# parameter file for ttgrid

grids &Arr{

  regional &Arr{

    mode      edp      # defines an equal-distance projection regular 3-D mesh

    latr      19.5      # reference latitude (origin of grid)

    lonr      -103.6    # reference longitude (origin of grid)

    nx       51       # Number of X-axis distance grid nodes

    ny       51       # Number of Y-axis distance grid nodes

    xmin     -3.0      # Minimum value of X-axis distance grid in degrees

    xmax      3.0      # Maximum value of X-axis distance grid in degrees

    ymin     -3.0      # Minimum value of Y-axis distance grid in degrees

    ymax      3.0      # Maximum value of Y-axis distance grid in degrees

    strike    90.0      # Angle from north clockwise in degrees to the X-axis

    compute\_P  yes      # yes = Compute P travel times

    compute\_S  yes      # yes = Compute S travel times

    method     ttauap   # method for computing travel times

    model      iasp91   # model for computing travel times

    depths &Tbl{

      0.0

      1.0

      5.0

     10.0

```
15.0
20.0
30.0
40.0
50.0
60.0
70.0
80.0
90.0
100.0
120.0
140.0
160.0
180.0
200.0
    }
}
}
```

#### Detections

The following parameter file was used as an input for the dbdetect routine for the creation of detections in the waveforms.

File: dbdetect.pf

# Parameter file for orbdetect

# Following are required and are used as overall defaults

```
ave_type    rms    # Method for averaging (rms or filter)
sta_twin    0.7    # short term average time window
sta_tmin    0.5    # short term average minimum time for average
sta_maxtgap 0.5    # short term average maximum time gap
```

```

lta_twin      8.0    # long term average time window
lta_tmin      6.0    # long term average minimum time for average
lta_maxtgap   4.0    # long term average maximum time gap
nodet_twin    0.0    # no detection if on time is less than this
pamp          500.0  # plot amplitude
thresh        4.0    # detection SNR threshold
threshoff     3.0    # detection-off SNR threshold
det_tmin      0.2    # detection minimum on time
det_tmax      60.0   # detection maximum on time
latency       30     # input packet pipe latency (per channel) in packets
h             0     # plot channel height in pixels
filter        none   # default filter
iphase        D     # default iphase for detections
process_twin  60.0   # data is processed in hunks of this duration
# At least one default band must be set set up in the bands table
# parameter values override default values above for each band
bands &Tbl{
    &Arr{          sta_twin    0.7
        sta_tmin    0.5
        sta_maxtgap 0.3
        lta_twin    8.0
        lta_tmin    6.0
        lta_maxtgap 4.0
        pamp        500.0
        filter      BW 1.0 4 10.0 4
    }
}
# At least one data channel must be specified in the stachans table
stachans &Tbl{
    [BH]H[ENZ]

```

```

}
# channels to reject
reject &Tbl{
}

```

### Grid Associator

The following parameter file was used as an input for the dbgrassoc routine for the association of detections with arrivals and location of detected earthquakes.

File: dbgrassoc.pf

```

# Parameter file for dbgrassoc
process_time_window    60.0    # Main detection processing time window
process_ncycle         0        # how often to do detection processing, in detections
process_tcycle         10       # how often to do detection processing, in delta time
grid_params &Arr{
  regional &Arr{
    nsta_thresh    10    # Minimum allowable number of stations
    nxd            11    # Number of east-west grid nodes for depth scans
    nyd            11    # Number of north-south grid nodes for depth scans
    cluster_twin   1     # Clustering time window
    try_S          no    # yes = Try observations as both P and S
                    # no = Observations are P only
    associate_S    yes   # yes = Try to associate observations as both P and S
    reprocess_S    yes   # yes = Reprocess when new S-associations found
    auth           dbgrassoc
    drop_if_on_edge no
    P_channel_sifter [BH]HZ
    S_channel_sifter [BH]H[NE]
    P_det_tmin      10
    priority        5
  }
}

```

```

    use_dwt      yes
    dwt_dist_near  2.0
    dwt_wt_near   1.0
    dwt_dist_far   6.0
    dwt_wt_far    0.1
    relocate      /home/mgardine/testing/NEW/rundbgenloc
    use_only_relocation  yes
  }
}
# parameters for "smart" association
assoc_method    tt1dcvl    # method for computing predicted travel times
assoc_model     scak      # velocity model for computing predicted travel times
assoc_phases    basic     # phase list for computing predicted travel times
assoc_P_thresh  5.0      # P-residual threshold for associations
assoc_S_thresh  10.0     # S-residual threshold for associations
assoc_ignoreiphase  no    # should the arrival row iphase value be ignored?
assoc_firstphase  yes    # should only the earliest predicted phase be used?
assoc_screen_new  time
assoc_screen_old  (time-900.0)::(time+900.0)
    # these are screening database expressions that should
    # match the existing (old) origins with the new origin for
    # association processing
assoc_expression  $nass>=$nars
    # this is a database expression that should evaluate
    # to true whenever an association is valid
author_priority &Arr{    # prefer priority as a function of assoc author
}

```

## Chapter 4: Dike emplacement near Parícutin volcano, Mexico in 2006<sup>2</sup>

### 4.1 Abstract

A major seismic swarm occurred near Parícutin volcano between the end of May and early July 2006. More than 700 earthquakes with magnitude ( $M_L$ ) exceeding 2.4 were located. Parícutin, located in the Michoacán - Guanajuato volcanic field in western Mexico, is well known as the site of the 1943 eruption in which a new 400 m cinder cone was constructed in what had been farmland. The 2006 swarm exhibits all of the characteristics typically associated with swarms of volcanic origins. The earthquake rate shows the typical ramp up and ramp down over the course of several days. Magnitudes are evenly distributed in time with a notably high b-value of 2.45. The earthquake locations cluster around a northeast-striking trend extending approximately 6 km. Over the first two weeks, hypocenters migrated steadily a few hundred meters per day, rising from 9 to 5 km depth and moving northeast about 5 km. On approximately June 7, the ascending hypocenters stalled. For the next three weeks, hypocenters held their depth while migrating laterally back in the direction they began. Focal mechanisms during the first part of the swarm reflect the increased stress caused by dike inflation. Following June 7, the stress orientation changes and becomes more consistent with the inflation of horizontal sill-like structures. Though only limited information is available from the seismic swarm preceding the 1943 eruption, several features, including the swarm duration and magnitude relationships, are comparable to the 2006 episode. The strong indicators of a magmatic origin to the 2006 swarm suggest that at this location there are few, if any, traditional seismic discriminants that could be used to distinguish which seismic swarms and dike emplacement events might culminate in eruption.

### 4.2 Introduction

Seismic swarms are commonplace at volcanoes. They can be caused by magmatism, glaciers, hydrothermal systems and regional tectonics. Earthquake depths and locations are sufficient to rule out most surficial processes, leaving volcanic and tectonic explanations for most swarms occurring at least a few kilometers below the surface. Interpreting these deeper swarms is a primary task in

---

<sup>2</sup>Gardine, M., West, M., Cox, T., In Review. Dike emplacement near Parícutin volcano, Mexico in 2006, Bulletin of Volcanology.

volcano monitoring. Arguably, these swarms remain the one phenomenon that is nearly always observed prior to explosive volcanic eruptions. While eruptions are accompanied by earthquake swarms, the reverse is not always true. Most earthquake swarms at volcanoes do not portend eruption. Because of this one-sided association, and the high cost of forecasting eruptions that do not occur, numerous techniques have been pioneered to distinguish various swarm mechanisms. Exotic sources, such as long period earthquakes suggestive of fluid resonance (Chouet and Julian, 1985) and multiplet earthquakes associated with conduit processes (Moran et al., 2008), suggest the occurrence of specific volcanic processes. However, such exotics are unusual and rarely the dominant source in swarms below the edifice. The vast majority of swarm crises are driven by increases in the rate and size of so-called volcano tectonic earthquakes - a catch all term for double couple earthquakes presumed to be sourced by the brittle failure of rock.

These swarms may be driven by the arrival of new magma from depth, latent degassing of older magmas, in situ thermal expansion or contraction, and the deep penetration of hydrothermal fluids. Swarms may also have regional tectonic explanations unrelated to magmatism. The challenge for responding scientists is to distinguish between different explanations while a swarm is still unfolding, often with the specific goal of assessing eruptive potential. This is largely accomplished by determining whether or not the swarm is caused by the movement of magma. Observations that have proven to be valuable discriminants of magmatic activity include: magnitude vs. time patterns which can be used to distinguish volcanic swarms from aftershock sequences; b-value magnitude parameters that can suggest a role for fluids or thermal transients; shallowing hypocenters which may indicate the ascent of magma or gas; lateral hypocenter migration within a vertical plane implying dike-like structures; and focal mechanisms and stress patterns consistent with dike injection. When several of these observations converge, they suggest reactivated volcanism, such as at Piton de la Fournaise in 1998 (Battaglia et al., 2005). Whether or not they constitute a volcanic crisis, is largely a function of the social response.

We present details of a major volcanic earthquake swarm, with over 300 located earthquakes, near Parícutin volcano, Mexico, from May - July 2006, with all of the above indicators for magma. The swarm occurred in the Michoacán - Guanajuato Volcanic Field, an ideal type locality for spontaneous volcanic eruptions. And yet this event did not end in eruption. It passed with little fanfare and is, in fact, not an uncommon occurrence in the region. It is a sobering example that while great

strides have been made in assessing the presence of active magmatism in the upper crust, there are few seismic swarm observables that can be applied broadly as reliable harbingers of eruption.

### 4.3 Geologic Setting

Parícutin volcano is the most recently active monogenetic cinder cone in the Michoacán - Guanajuato Volcanic Field (MGVF), located in the Trans-Mexican Volcanic Belt. The 1943 eruption of Parícutin is well-known as it created a new cinder cone in what had previously been a corn field. The nine year eruption is documented in numerous papers summarized by Luhr and Simkin (1993). Yokoyama and de la Cruz-Reyna (1990) show that the eruption was preceded by 21 earthquakes with surface-wave magnitudes ( $M_S$ ) exceeding 3.2 based on analysis of historical records from a station 320 km away. These earthquakes began five weeks before the eruption. One week prior to the eruption, newspapers reported 25-30 felt earthquakes per day. On the day before the eruption the felt earthquake rate reached approximately 300 (Trask, 1943).

The MGVF, covering an area of 40,000 km<sup>2</sup>, is characterized by over 900 cinder cones and scattered shield volcanoes, stratovolcanoes, lava domes, and maars (Hasenaka and Carmichael, 1985). Tancitaro volcano, located approximately 10 km southwest of Parícutin, is one of the largest composite volcanoes in the MGVF, but has no holocene activity (Hasenaka, 1994). The San Juanico-Buenavista fault is a northwest-southeast trending left-lateral oblique fault that passes roughly between the two volcanoes (Pacheco et al., 1999).

Volcanism in the region is due to the subduction of the Rivera and Cocos plates along the Middle American trench. A series of north-to-south trending grabens around the MGVF put the area in an extensional stress regime (Kurokawa et al., 1995). Swarms of earthquakes are not unknown in the region. In March 1997, a particularly vigorous swarm with 230 earthquakes, including five earthquakes exceeding local magnitude ( $M_L$ ) 3.9, were located between Tancitaro and Parícutin (Pacheco et al., 1999). Pacheco et al. (1999) concluded that the activity was due to tectonic movement along a series of fractures in the area or along the San Juanico-Buenavista Fault itself.

### 4.4 Data

Between January 2006 and June 2007, two concurrent seismic networks were in operation in the region to study the subduction of the Rivera plate and related volcanism in the western portion of the

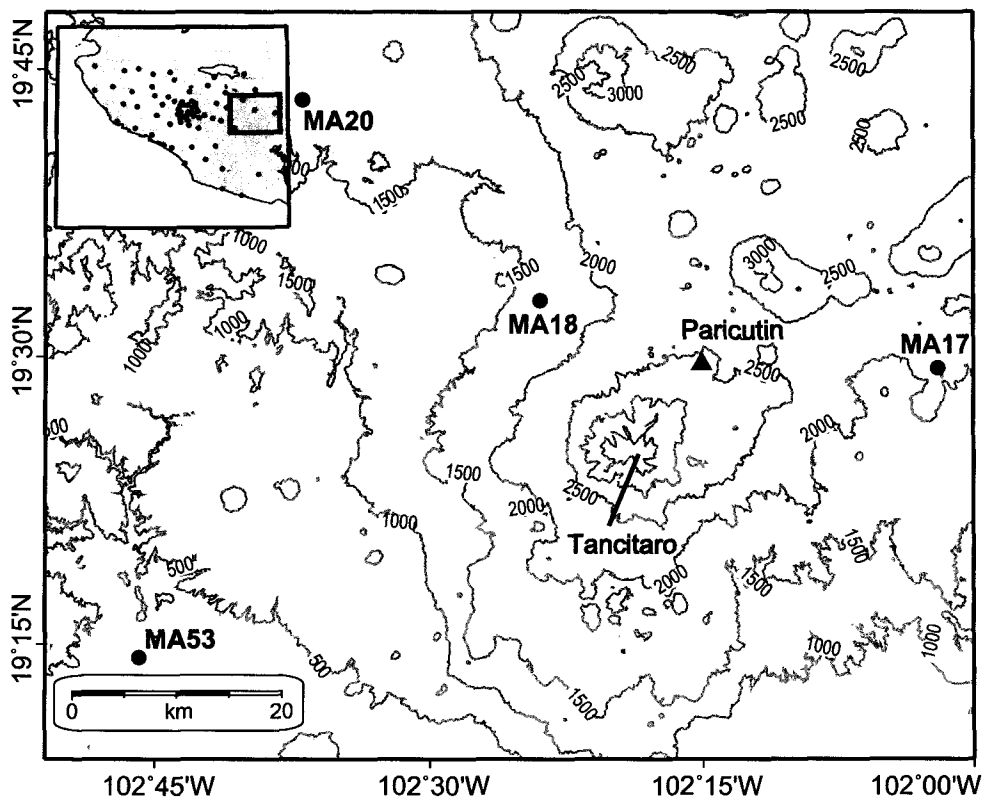


Figure 4.1: A map of MARS and CODEX seismic stations near Parícutin in western Mexico. Parícutin, a cinder cone that erupted in 1943, and Tancitaro, an eroded stratovolcano, are also shown on the map.

trans-Mexican Volcanic Belt. 50 broadband seismometers, consisting of a mix of Güralp CMG-3T and Streckeisen STS-2 sensors were deployed as part of the Mapping of the Rivera Subduction Zone (MARS) project (Yang et al., 2009) as well as an additional 20 Güralp CMG-40T sensors as part of the Colima Volcano Deep Seismic Experiment (CODEX) (Gardine et al., 2007) across western Mexico (Figure 4.1).

As part of the objectives of these projects, we created a comprehensive catalog of earthquakes using standard automated detection and location algorithms in the Antelope processing suite. Possible arrival detections were picked using a short-term average/long-term average (STA/LTA) algorithm run over all stations and channels. A rectangular grid covering the area encompassed by the network was created and P and S wave travel times were calculated from each grid node to every station. For every detection, the program searched for other detections that, based on the computed

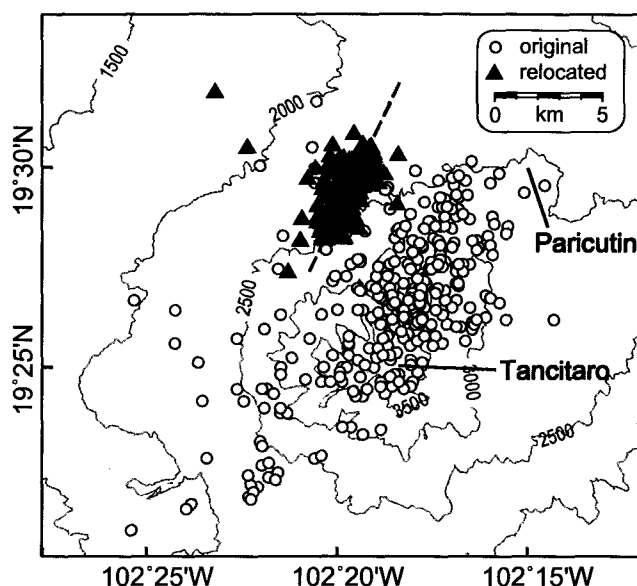


Figure 4.2: A map showing the original and double-difference relocated epicenters. Original epicenters of earthquakes are shown as circles, and relocated earthquakes using a double-difference relocation algorithm are triangles. The dashed line shows the approximate strike of the swarm.

travel time file, could correspond to an earthquake at one of the grid nodes. If at least ten detections matched, then an earthquake origin was created. In all, we created a catalog of over 4000 earthquakes throughout western Mexico from February 2006 - May 2007.

In the course of analyzing this catalog, we observed over 700 events in the Michoacán - Guajalato volcanic field from May 21 - July 2, 2006. As our detection settings required detections a hundred kilometers away, this event count is limited roughly to  $M_L$  2.5 and above. Even a conservative application of the Gutenberg-Richter relationship (Gutenberg and Richter, 1944) suggests that somewhere on the order of ten thousand earthquakes might be locatable with a handful of stations within 10 km. From the catalog, 314 of the larger earthquakes were analyzed manually; additional picks were added as needed and the earthquakes were re-located using a one-dimensional constant-velocity layer model. The epicenters of these earthquakes can be seen in Figure 4.2. Hypocentral depths varied, but were limited to the upper 15 km of the crust. Because of the large number of stations, the formal hypocentral errors were small, generally less than 3 km horizontally and 0.5 km in depth. However, the absence of stations within 10 km of the swarm suggests that the depth errors in particular are underestimated. The magnitude range of the events was between  $M_L$  2.4 and 3.7.

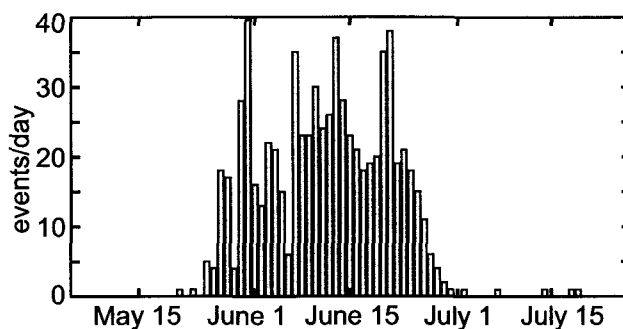


Figure 4.3: A histogram showing the number of located events per day associated with the swarm. The swarm demonstrated a sharp onset around May 21 and a rapid decay around July 1. Peak rates were around 40 events/day.

Figure 4.3 shows the daily earthquake rate during the swarm. Values peak at around 40 events / day on May 31, with the caveat that the magnitude of completeness of the catalog is quite high, around 2.6. As noted above, we would expect rates from a more traditional volcano network to exceed 10 times what is shown here. Though the detection threshold is high, the automated processing is consistent through time. Therefore, the event rates shown here are, proportionally, correct. The overall shape of the histogram is fairly representative of earthquake swarms seen at volcanoes around the world and is not typical of mainshock - aftershock earthquake sequences (Benoit and McNutt, 1996). Very little seismicity precedes May 21 or occurs after July 2. Magnitudes do not vary greatly over the duration of the swarm; earthquakes with  $M_L$  greater than 3.5 are seen in late May as well as in late June.

We calculated a b-value of 2.45 for the swarm. The b-value is calculated by finding the best-fit line to the frequency - magnitude distribution of the earthquakes using a standard weighted least squares fit, assuming the Gutenberg - Richter relation between magnitude and the logarithm of the cumulative number of earthquakes (Gutenberg and Richter, 1944). A b-value close to 1.0 is typically seen with tectonic swarms (Frolich and Davis, 1993), and higher values are often associated with volcanic environments (McNutt, 1986, Wyss et al., 1997). The observed value of 2.45 is characteristic of a magmatic origin to the swarm, and is larger than many swarms at other volcanoes (McNutt, 2005).

The strike of the swarm is in a northeast-southwest direction. Previous work by Kurokawa et al.

(1995) and Connor (1987) have shown that the MGVF is in an extensional stress environment, with the direction of maximum compressive stress being vertical. Kurokawa et al. (1995) also showed that the maximum horizontal compressive stress is in the northeast-southwest direction. Under this stress regime, we might expect a dike to open in the direction of the minimum compressive stress, i.e., towards the northwest - southeast and the dike to propagate to the northeast - southwest. This matches well with the overall shape of the observed seismicity.

#### 4.5 Hypocenter Analysis

Because the time history and magnitude characteristics were suggestive of a possible magmatic event, combined with the location of the swarm near prominent volcanoes in the MGVF, we felt the swarm merited further analysis.

To look for possible migration of the hypocenters, we carried out a simple comparison of differential arrival times between stations. Arrival time comparisons are attractive because the results are independent of the assumptions and modeling required to locate earthquakes. We show arrival times at station MA18 located to the north of the swarm, and MA53 located south of the swarm (Figure 4.4). The waveforms are aligned (time=0) on the P-arrival at MA18. For a normalized arrival time at MA18, P-waves arrive at progressively later times at MA53. This pattern is easily explained by hypocenters moving closer to MA18 and farther from MA53, showing a migration towards the north.

Since the waveforms showed a clear migration through time, we relocated the earthquakes using the double-difference algorithm of Waldhauser and Ellsworth (2000). This algorithm seeks to minimize the travel time residuals between earthquake pairs by adjusting the vector difference between the hypocenters, thereby minimizing the effect of the velocity structure on the relative earthquake locations. While this approach only minimally improves the true location of an earthquake, the relative location of adjacent earthquakes are obtained with greatly improved precision. This method has been shown to produce high-resolution structures at tectonic areas (Waldhauser and Ellsworth, 2002), as well as at volcanic settings (Prejean et al., 2002).

We used travel time differences in P and S arrivals for earthquake pairs separated by less than 10 km and used the 1-D velocity model shown in Table 4.1, assuming a constant P-to-S wave velocity ratio of 1.73. This velocity model was created by the authors using travel time tomographic

Table 4.1: 1-D velocity model for western Mexico derived from travel-time inversions.

Depth (km) to layer top	P velocity (km/s)
0.0	5.26
3.0	5.56
6.0	5.87
9.0	6.07
12.0	6.41
15.0	6.71
18.0	7.01
30.0	7.41

inversions generalized for all of western Mexico. Cross-correlated picks were not used due to the relatively dissimilar waveforms (see Figure 4.4).

Spatially, the swarm collapsed into a 3x5 km northeast-southwest oriented cloud (Figure 4.2) located just north of Tancitaro volcano and west of Parícutin, with depths between 4 and 9 km. While the relocated earthquake locations are relative and not absolute, the tight clustering is consistent over a wide range of relocation parameters in the double-difference algorithm. When the time history of the relocated events is plotted, a striking trend emerges (Figure 4.5). At the beginning of the swarm in May, earthquake hypocenters are consistently deeper (around 8 km) and occur towards the southwest. As time progresses, the hypocenters migrate upwards at a rate of approximately 230 meters/day and toward the northeast at 350 meters/day. After June 7, the events stop shallowing, remaining around 5-6 km depth, and instead begin to move southwest at around 120 meters/day. By the end of the swarm, around July 2, the events had migrated southwest to almost the original starting location, only at shallower depths (5-6 km on July 2 versus 8-9 km on May 28).

#### 4.6 Stress Patterns

Since both tectonic and volcanic activity is known to occur in the MGVF, we next analyzed focal mechanisms from P-wave first motions to look for patterns in fault planes that would indicate movement along a single fault. To find the focal mechanisms of the earthquakes, we used FPFIT, a program that computes the best double-couple fault plane solution using P-wave first motions (Reasenber and Oppenheimer, 1985). To quality-control the results, we required a minimum of

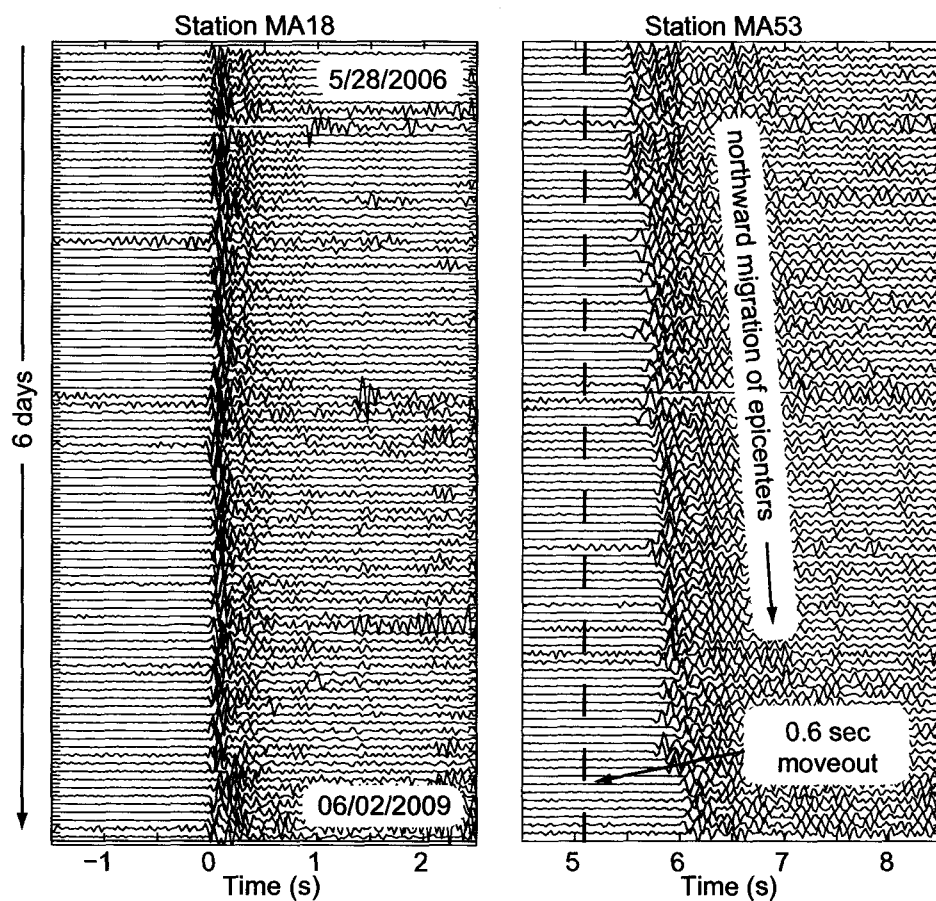


Figure 4.4: Waveforms showing P-wave arrivals from two seismic stations: MA18 and MA53. MA18 is approximately 15 km to the northwest of the swarm and MA53 is approximately 60 km to the southwest of the swarm. The waveforms have been aligned so that the P-wave arrival at MA18 is set to time=0. P-wave arrivals on MA53 show a steady moveout relative to MA18 with time over a six day period.

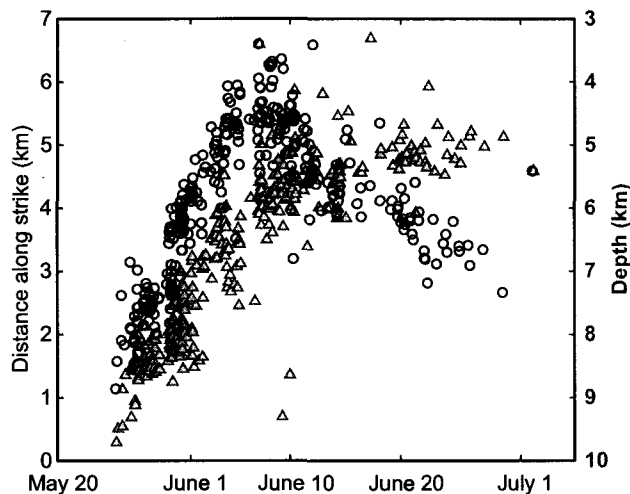


Figure 4.5: Epicentral distance of the relocated earthquakes along the strike of the swarm with time (circles). Also shown are the depths of the relocated earthquakes with time (triangles). The earthquakes show a steady migration both along strike and in depth with time.

fifteen first arrivals. Mechanisms with limited azimuthal station coverage, resulting in unconstrained fault planes, were also rejected. In all, focal mechanisms for 56 earthquakes were included in the study and are shown in Figure 4.6. If the swarm was caused by progressive movement along a fault, we would expect to see similar focal mechanisms throughout the sequence; however, no such pattern is apparent.

Due to the large variability in the focal mechanisms, we then performed stress tensor inversions of the focal mechanisms using the method of Michael (1987) to check for structure in the overall stress in the region. This method assumes that faults slip along the direction of the maximum tangential traction along the fault plane. Since the area of the swarm is small, we solve for a single stress field. The results of the inversion are the three orthogonal components of the stress tensor displayed in a lower-hemispherical projection, consistent with the focal mechanism plots (Figure 4.6). S1 is the axis of maximum compressional stress and S3 is the axis of minimum compressional stress (Weimer, 2001).

In Figure 4.5, a change in earthquake location patterns occurred around June 7 as discussed in the previous section. Based on this, the dataset was divided into two time frames: May 25 - June 6 and June 7 - July 2. Each dataset included roughly the same number of focal mechanisms, 32 for

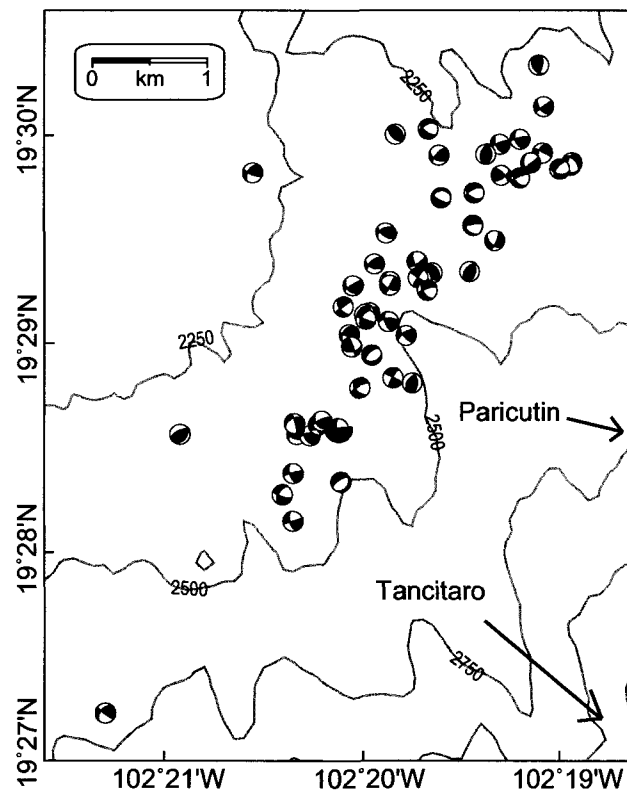


Figure 4.6: A map showing relocated epicenters for 56 earthquakes with focal mechanisms. Parícutin is located approximately 8 km east of the epicenters.

May 25 - June 6 and 24 for June 7 - July 2. Confidence regions for each inversion are calculated by using the bootstrap method with 2000 iterations (Figure 4.7). The first time period shows a reasonably well constrained maximum compressive stress in a northwest - southeast direction, while the other stress axes show variability within the strike of the swarm. This suggests that S2 and S3 are nearly equal in magnitude. During the later time period, the maximum compressive stress remains in a similar location, however, the axis of minimum compressive stress shifts to near vertical, and the null axis becomes essentially unconstrained. In a double-couple paradigm, this is suggestive of an overall thrusting environment.

#### 4.7 Interpretation and Discussion

A previous swarm of earthquakes near Parícutin in 1997 was determined by Pacheco et al. (1999) to also be aligned in a northeast - southwest direction similar to the 2006 swarm. Based on evidence shown here, we believe that the swarm in May - July 2006 was caused by the movement of magma through the upper crust. We see nearly all of the characteristics frequently associated with magmatic earthquake swarms (see Introduction). Our conceptual model of the swarm is shown in Figure 4.8.

Based on the steady migration of the swarm before June 7 over a horizontal extent of 5 km, the source of the earthquakes could be an injection of magma along a dike. Throughout this time frame, first-motion polarities were mixed between compressional and dilatational, as shown by the varied focal mechanisms of the swarm. If the earthquakes were caused by the propagation of a crack through country rock due to tensile stress, first motions should show only compressional arrivals (Chouet and Julian, 1985). However, if the intrusion occurred along an existing dike structure, then we would expect the earthquake source mechanism to be movement along pre-existing fractures around the dike, as long as ambient stress is near the existing failure envelope for fault slip (Rubin and Gillard, 1998a). Work by Roman and Cashman (2006) proposed a model whereby earthquakes are caused by an expanding dike and occur in a volume around the dike instead of just at the dike tip. The resulting stress field in this model should show a maximum compression axis that is rotated by approximately  $90^\circ$  from the regional maximum compression axis. The Parícutin swarm fits this model well. Based on work done by Kurokawa et al. (1995), the maximum horizontal compression axis in the MGVF strikes northeast. In the stress tensor inversions from both time periods, we see a

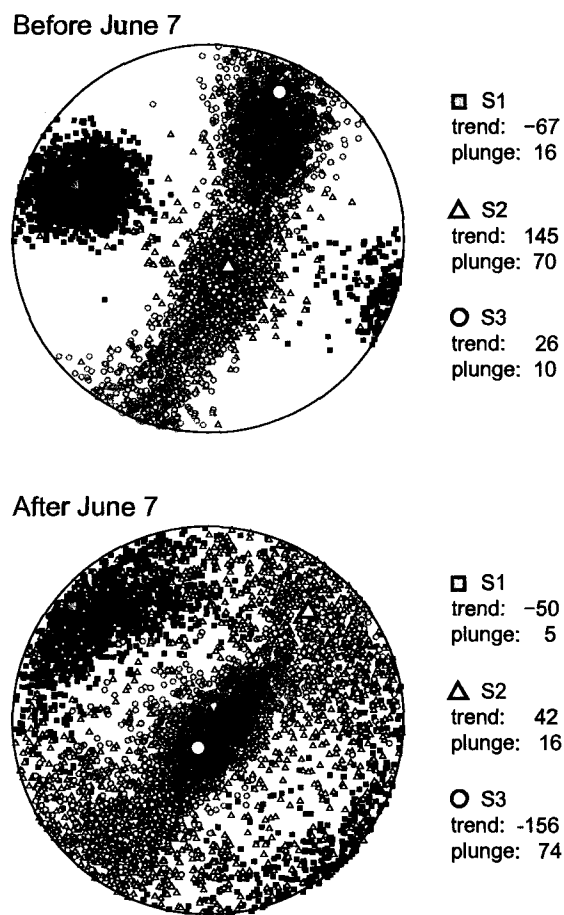


Figure 4.7: Stress tensor inversion results. The inversions used 2000 bootstrap iterations using the 32 focal mechanisms from earthquakes before June 7 (top) and from the 24 focal mechanisms from earthquakes after June 7 (bottom). S1 (square) is the best-fitting axis of maximum compressive stress, S2 (triangle) is the axis of intermediate compressive stress, and S3 (circle) is the axis of minimum compressive stress.

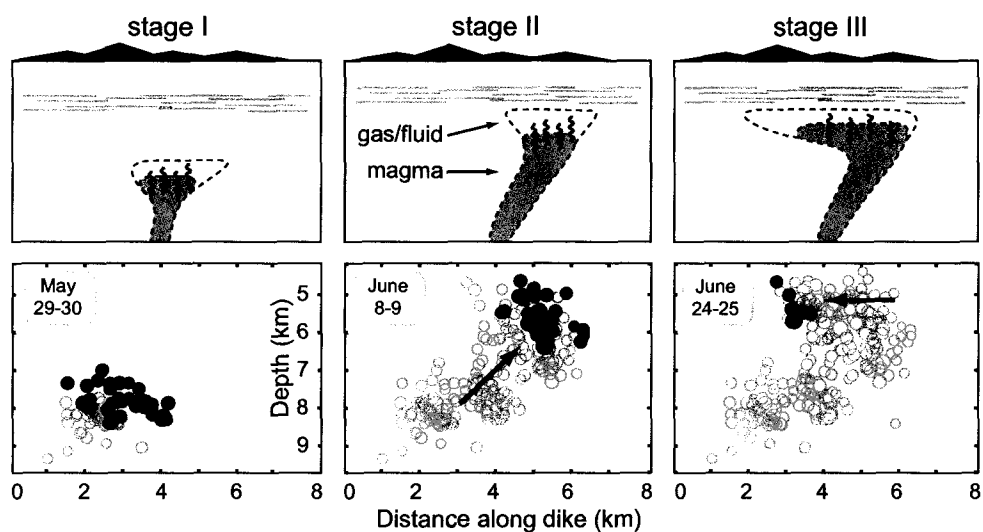


Figure 4.8: Conceptual model of the propagating dike with time (top) and the relocated hypocenters with time (bottom). Darker circles show events that occur during the given time period, lighter circles show all events that occurred prior to the given time period.

maximum stress axis striking to the northwest - southeast (Figure 4.7). The implication is that a near vertical dike opened upward to the northeast over the course of two weeks. Seismicity analyzed in focal mechanisms suggests that most of the earthquakes were in response to stresses induced in the surrounding rock. This may explain why the earthquake locations collapsed, not to a true line, but are somewhat distributed across the axis of propagation.

On approximately June 7, the hypocenters stopped the upward, northeast migration and instead remained at around 4-5 km depth and progressed steadily to the southwest. Horizontal migrations have been observed at rift zones like Kilauea (Rubin and Gillard, 1998b) and Krafla volcano in Iceland (Einarsson and Brandsdóttir, 1980). In both cases, the respective authors proposed that the earthquakes were due to magma moving through a horizontal dike or sill prior to an eruption. This type of movement into a sill explains the second stage of the swarm at Parícutin. Around 4-5 km depth, the magma reached neutral buoyancy, found a horizontal zone of weakness, or encountered a barrier to ascent. When vertical migration stalled, the magma, or the gas moving ahead of the magma, began to expand horizontally. It is possible that this occurred toward the southwest along a long narrow dike. However, a sill-like complex is more consistent with the data. Results from the stress tensor inversion after June 7 suggest this transition. The maximum compressive stress direc-

tions, S1 and S2, are less clearly defined than prior to June 7, while the minimum stress direction, S3, is well-constrained to be nearly vertical. Minimum stress in the vertical direction would be most conducive to horizontal cracks, or sills. A better conceptual explanation is to consider the stress tensor inversion as a summary of the focal mechanisms. The S3 direction is largely constrained by the portion of the focal sphere generating compressive first motions. Figure 4.7 illustrates that first motions directly above the source were predominantly compressive. This could be caused by thrust faults of varying strike, or more plausible, the inflation of a sill complex. Sill inflation is also consistent with the erratic S2 and S3 directions.

#### 4.8 Conclusion

The June 2006 Parícutin seismic swarm has all of the canonical markings of magma in the shallow crust. The 6 week sequence has rate patterns and time vs. magnitude characteristics typical of volcanic swarms, a notably high b-value, linear trend in epicenters, vertical ascent of hypocenters, steady lateral migration of hypocenters, focal mechanisms consistent with dike injection and stress patterns that evolve concurrently with hypocenter migration. Moreover, this swarm occurred in a highly expected location for magma intrusion and volcanism. The hundreds of monogenetic cinder cones in the Michoacán-Guanajuato Volcanic Field offer field proof that discrete batches of magma transit the local crust with regularity. The 1943 birth of a new volcano suggests that not only is this process still vigorous, but that magmatic intrusions and eruptions near Parícutin itself should be anticipated. Like the precursory swarm in 1943, the current swarm was active for about a month and a half. Though the magnitudes in the current swarm are about three-quarters of a unit lower, we note that the magnitude datasets come from highly divergent methods. After weeks of sustained seismicity, relatively on par with 1943 and 1997, the present swarm died out. While details of the 1943 swarm are necessarily limited, it is difficult to imagine that its precursory swarm had significantly more characteristics that demonstrated magmatic influences. In the few days immediately before the eruption, sustained tremor (Trask, 1943) and elevated ground temperatures were, in hindsight, clear markers. However, the question remains whether the deeper precursory seismic activity contained telltale signs that it would proceed all the way to eruption. The 2006 sequence suggests that, for this location, there are likely few clues from traditional earthquake methods that might foretell whether the vigorous magmatism in the upper crust would end in eruption.

### Acknowledgements

Funding for the CODEX project was provided by National Science Foundation Grant EAR-0439882. Seismic stations were provided by IRIS / PASSCAL. We would like to thank Steve Grand at the University of Texas at Austin and Jim Ni at New Mexico State University for supplying the data from the MARS array. We also appreciate the efforts of the Colima Volcano Observatory and the RESCO seismic network, in particular the work of Tonatiuh Dominguez, for help with all aspects of the CODEX array, and Gabriel Reyes for insight into regional seismicity patterns.

## References

- Battaglia, J., Ferrazzini, V., Staudacher, T., Aki, K., Cheminée, J.-L., 2005. Pre-eruptive migration of earthquakes at the Piton de la Fournaise volcano (Réunion Island). *Geophysical Journal International* 161 (2), 549–558.
- Benoit, J., McNutt, S., 1996. Global volcanic earthquake swarm database 1979-1989. United States Geological Survey Open File Report (96-69), 31 pp.
- Chouet, B., Julian, B., 1985. Dynamics of an expanding fluid-filled crack. *Journal of Geophysical Research* 90, 11,187–11,198.
- Connor, C., 1987. Structure of the Michoacán-Guanajuato Volcanic Field, Mexico. *Journal of Volcanology and Geothermal Research* 33, 191–200.
- Einarsson, P., Brandsdóttir, B., 1980. Seismological evidence for a lateral magma intrusion during the July 1978 deflation of the Krafla volcano in NE Iceland. *Journal of Geophysics* 47, 160–165.
- Frolich, C., Davis, S., 1993. Teleseismic b-values: or much ado about 1.0. *Journal of Geophysical Research* 98, 631–634.
- Gardine, M., Dominguez, T., West, M., Grand, S., Suhardja, S., 2007. The deep seismic structure of Volcan de Colima, Mexico. *EOS Transactions AGU* 88 (23), Jt. Assem. Suppl. Abstract T51A-02.
- Gutenberg, B., Richter, C., 1944. Frequency of earthquakes in California. *Bulletin of the Seismological Society of America* 34, 185–188.
- Hasenaka, T., 1994. Size, distribution, and magma output rate for shield volcanoes of the Michoacán-Guanajuato volcanic field, Mexico. *Journal of Volcanology and Geothermal Research* 63, 13–31.
- Hasenaka, T., Carmichael, I., 1985. The cinder cones of Michoacán-Guanajuato, central Mexico: Their age, volume and distribution, and magma discharge rate. *Journal of Volcanology and Geothermal Research* 25, 105–124.

- Kurokawa, K., Otsuki, K., Hasenaka, T., 1995. Tectonic stress field and fractal distribution of volcanoes in the Michoacán-Guanajuato region of the Mexican Volcanic Belt. *Geofísica Internacional* 34 (3), 309–320.
- Luhr, J., Simkin, T., 1993. *Parícutin: the volcano born in a Mexican cornfield*. Geoscience Press, Phoenix, AZ.
- McNutt, S., 1986. Observations and analysis of B-type earthquakes, explosions, and volcanic tremor at Pavlof Volcano, Alaska. *Bulletin of the Seismological Society of America* 76 (1), 153–175.
- McNutt, S., 2005. Volcanic seismology. *Annual Review of Earth and Planetary Sciences* 32, 461–491.
- Michael, A., 1987. Use of focal mechanisms to determine stress: A control study. *Journal of Geophysical Research* 92 (B1), 357–369.
- Moran, S., Malone, S., Qamar, A., Thelen, W., Wright, A., Caplan-Auerbach, J., 2008. Seismicity associated with the renewed dome building at Mount St. Helens, 2004-2005. In: Sheed, D., Scott, W., Stauffer, P. (Eds.), *A volcano rekindled; the renewed eruption of Mount St. Helens, 2004-2006*. Vol. 1750 of U.S. Geological Survey Professional Paper. United States Geological Survey.
- Pacheco, J., Valdés-González, C., Delgado, H., Singh, S., Zuñiga, R., Mortera-Gutiérrez, C., Santoyo, M., Domínguez, J., Barrón, R., 1999. Tectonic implications of the earthquake swarm of 1997 in the Michoacan Triangle, Mexico. *Journal of South American Earth Sciences* 12, 567–577.
- Prejean, S., Ellsworth, W., Zoback, M., Waldhauser, F., 2002. Fault structure and kinematics of the Long Valley Caldera region, California, revealed by high-accuracy earthquake hypocenters and focal mechanism stress inversions. *Journal of Geophysical Research* 107 (B12).
- Reasenber, P., Oppenheimer, D., 1985. FPFIT, FPLOT, and FPPAGE: Fortran computer programs for calculating and displaying earthquake fault-plane solutions. United States Geological Survey Open File Report (85-739), 27 pp.

- Roman, D., Cashman, K., 2006. The origin of volcano-tectonic earthquake swarms. *Geology* 34 (6), 457–460.
- Rubin, A., Gillard, D., 1998a. Dike-induced earthquakes: Theoretical considerations. *Journal of Geophysical Research* 103 (B5), 10,017–10,030.
- Rubin, A., Gillard, D., 1998b. A reinterpretation of seismicity associated with the January 1983 dike intrusion at Kilauea Volcano, Hawaii. *Journal of Geophysical Research* 103 (B5), 10,003–10,015.
- Trask, P., 1943. The Mexican volcano, Parícutin. *Science* 98 (2554), 501–505.
- Waldhauser, F., Ellsworth, W., 2000. A double-difference earthquake location algorithm: Method and application to the northern Hayward fault. *Bulletin of the Seismological Society of America* 90, 1353–1368.
- Waldhauser, F., Ellsworth, W., 2002. Fault structure and mechanics of the Hayward Fault, California, from double-difference earthquake locations. *Journal of Geophysical Research* 107.
- Weimer, S., 2001. A software package to analyze seismicity: ZMAP. *Seismology Research Letters* 72 (2), 373–382.
- Wyss, M., Shimazaki, K., Wiemer, S., 1997. Mapping active magma chambers by b values beneath the off-Ito volcano, Japan. *Journal of Geophysical Research* 102 (B9), 20413–20422.
- Yang, T., Grand, S., Wilson, D., Guzman-Speziale, M., Gomez-Gonzalez, J. M., Dominguez, T., Ni, J., 2009. Seismic structure beneath the Rivera subduction zone from finite-frequency seismic tomography. *Journal of Geophysical Research* 114 (B01302).
- Yokoyama, I., de la Cruz-Reyna, S., 1990. Precursory earthquakes of the 1943 eruption of Parícutin volcano, Michoacan, Mexico. *Journal of Volcanology and Geothermal Research* 44, 264–281.

## **Chapter 5: P-wave velocity structure of the deep crust under Colima volcano, Mexico: evidence of secondary magma storage**

### 5.1 Abstract

Resolving features in the lower crust using travel time tomography is often difficult, as ray paths, earthquake distribution, and station coverage are often lacking. Here we present results from a P-wave tomographic inversion in the area surrounding Colima volcano, Mexico, using 8660 arrivals from 299 events located by a well-distributed temporary seismic network across western Mexico as well as a denser temporary network near the volcano itself. The results of the inversion show two distinct low-velocity zones. One is in the upper 10 km under the volcano and may be caused by the Colima rift zone. The second anomaly, with peak values of 2.5% slower velocities, was imaged in the crust southeast of the volcano at depths of 15-30 km. This body may be due to partial melt and increased temperatures from a smaller, deep crustal magma source.

### 5.2 Introduction

In subduction zones, processes that are thought to occur in the deep crust can have a profound influence on the magmatism of the given region. Many of these processes, such as magma ponding in the lower crust, exhibit changes to the physical properties of the rock (such as increased temperatures and the presence of partial melt) that a technique like seismic travel time tomography is sensitive to. However, limitations in the tomographic method make sampling the deep crust difficult. Teleseismic earthquakes, with long wavelengths, often lack the necessary resolution to see local crustal features underneath a volcano, although they can be used to image features such as subducting slabs (Zhang et al., 2004, Yang et al., 2009). Local earthquakes have a higher frequency content and have been used to draw images of shallow magmatic features under many volcanos (Lees, 1992, Power et al., 1998, Yang and Shen, 2005, DeShon et al., 2007), but generally do not sample deep enough to resolve velocities in the lower crust.

Petrology and geochemistry have made the most progress in the study of magma interaction with the deep crust, with limited input from any geophysical method. Annen et al. (2006) proposed a model whereby basaltic magma ascends from the mantle wedge and is stored in "hot zones", areas

in the lower crust where magma is emplaced into sills (Figure 5.1). While in this hot zone, the magma will evolve into more silicic composition primarily through magma differentiation within the crust and mantle, or by partially melting existing crustal rocks.

In this paper, we show results from a tomographic study of the crust under Colima volcano in the western Trans-Mexican Volcanic Belt. We invert for P-wave velocities using  $\sim 200$  regional earthquakes associated with the subducting Rivera plate, and 100 shallow crustal earthquakes, recorded on 70 seismometers in western Mexico. Combining this velocity model with existing thermal data and petrologic work, we image an area of possible increased temperatures due to the presence of magma under the volcano at 15-30 km depth. We interpret this area as a possible "hot zone" formed from thousands of years of sustained magmatic interaction with the lower crust under Colima.

### 5.3 Geologic and Tectonic Background

Situated at the western edge of the Trans-Mexican Volcanic Belt (TMVB), Colima volcano is one of the most active volcanoes in North America (Luhr and Carmichael, 1980). The volcanism is due to the subduction of the Rivera and Cocos Plates under North America. Geodetic measurements have shown that the young Rivera plate is currently subducting at 4 cm/year (DeMets and Wilson, 1997), and the Cocos plate is subducting at a slightly faster rate, between 4.8 and 7.5 cm/year (DeMets and Stein, 1990). Colima volcano itself is located in the Colima Rift Zone, a large graben structure 50 km wide with rift flanks  $>1$  km above the graben floor (Allan et al., 1991, Savov et al., 2008). Figure 5.2 is a overview of the tectonic setting of western Mexico.

Colima volcano is an andesitic stratovolcano, with silica content of eruption material generally ranging between 58% and 61%  $\text{SiO}_2$  (Luhr and Carmichael, 1980, Mora et al., 2002, Savov et al., 2008). A long record of eruptions exists, spanning over 500 years (Gonzalez et al., 2002). Over this time period, the volcano has exhibited a striking cyclical pattern. The eruptive cycle typically lasts around 100 years, with a trend towards a more mafic composition, thought to be driven by magma input from the lower crust, towards the end of a cycle (Luhr, 2002, Mora et al., 2002). With the last major eruption of Colima in 1913 (Gonzalez et al., 2002), the end of the current cycle is thought to be near.

The Colima-Jalisco region is highly active seismically. Multiple large earthquakes have occurred in the area, including a  $M_W$  7.5 near the city of Colima in 2003 (Sánchez and Núñez-Cornú,

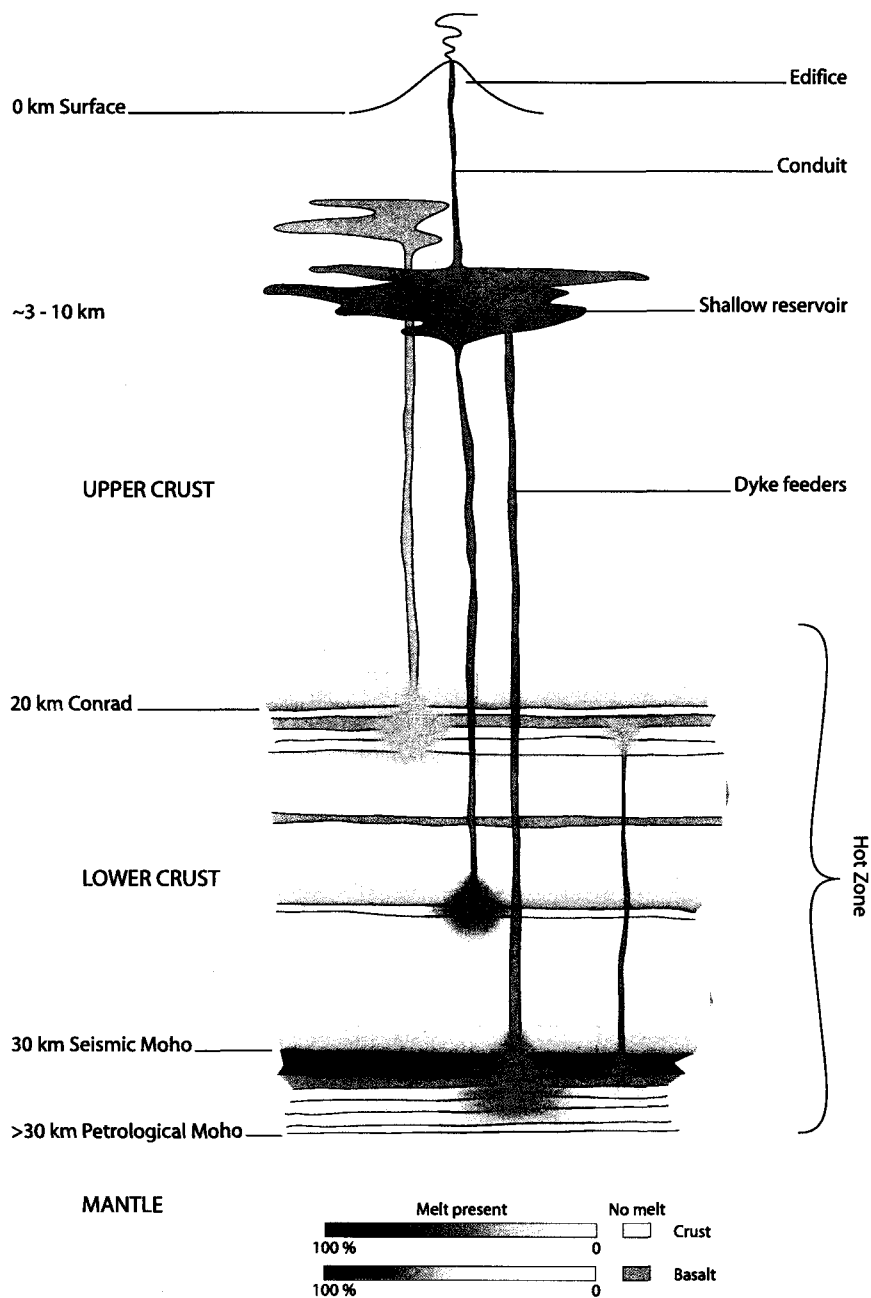


Figure 5.1: Conceptual model of a hot zone. The figure is modified from Annen et al. (2006). Magma ascends from the mantle into sills, where it crystallizes as it cools and gives it compositional variety. Melts can then rise from the hot zone into shallow magma reservoirs, where further textural and compositional variety can be added.

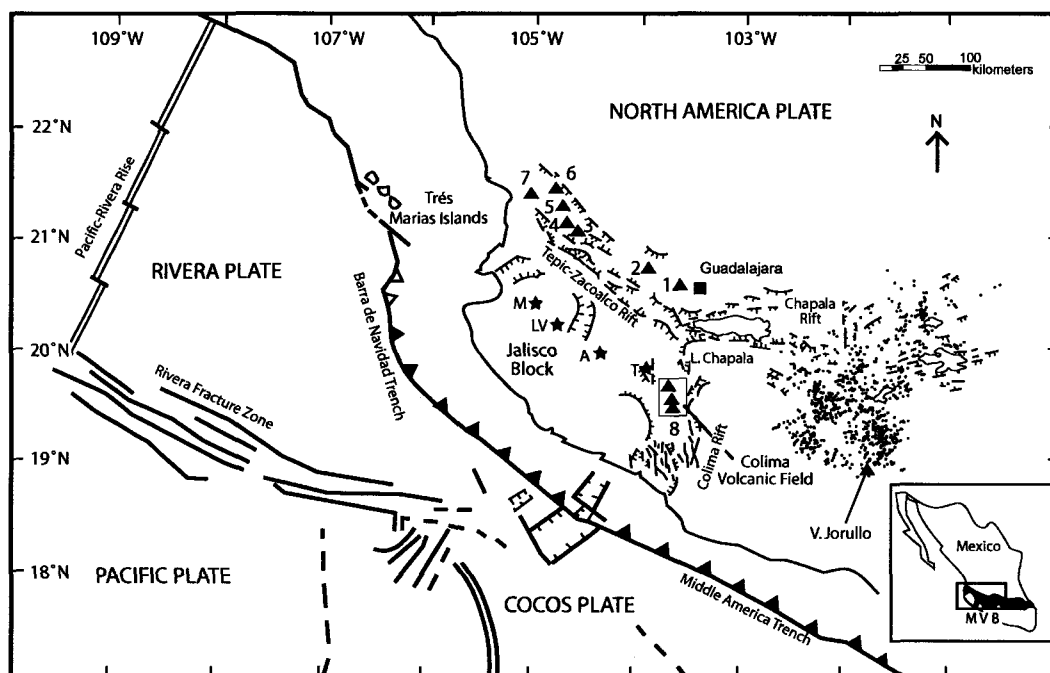


Figure 5.2: Simplified tectonic map of western Mexico. The figure is modified from Carmichael et al. (2006). The numbered triangles refer to volcanoes in the Mexican Volcanic Belt. Colima volcano is triangle number 8. The numerous cinder cones in the Michoacán-Guanajuato volcanic field are shown as solid dots located east of the Chapala Rift. The lettered stars represent towns in the area.

2009). Regional crustal and slab earthquakes are well distributed, with depths extending to around 100 km (Pardo and Suárez, 1995).

#### 5.4 Data

Two joint seismic networks were in operation between January 2006 and June 2007 in the region to study the subduction of the Rivera plate and related volcanism. 50 broadband seismometers, consisting of a mix of Güralp CMG-3T and Streckeisen STS-2 sensors were deployed across western Mexico as part of the Mapping of the Rivera Subduction Zone (MARS) project (Yang et al., 2009), with an additional 20 Güralp CMG-40T sensors near Colima Volcano as part of the Colima Volcano Deep Seismic Experiment (CODEX) (Gardine et al., 2007). Figures 5.3 and 5.4 show the configuration of the networks.

Using automated detection and location algorithms in the Antelope processing suite, we created a robust catalog of earthquakes detected by the networks. Possible arrival detections were picked using a short-term average/long-term average (STA/LTA) algorithm run over all stations and channels. A rectangular grid covering the area encompassed by the network was created and P and S wave travel times were calculated from each grid node to every station. For every detection, the program searched for other detections that, based on the computed travel time file, could correspond to an earthquake at one of the grid nodes. If at least ten detections matched, then an earthquake origin was created. In all, we created a catalog of over 4000 earthquakes throughout western Mexico from February 2006 - May 2007 (see Chapter 3 for complete details of the catalog and its creation).

From this catalog, we extracted all events deeper than 40 km for manual review. Our goal was to locate as many events related to the subducting Rivera and Cocos plates as possible, and minimize the errors associated with arrival times. These slab events were desirable for tomographic purposes due to their ray paths and their high frequency content. Tomographic methods rely on crossing ray paths through areas of interest in order to resolve the velocity structure (Aki et al., 1977). Since we were interested in the velocity structure of the crust between 20 and 40 km depth under Colima volcano, we needed rays that crossed in this area. Earthquakes below the crust are ideal for these rays (see Figure 5.5 for example ray paths). For the catalog events, false or incorrect origins were removed, any improperly picked arrivals were fixed, and any missed arrivals were added with a particular emphasis on adding arrivals on CODEX stations. In all, 198 slab-related events were

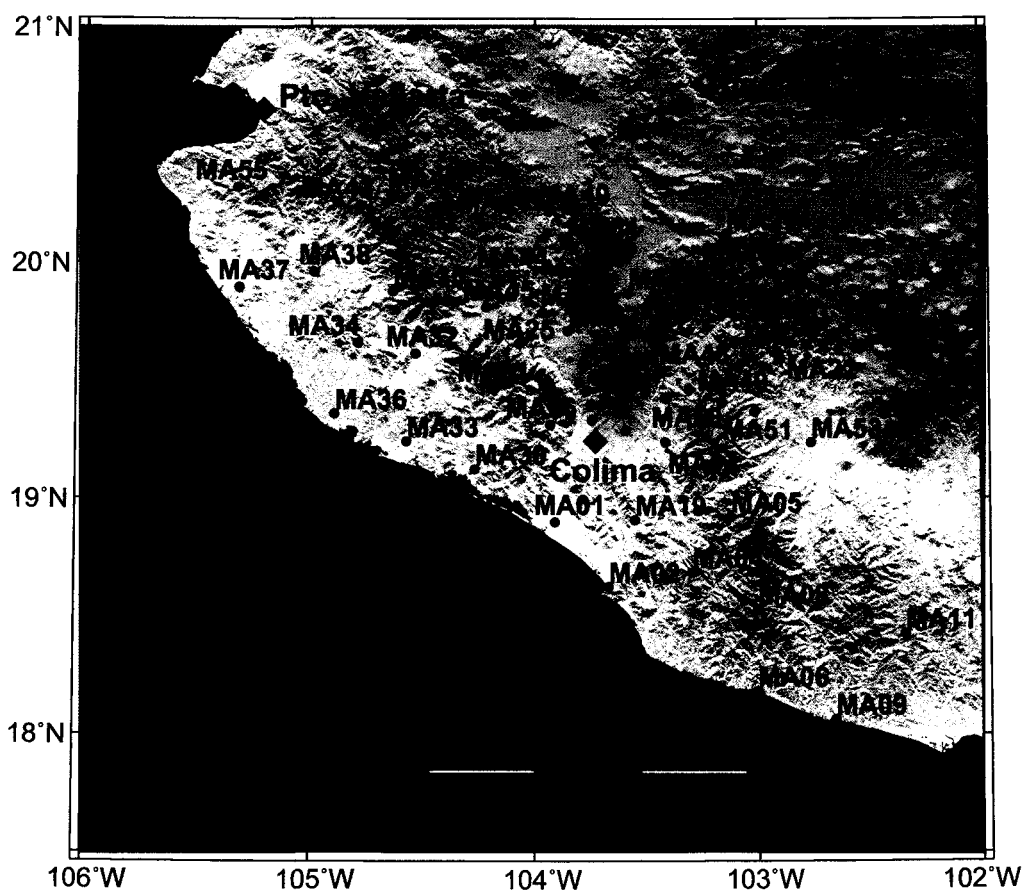


Figure 5.3: A map showing CODEX (red) and MARS (blue) seismic stations deployed in western Mexico from 2006-2008.

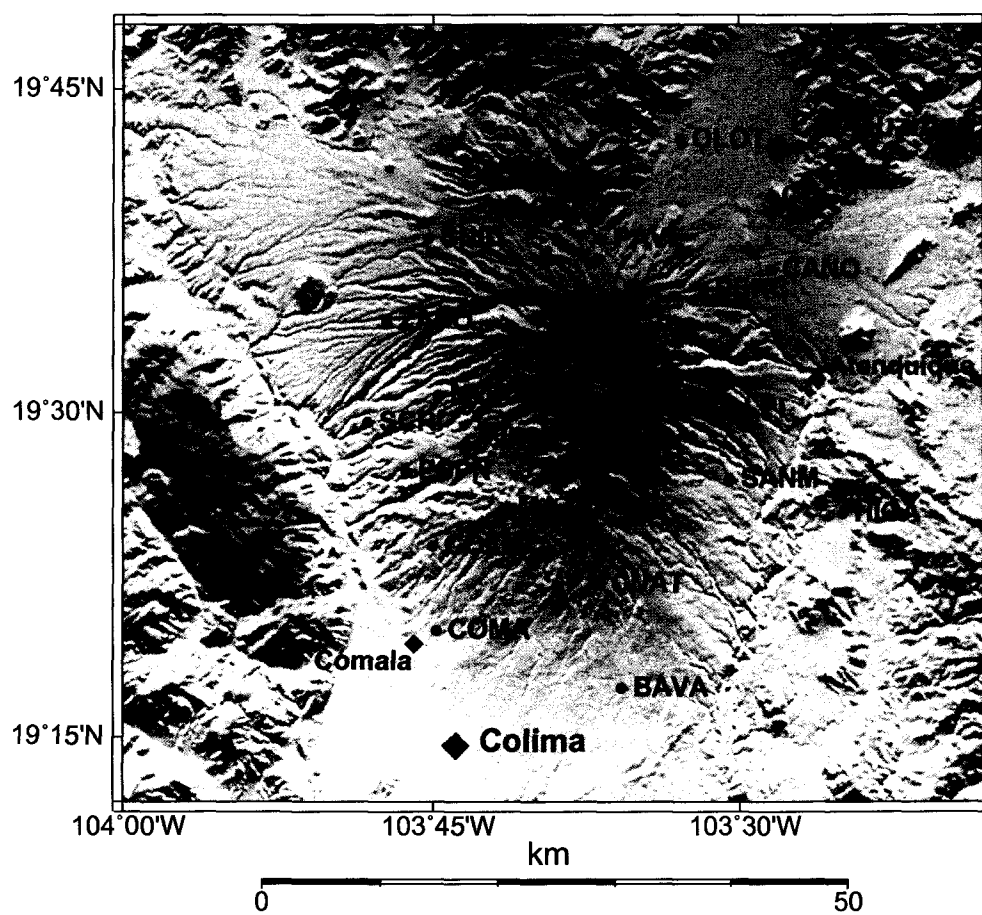


Figure 5.4: A zoom-in of Figure 5.3 showing CODEX stations (red circles). Colima volcano is located at (19°30' N, 103°37'W).

included in the catalog.

In addition, 101 earthquakes that occurred in the crust (depths less than 30 km) were included in the catalog in order to increase azimuthal coverage and to increase ray coverage in the upper crust. An epicenter map of the 299 earthquakes can be seen in Figure 5.6. The local magnitude ( $M_L$ ) of these events range from 1.5-5.1. A total of 8660 P-arrivals were obtained from these earthquakes.

### 5.5 Method

Tomography is a technique used to reconstruct an image from measurements made along rays. In seismology, the rays are approximations of seismic waves traveling through the earth, and the image returned is the velocity (or more correctly, the slowness [ $1/velocity$ ]). To create the velocity image, the area of interest, containing the sources, receivers, and the raypaths connecting the two must be discretized into three-dimensional grid cells known as voxels (Figure 5.7).

The general tomographic method is based on solving the linear inverse problem shown in Equation 5.1.

$$\vec{d} = G_{ij}\vec{m} \quad (5.1)$$

In this equation, the vector  $\vec{d}$  contains the observed travel times, the vector  $\vec{m}$  contains the unknown model slowness values, and  $G_{ij}$ , the data kernel, contains the arc length of the  $i$ th ray in voxel  $j$ . Because the data kernel is, in general, a sparse matrix (i.e., most rays do not pass through most of the voxels), and because the ray distribution is usually not perfect (some voxels have more rays passing through them than others), Equation 5.1 is a mixed-determined problem. The approximate solution to a mixed-determined problem is calculated by using Equation 5.2, the damped least squares solution.

$$\vec{m} = (G^t G + \epsilon^2 I)^{-1} G^t \vec{d} \quad (5.2)$$

In this equation,  $\epsilon$  is known as the damping parameter. Larger values of  $\epsilon$  will tend to drive changes in  $\vec{m}$  towards 0.

For the tomographic inversion carried out in this study, we used the RAYTRACE3D package, written by Bill Menke (Menke, 2005). This method jointly inverts for velocity structure and earthquake locations using the method of joint hypocenter determination and a tetrahedral representation

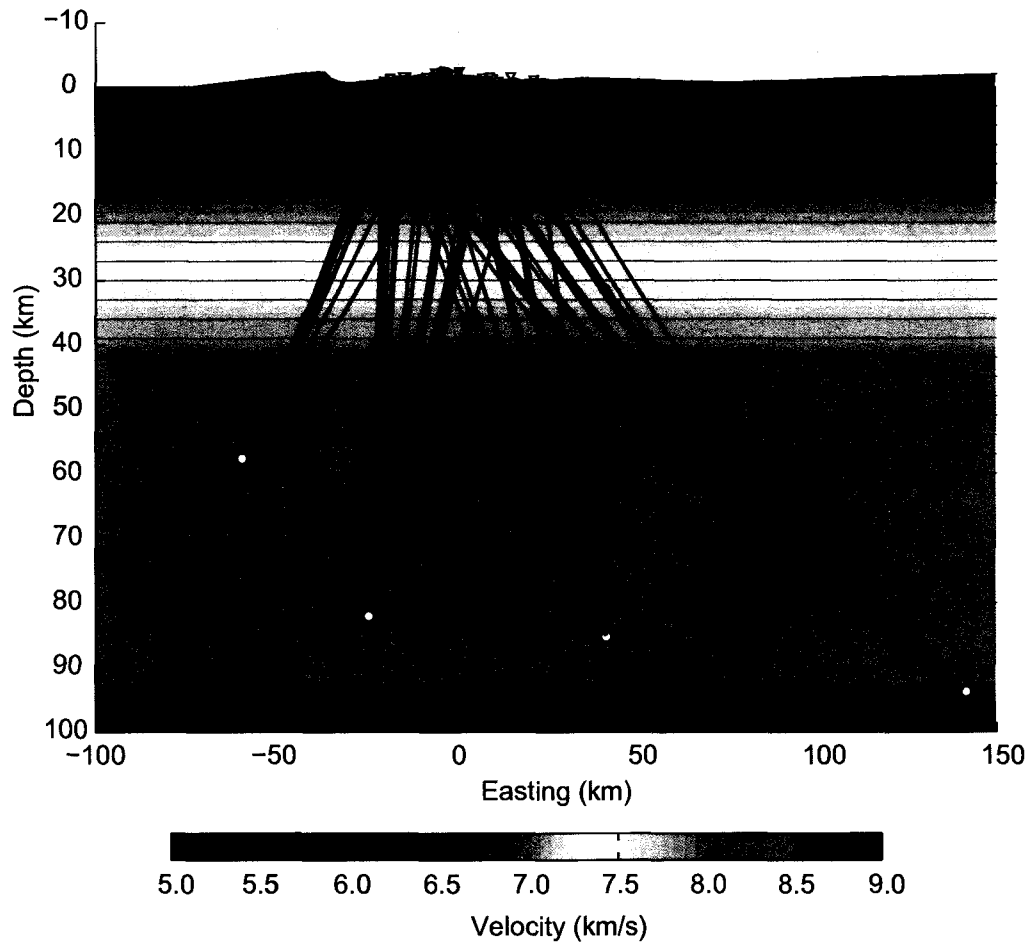


Figure 5.5: Ray paths for four slab earthquake recorded on CODEX stations. The rays were calculated using the best-fitting 1-D velocity model for the region, represented by the color scale. Depth layers are shown as the horizontal black lines. Topography was added to the top layer using 3 arc-second Shuttle Radar Topography Mission (SRTM) data.

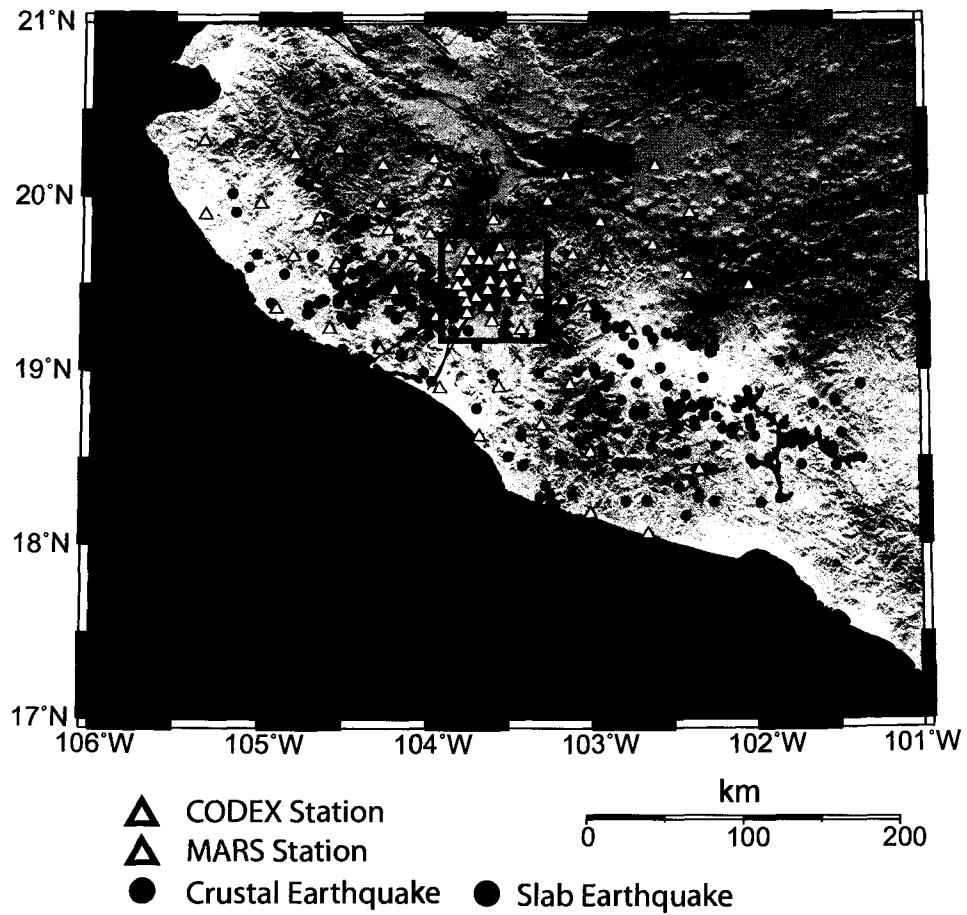


Figure 5.6: Epicenter map showing earthquakes used for the tomographic inversion. Crustal earthquakes (depth less than 30 km) are red dots and slab earthquakes are blue dots. The red box denotes the area plotted in the tomographic results.

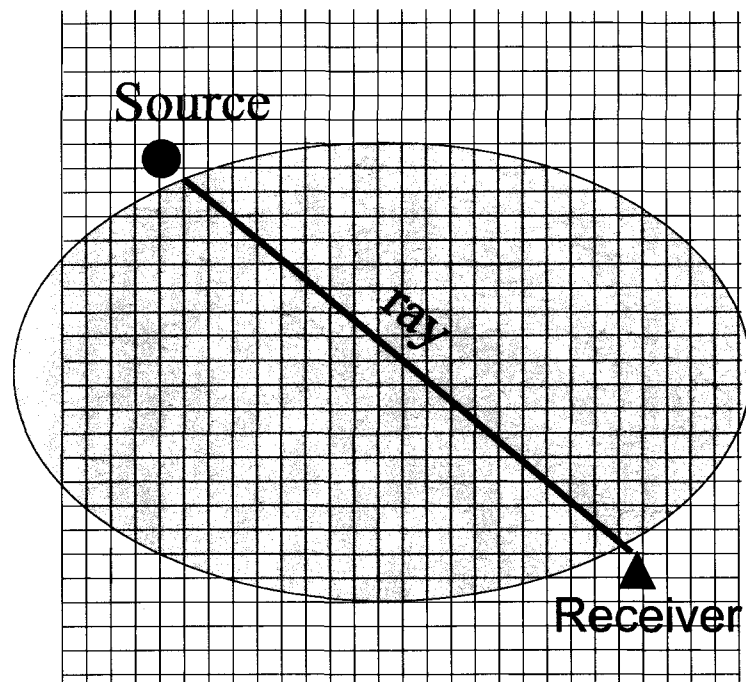


Figure 5.7: Conceptual cartoon showing a discretized tomographic model. In seismic tomography, the source would be an earthquake, the receiver would be a seismic station, and the model would be seismic velocities.

of the velocity model. Ray paths through each tetrahedra are computed analytically as an arc. The total ray path is the summation of these arc lengths from source to receiver.

The velocity structure is linearized by

$$v(x, y, z) = v_0(x, y, z) + \Delta v(x, y, z) \quad (5.3)$$

where  $v_0$  is a reference velocity field and  $\Delta v$  is a perturbation that is assumed to be small. Ray paths are calculated through  $v_0$ , with a  $\Delta v$  being computed afterward, then the whole process is iterated with an updated  $v_0$ . Like many tomography codes, the best-fitting  $\Delta v$  is found using a least-squares method to minimize travel time error. Smoothing is applied by adding a damping parameter term to the least-squares travel time error and by a method of node-tying, whereby nodes are joined together and any velocity perturbations within the joined nodes must be large enough to influence most of the nodes in the group.

The velocity model was parameterized into a grid containing 50x50 horizontal nodes from 17°N - 21°N and 106°W - 101°W. The grid was irregularly spaced with a dense grid containing 75% (37) of the nodes with 2 km spacing in an area centered around Colima Volcano, from 19.143–19.809°N and 103.951 – 103.235°W. The remaining 25% of the nodes were in a sparse grid covering the rest of the area. Topography was added to the top depth layer using 3 arc-second Shuttle Radar Topography Mission (SRTM) data. Subsequent depth layers ran from 3 to 45 km with 3 km spacing, with additional layers at 60, 80, 100, and 300 km.

The initial P-wave velocity model was derived through a 1-D inversion of the data as described in Chapter 3, and is shown in Figure 5.8. S-wave velocities were calculated assuming a standard  $V_P/V_S$  ratio of 1.73.

Ray coverage, the number of rays passing through each node as well as the direction of the rays, is very important in tomography. If too many rays are coming from the same direction, the end results tends to "smear" anomalies in the direction of the dominant rays. The number of rays passing through each node is shown in Figure 5.9. While there are more rays passing through nodes in the southern portion of the model, overall the rays are reasonably well distributed. Many CODEX stations have arrivals from a majority of the 299 earthquakes in the data set (Figure 5.10).

An iterative approach was taken for the inversion in order to ensure that the solution to the least-squares problem described in Equation 5.2 converged. Hypocenters and the velocity structure were jointly inverted for, using a damping parameter chosen by weighing the tradeoff between model

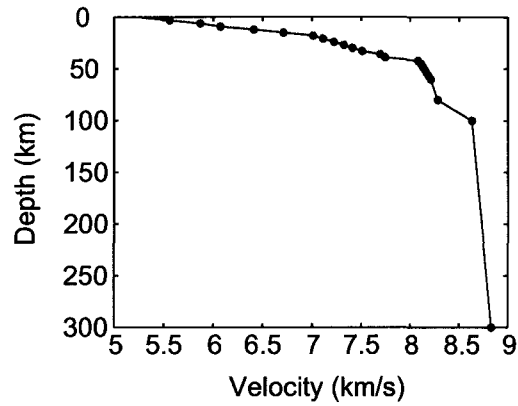


Figure 5.8: The initial 1-D velocity model used for the inversion. Velocities shown are for P-waves. Depth layers are every 3 km through 60 km depth, with additional layers at 80, 100, and 300 km. In between layers, the velocities have a linear gradient.

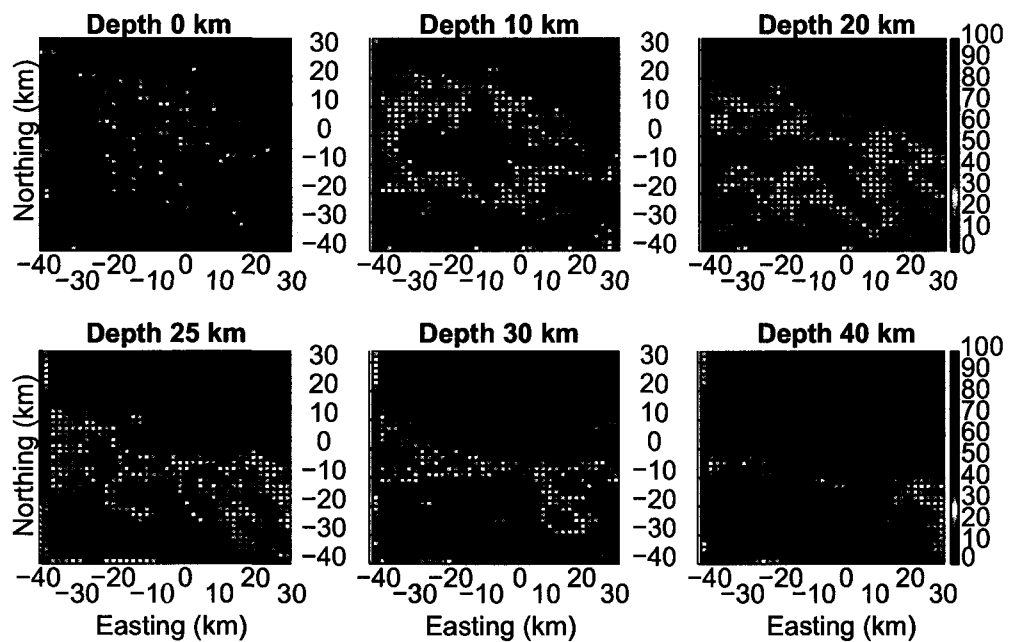


Figure 5.9: Ray hit count plot at various depth slices of the model. The color scale represents the number of rays passing through each grid node.

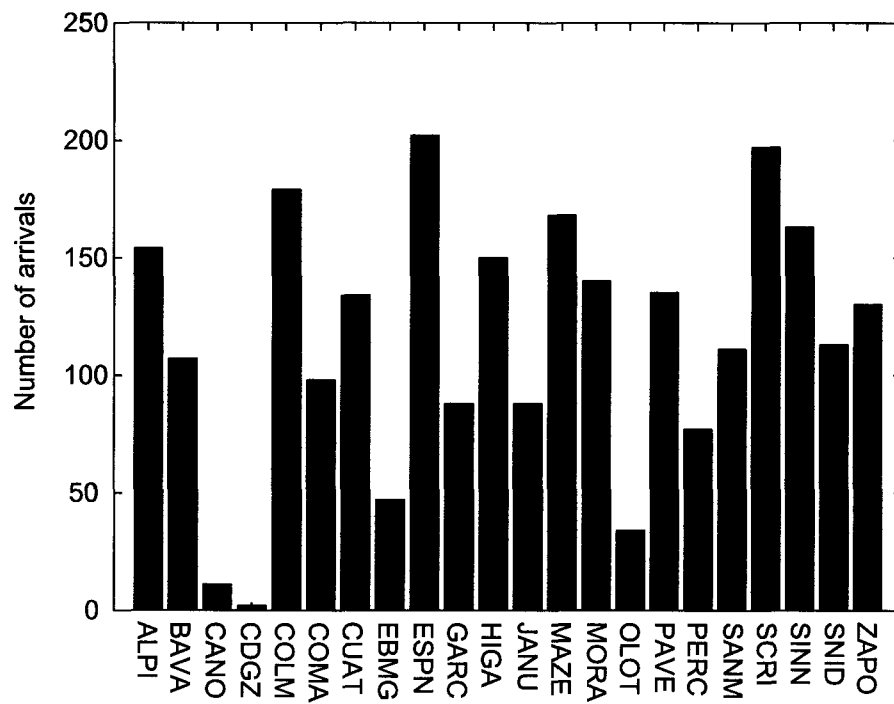


Figure 5.10: A histogram showing arrivals recorded at each CODEX station. Stations CANO, CDGZ, EBMG, and OLOT were only operational for approximately 1 year each, explaining their low number of arrivals.

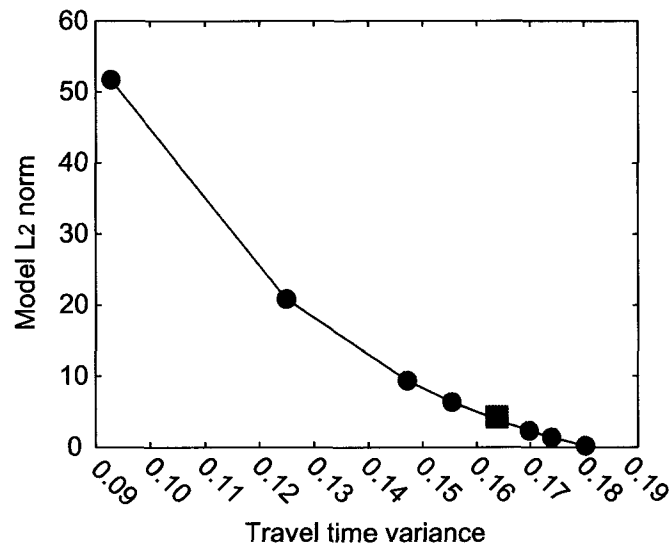


Figure 5.11: Velocity model norm versus travel time residual variance for selected damping values. The damping value selected for the inversion is shown as the blue square.

norms and travel time residuals. Figure 5.11 shows the  $L_2$  norm of the velocity model, which is a measure of the model misfit in term of the least-squares solution (Menke, 1989), versus the variance in the travel time residuals for various damping parameters. As damping increases, the norm of the velocity model decreases. This means that the magnitude of  $\Delta V_p$  of the nodes decrease relative to each other (i.e., the model is smoother). The trade-off for this increased smoothness is that variance in the travel times residuals goes up, showing that the velocity structure does not fit the real earth quite as well. The damping value of 25, shown as the blue square, was chosen as a best-fit value.

In addition to damping, smoothing was explicitly applied to the model by associating neighboring nodes together into  $3 \times 3 \times 2$  groups with equal damping and weight given to every node (effectively changing the  $\epsilon$  in Equation 5.2 for different nodes). The inversion was iterated multiple times until the travel time residuals had declined asymptotically (Figure 5.12) and was stopped at 10 iterations. In the final model, the variance of the travel time residuals was improved by 49.9% over the original 1-d model. The travel time residual root-mean squared (RMS) value was 0.3836 seconds, reduced from 0.63 seconds for the original 1-d velocity model and 0.46 seconds for the best-fit 1-d model.

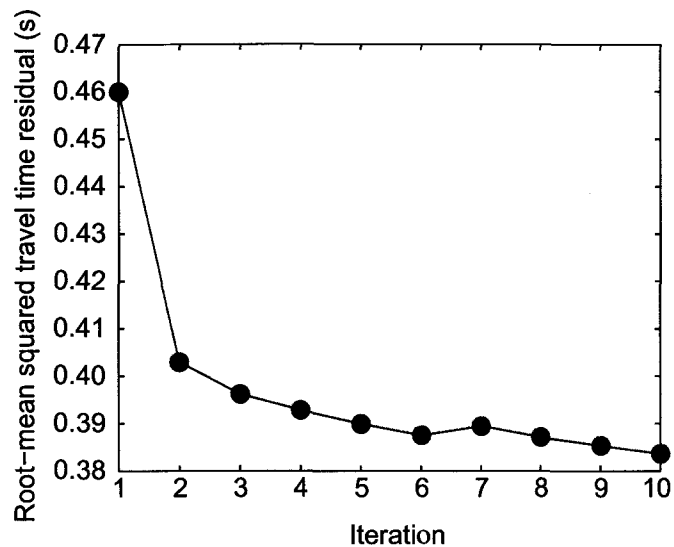


Figure 5.12: RMS travel time residuals for each iteration of the inversion. The inversion was stopped after 10 iterations, and the results from the 10th iteration was used as the final model.

## 5.6 Model analysis

The resulting velocity model from the inversion is shown in Figures 5.13- 5.18. To check for any systematic biases in the inversion, a series of statistics of the model were calculated. Figure 5.19 is a histogram showing the velocity change in each node after the inversion. Both sides of the histogram are nearly symmetric about 0. Figure 5.20 goes farther and divides the nodes by depth; the top plot shows nodes that are above 15 km depth; the bottom plot shows nodes that are below 15 km. Nodes that are shallower than 15 km, in general, have larger velocity deviations than those below 15 km. Finally, Figure 5.21 compares nodes that are within the dense grid near Colima versus nodes that are outside in the sparse grid. While more nodes do not change velocities after the inversion in the sparse grid, the two curves are generally similar. Throughout the joint inversion, hypocenters only moved by an average of 200 m from their starting locations.

## 5.7 Results

The crustal velocity structure under Colima volcano is shown in Figure 5.22. Two prominent P-wave low-velocity zones can be seen. The first is in the shallow crust near the volcano, with a peak velocity anomaly of 3% ( $\sim 0.17$  km/s) slower than the starting model. This anomaly covers an

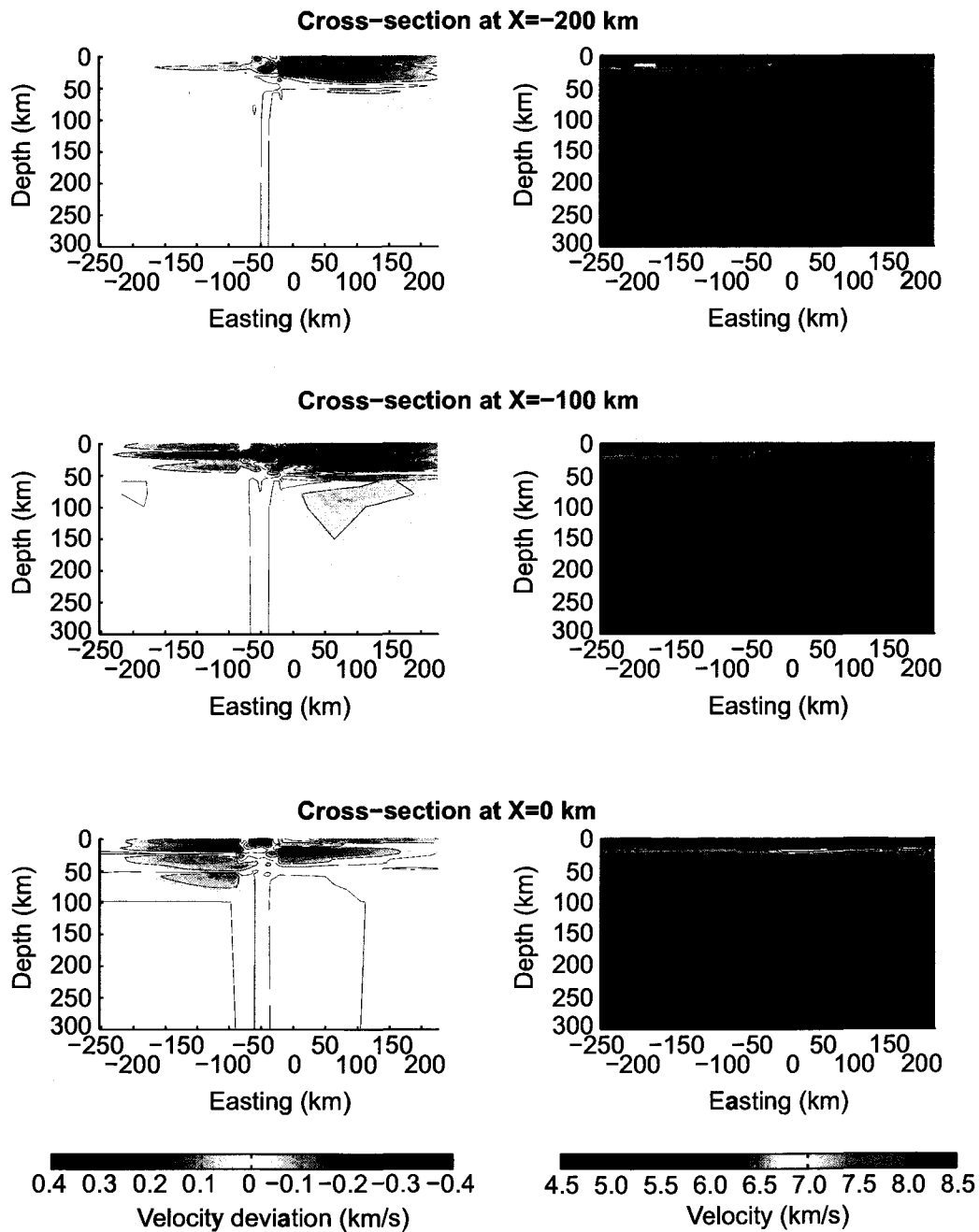


Figure 5.13: Velocity model cross-sections running south-north. For each slice, two cross-sections are plotted, (left) velocity deviation from the 1-D model and (right) P-wave velocity. Colima volcano is located at (0,0). The contour interval is 0.05 km/s for the figures on the left, 0.1 km/s for the figures on the right.

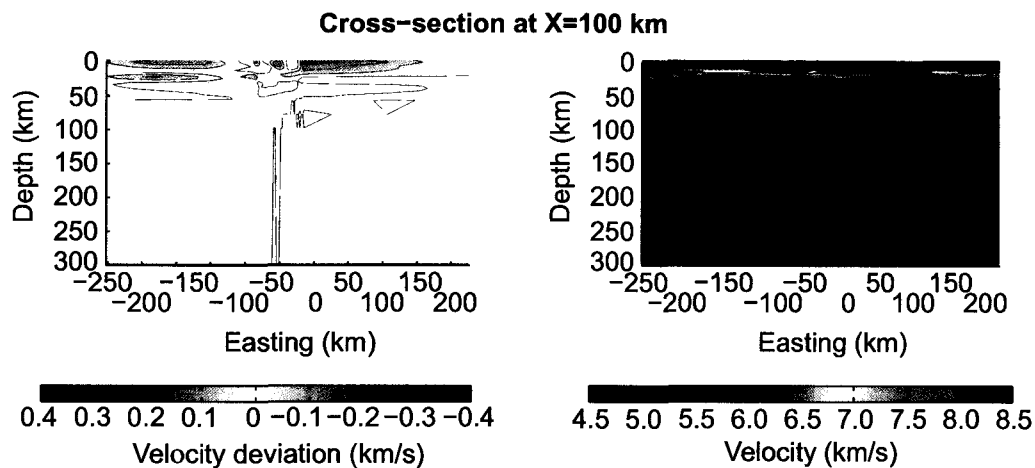


Figure 5.14: Velocity model cross-sections running south-north, continued. For each slice, two cross-sections are plotted, (left) velocity deviation from the 1-D model and (right) P-wave velocity. Colima volcano is located at (0,0). The contour interval is 0.05 km/s for the figures on the left, 0.1 km/s for the figures on the right.

area of approximately 30x30 km centered around the volcano and extends from near the surface to around 10 km depth.

A second, deeper low-velocity zone can also be seen. This anomaly is located to the southeast of the volcano and runs from around 15-30 km in depth. The peak velocity anomaly in this area is around 2.5% (approximately 0.2 km/s) slower than the starting model. In addition, an area of low-velocities appears to connect the two anomalies together.

To test the resolution capabilities of our inversion, we ran a series of resolution tests. The first test was a checkerboard test with block sizes of 16x16x6 km, containing alternating positive and negative velocity anomalies of  $\pm 1$  percent. The results of this test are shown in Figure 5.23. The inversion can adequately image high and low velocity zones in the deeper (10-30 km) crust, but degrades for features in the shallow (less than 10 km deep) crust, as well as for features below 30 km in depth.

Checkerboard tests with smaller block sizes were also tested. Blocks with thicknesses of less than 6 km were poorly resolved no matter what horizontal extents were used. This shows that features with thicknesses of less than 6 km should not be interpreted anywhere in the final model. Horizontal blocks smaller than 10x10x6 km were also not well resolved anywhere within the grid,

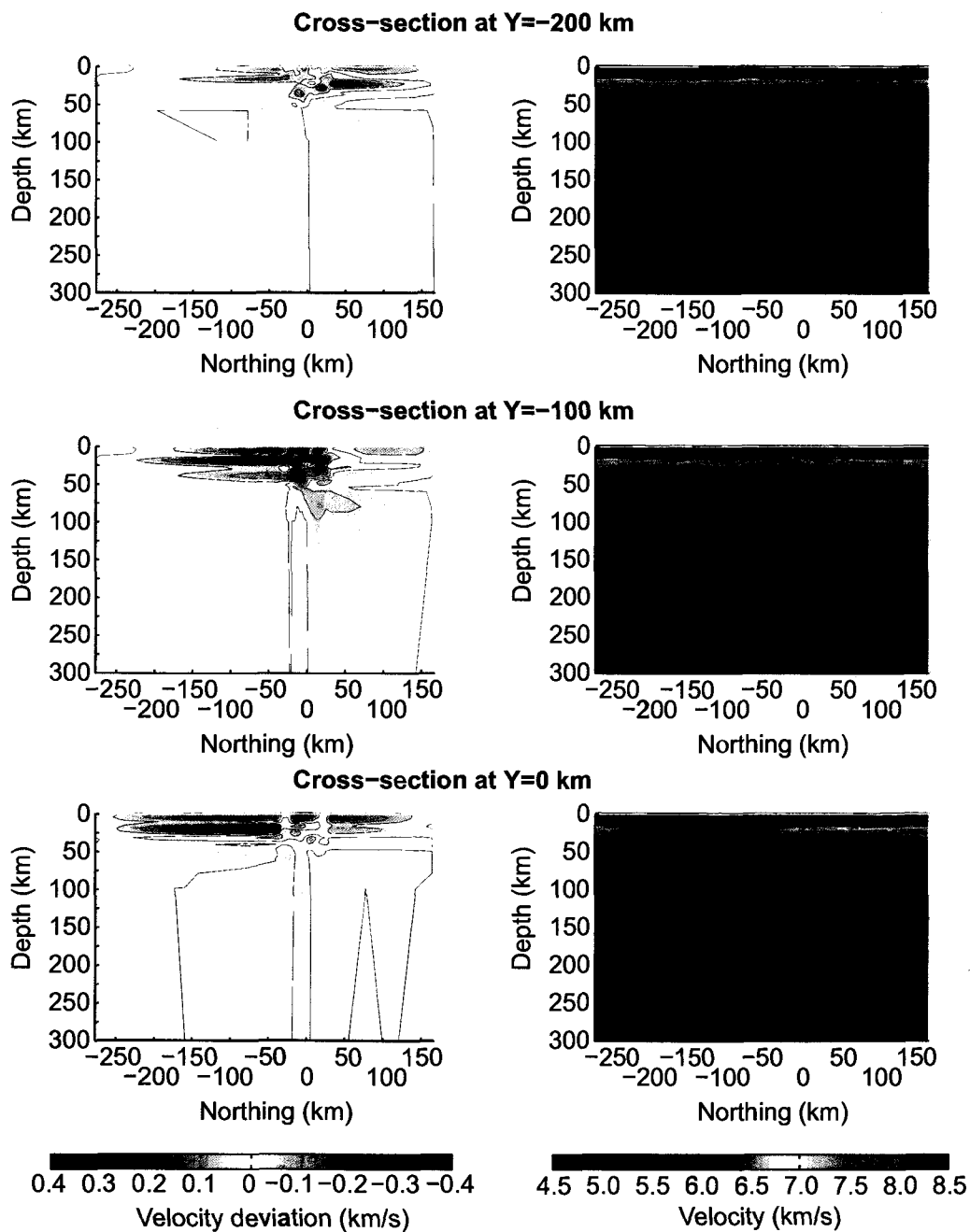


Figure 5.15: Velocity model cross-sections running west-east. For each slice, two cross-sections are plotted, (left) velocity deviation from the 1-D model and (right) P-wave velocity. Colima volcano is located at (0,0). The contour interval is 0.05 km/s for the figures on the left, 0.1 km/s for the figures on the right.

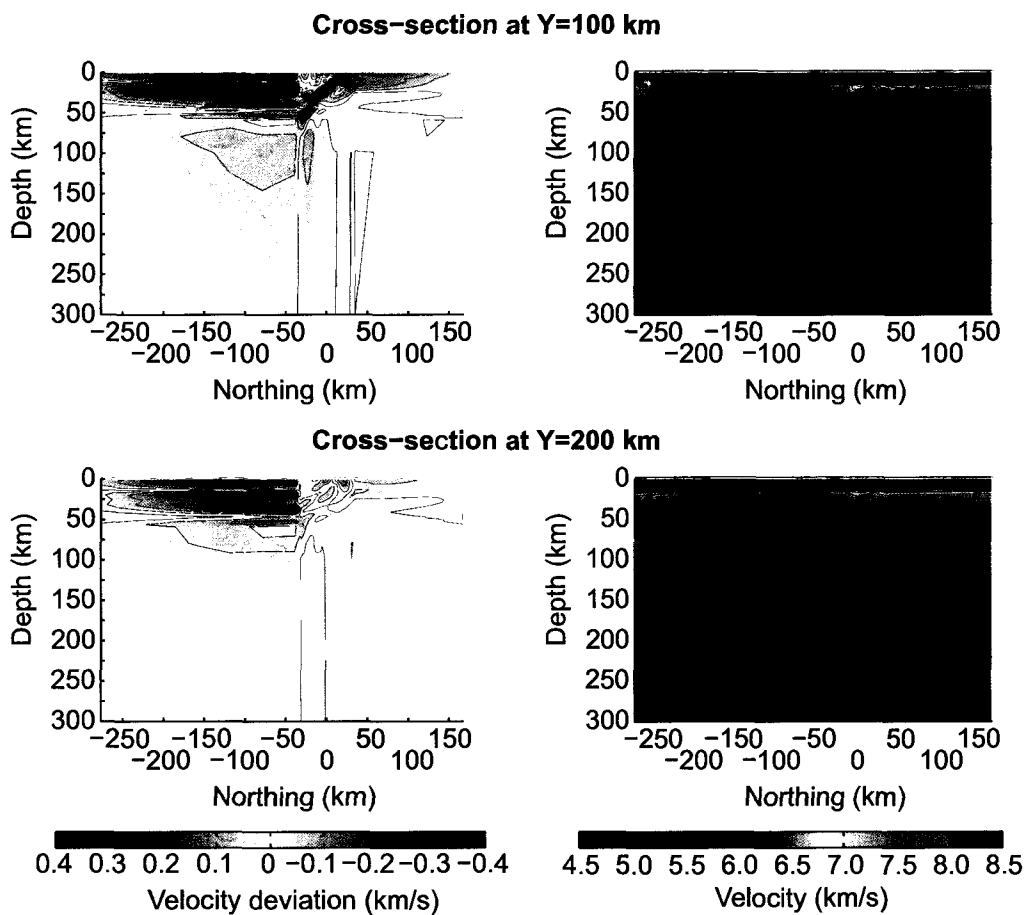


Figure 5.16: Velocity model cross-sections running west-east, continued. For each slice, two cross-sections are plotted, (left) velocity deviation from the 1-D model and (right) P-wave velocity. Colima volcano is located at (0,0). The contour interval is 0.05 km/s for the figures on the left, 0.1 km/s for the figures on the right.

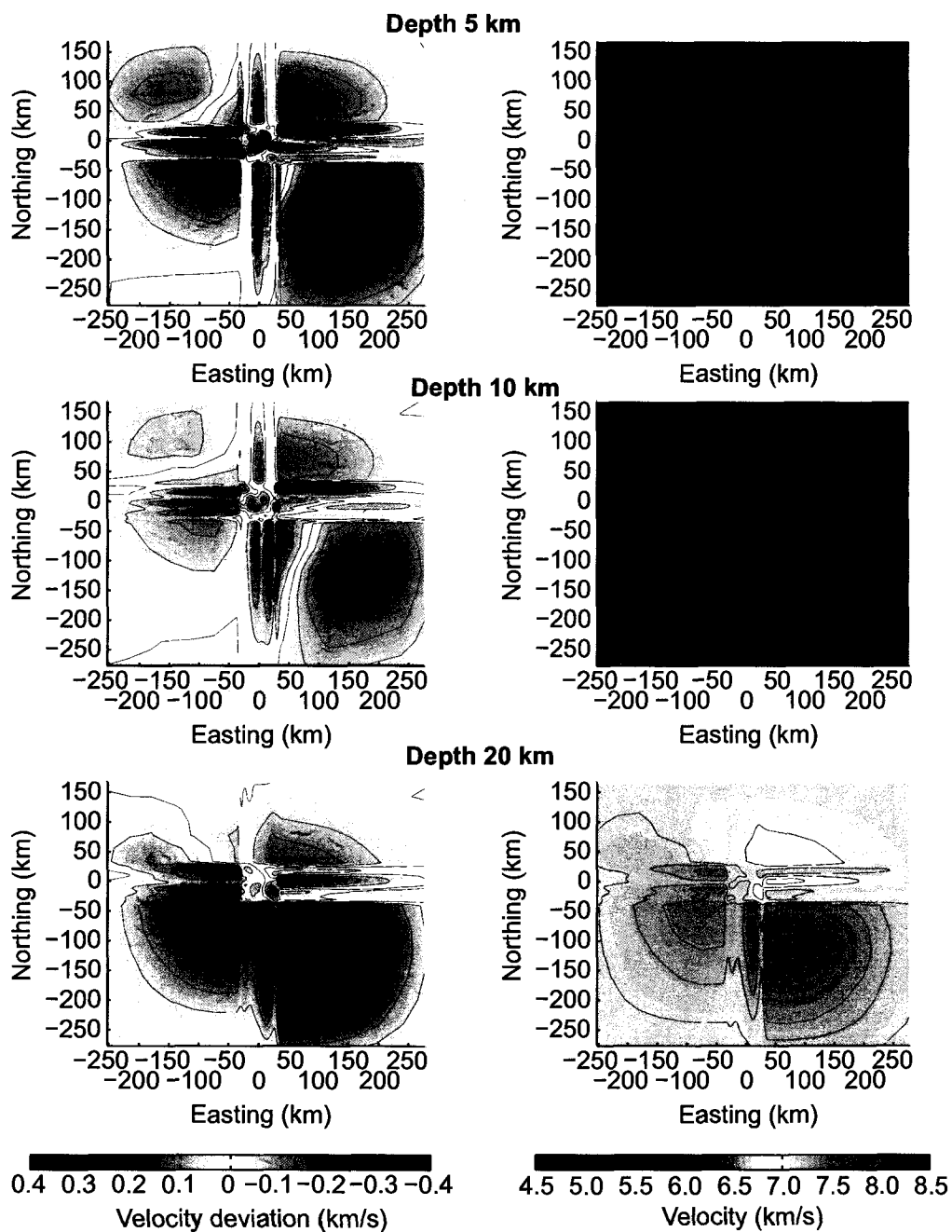


Figure 5.17: Velocity model depth slices. For each slice, two cross-sections are plotted, (left) velocity deviation from the 1-D model and (right) P-wave velocity. Colima volcano is located at (0,0). The contour interval is 0.05 km/s for the figures on the left, 0.1 km/s for the figures on the right.

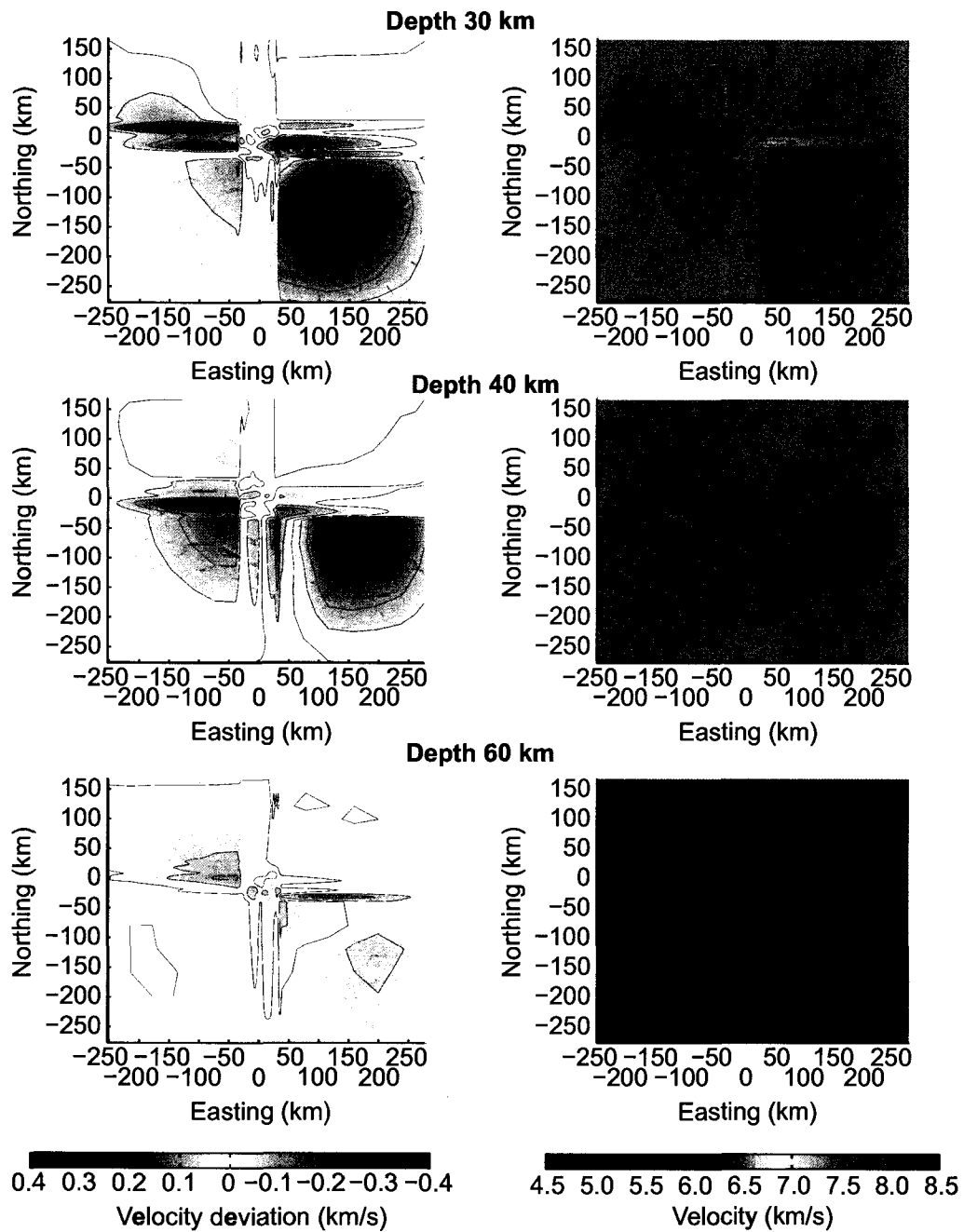


Figure 5.18: Velocity model depth slices, continued. For each slice, two cross-sections are plotted, (left) velocity deviation from the 1-D model and (right) P-wave velocity. Colima volcano is located at (0,0). The contour interval is 0.05 km/s for the figures on the left, 0.1 km/s for the figures on the right.

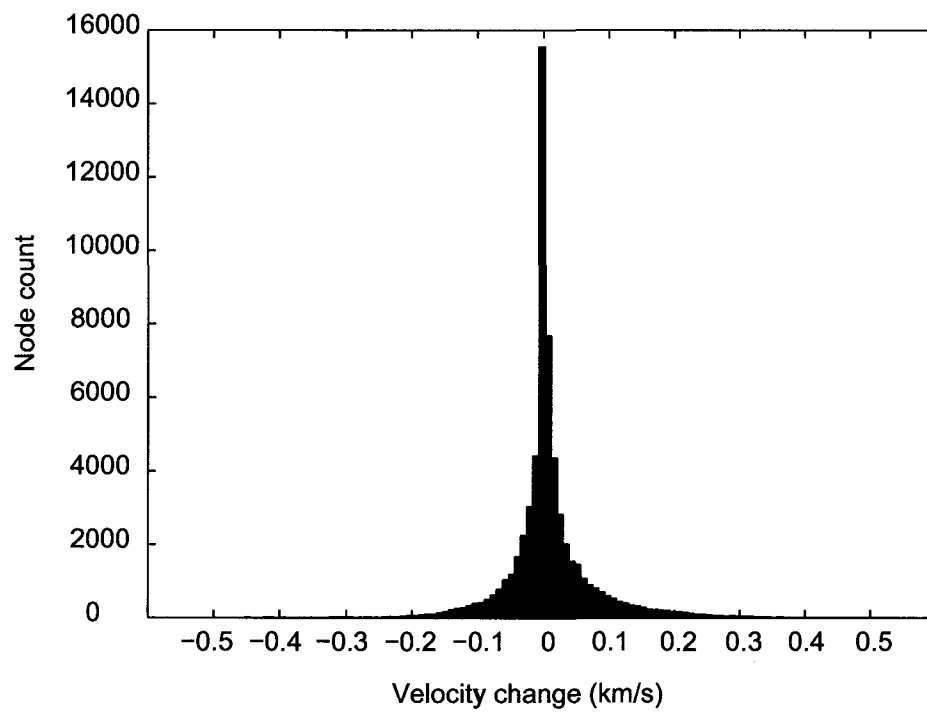


Figure 5.19: A histogram showing velocity change in the model after the inversion. The histogram peaks at -0.01 km/s velocity change. No nodes change more than  $\pm 0.4$  km/s after the inversion.

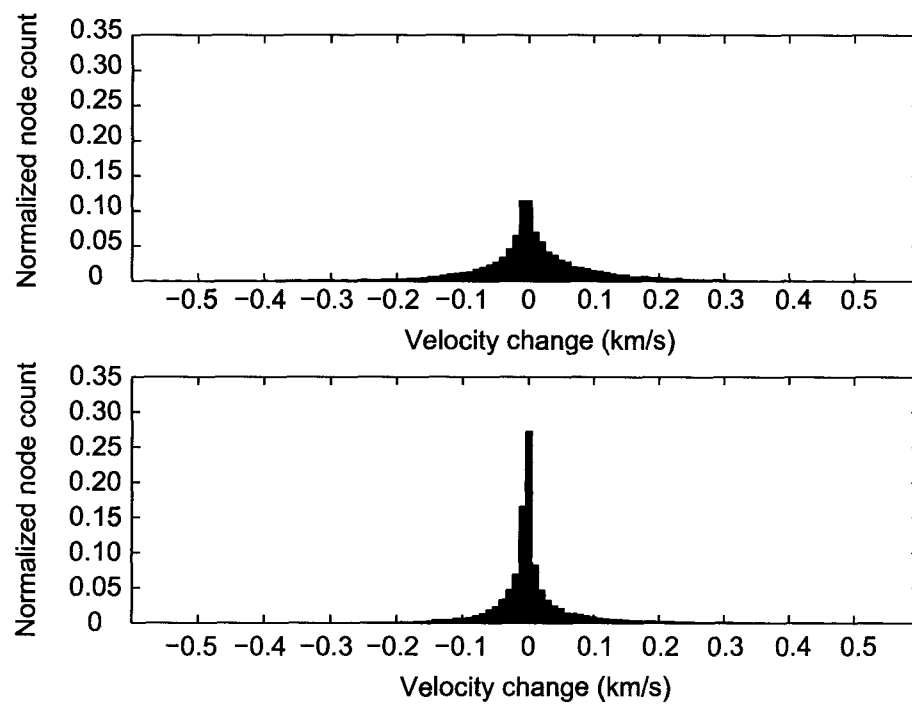


Figure 5.20: A histogram showing velocity change separated by depth. The top figure shows nodes that are above 15 km depth. The bottom figure shows nodes that are deeper than 15 km depth. The histogram counts have been normalized with respect to each other.

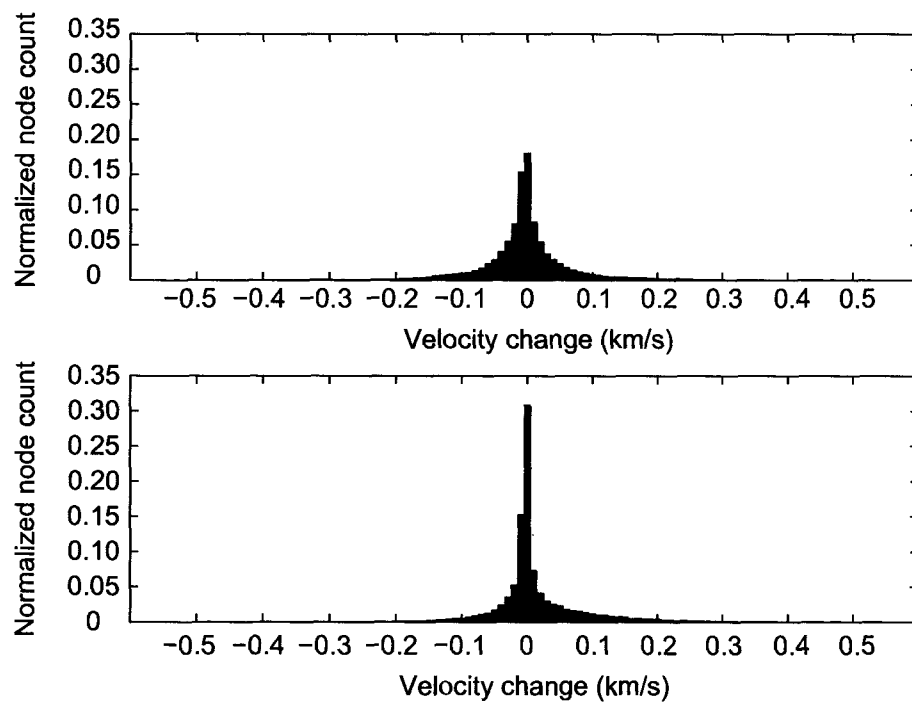


Figure 5.21: A histogram showing velocity change separated by dense grid vs. sparse grid. The top figure shows nodes that are located within the dense grid near the volcano. The bottom figure shows nodes that are outside the dense grid. The histogram counts have been normalized with respect to each other.

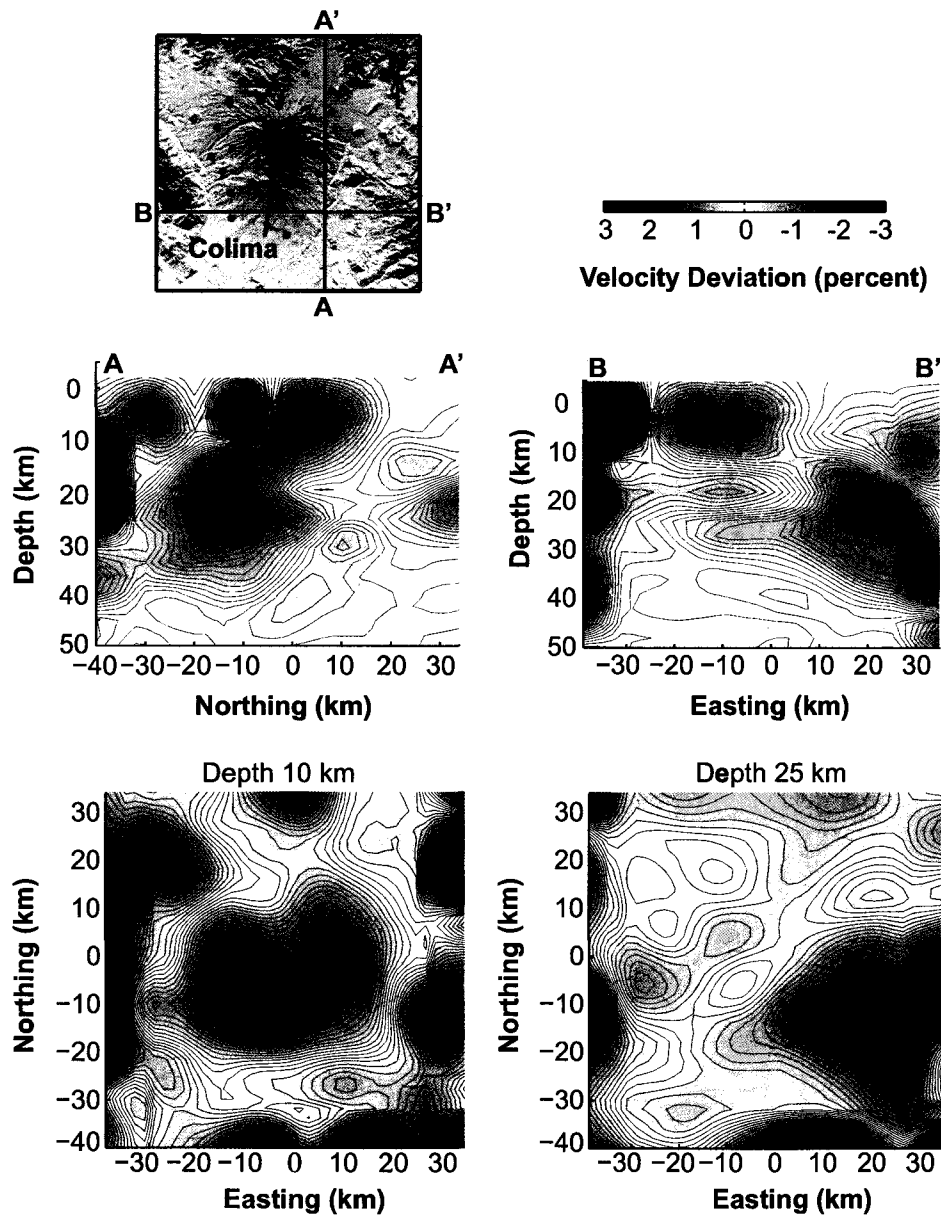


Figure 5.22: The P-wave velocity model from local earthquake tomography. Velocity deviation values are given in percent change from the 1-D model. Two cross-sections are plotted, south-north and west-east, and two depth slices at 10 km and 25 km. Colima volcano is located at (0,0). The contour interval is 0.1 percent velocity deviation.

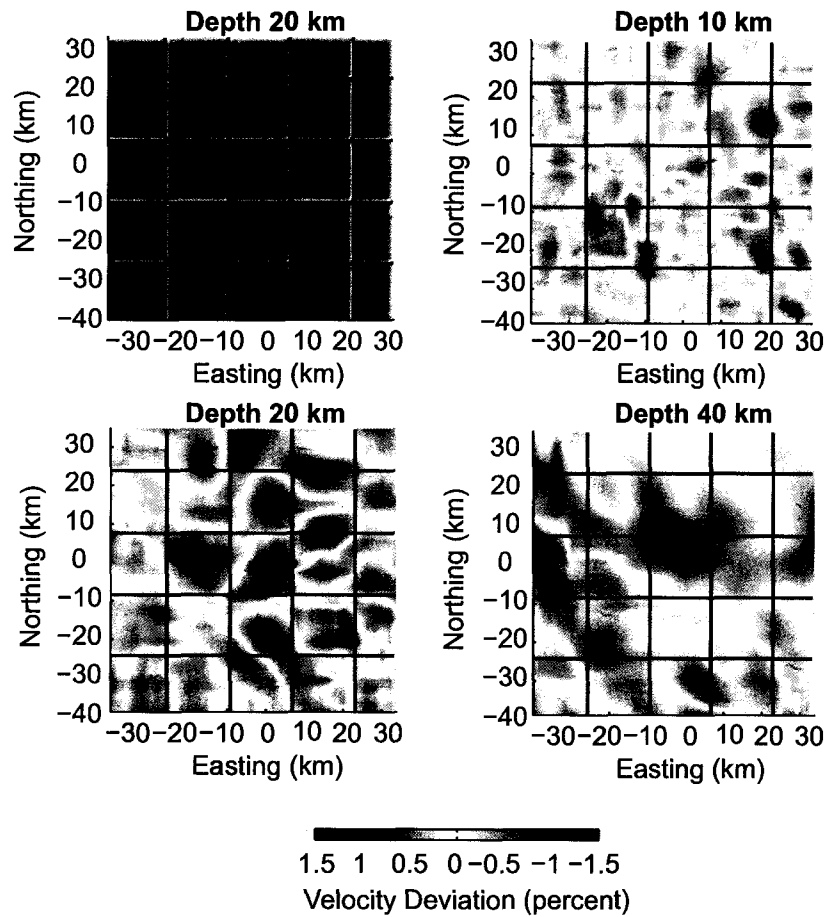


Figure 5.23: A checkerboard resolution test. (A) The original model, with alternating positive and negative 1% anomalies. The grid size for the anomalies was  $8 \times 8 \times 2$  nodes ( $16 \times 16 \times 6$  km). Shown are the inverted data at depth slices of (B) 10 km, (C) 20 km, and (D) 40 km. Colima volcano is located at (0,0).

placing a lower bound of 10x10 km horizontally on interpretable features.

The input model for the second test was a rectangular 3% slow low-velocity anomaly 20x20x12 km in size, placed in a similar location to the imaged deep crustal low-velocity zone. Figure 5.24 shows the results of this test. Overall, our data set appears to be able to resolve a feature in the lower crust similar to our results.

Because our method jointly inverts for hypocenter locations and velocity structure, we tested the influence of favoring changes to velocity versus changes to earthquake locations. We ran inversions heavily favoring both parameters, as well as giving both equal weight, and found that the resulting tradeoff was inconsequential.

## 5.8 Discussion and Conclusions

### 5.8.1 Upper crust results

The results of our inversion show two low-velocity zones in the crust under Colima volcano (Figure 5.25). The first is a shallow feature directly under the volcano. Multiple studies have also seen areas of low velocity under volcanoes such as at Yellowstone (Husen et al., 2004), Mt. St. Helens (Lees and Crosson, 1989, Waite and Moran, 2009), Katmai (Jolly et al., 2007), and others. These low-velocity zones are often interpreted as areas of high temperature and partial melt due to a magma chamber. While our tomographic inversion lacks the ideal resolution to resolve structures this shallow, it is not far reaching to hypothesize that such a magma chamber could also exist under Colima.

However, a few caveats exist with this explanation. The 0-10 km depth of the imaged anomaly roughly matches with the previously cited studies at other volcanoes, however, the volumetric extent of the low-velocity zone imaged here is much larger than in other studies (9000 km<sup>3</sup> in this study vs.  $\leq 100$  km<sup>3</sup> at other volcanoes, except Yellowstone), and has a smaller velocity anomaly (3.5% in this study vs. 5-7% at other volcanoes). A more likely explanation for the observed anomaly is due to regional geology. The area surrounding the volcano is a large graben feature due to the extension of the Colima rift zone (Luhr and Carmichael, 1980). The rift is  $\sim 50$  km wide around Colima with rift flanks  $\geq 1$  km above the base. The sediment fill of the graben would decrease seismic velocities because of lower densities and the relatively poor consolidation of materials. Conversely, the basement rock exposed on the rift flanks would show higher velocities than the graben floor.

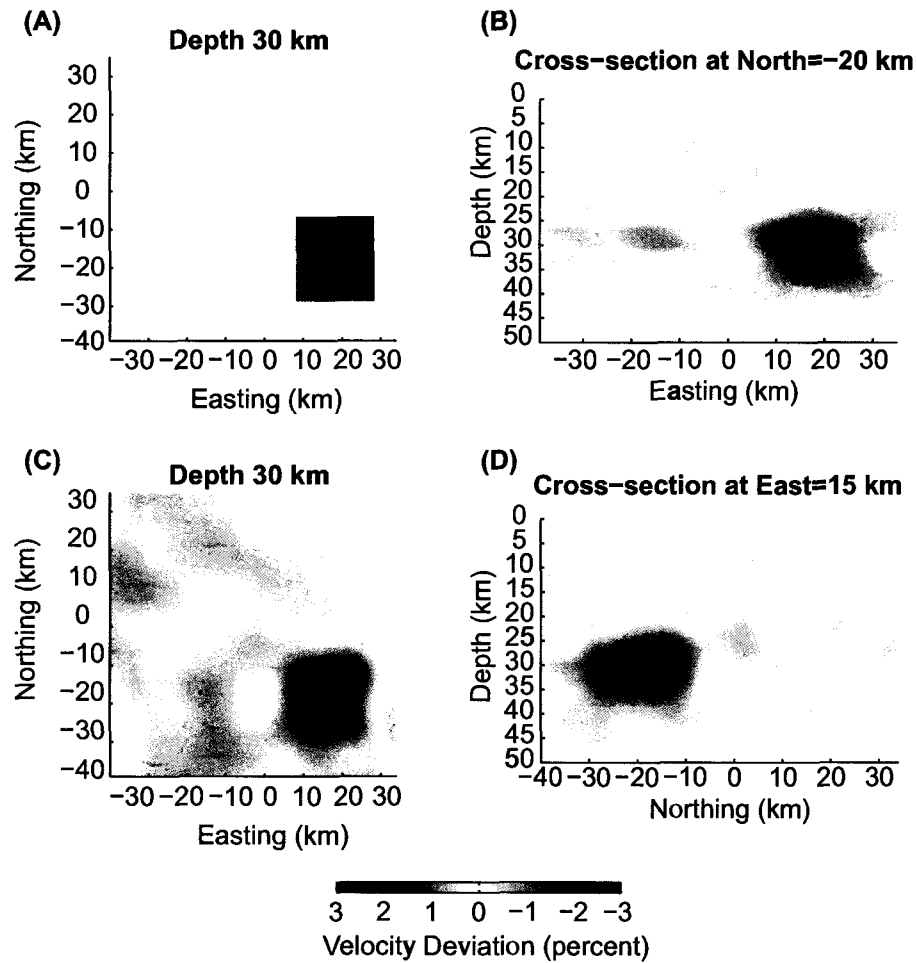


Figure 5.24: A resolution test for a rectangular anomaly in the lower crust. The anomaly had 3% slower velocities over a 20x20x10 km area, roughly located near the observed lower-crustal anomaly in the tomographic results. The synthetic anomaly has depths from 25-35 km. (A) The synthetic model, with negative 3% anomaly. Cross-sections, matching those in Figure 5.22 are shown in (B) and (D). Also shown are the inverted data at depth slice at 30 km (C). Colima volcano is located at (0,0).

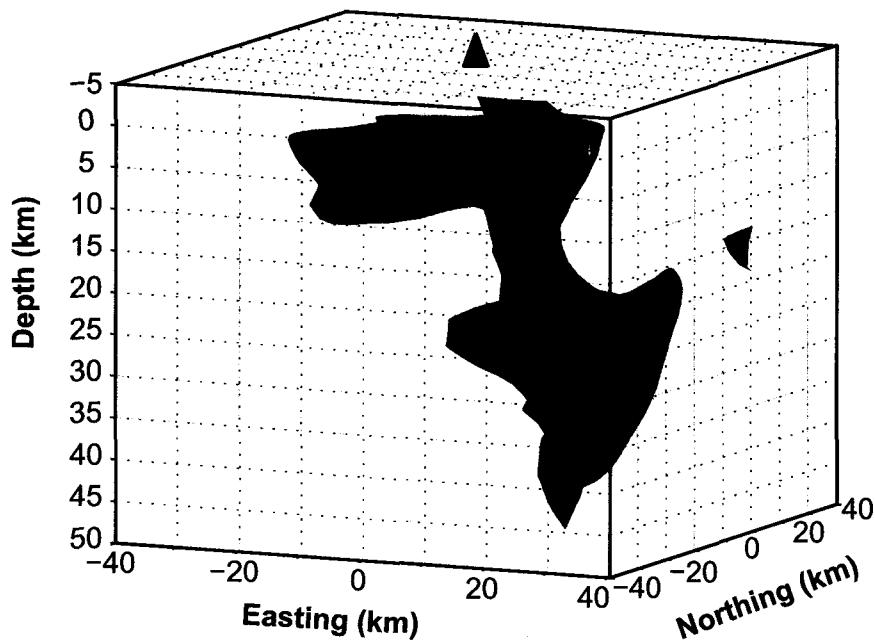


Figure 5.25: The -1.5% velocity deviation isosurface plot from the tomography results. The shallow low-velocity zone is located under Colima volcano, and runs to depths of about 10 km. The second low-velocity zone is located to the southeast of the volcano at depths of 15-30 km. Colima volcano itself is located at (0,0).

This pattern of slower velocities in the center and faster velocities on the edges is borne out in the results (Figure 5.22).

### 5.8.2 Lower crust results

The second low-velocity anomaly is located approximately 20 km southeast of the volcano and ranges in depth from 15-30 km. Peak velocity anomalies are 0.2 km/s slower than the background of 7.25 km/s in the 1-D model (2.8%). Crustal thickness in the area has been determined through receiver function analysis to be on the order of 40 km around the Colima area (S. Sudhardja, unpublished document, D. Wilson, unpublished document), placing the low-velocity zone in the lower

crust.

Annen et al. (2006) proposed a petrologic mechanism whereby magma can be stored in the lower crust in a series of sill-type structures dubbed "hot zones". These hot zones are typically long lasting, requiring 1000+ years to set up the necessary background temperatures to keep magma at or near the liquidus phase. Initial basaltic magma generation is caused by fluids released by the eastward subduction of the Rivera and Cocos plates under North America (Davies and Stevenson, 1992, DeMets and Wilson, 1997, Jödicke et al., 2006). This basalt travels upwards through the mantle wedge into the lower crust. It is in the crust where the basalt can turn into intermediate and silicic magmas through two processes: differentiation through crystallization (Grove and Kinzler, 1986, Grove et al., 2003) or by partially melting existing crustal rocks (Atherton and Petford, 1993, Izbekov et al., 2004). However, due to the increased background temperatures, the amounts of crustal inputs occurring in these zones could be varied (Annen et al., 2006).

As the mafic magma enters the lower crust, it transfers heat and volatiles into the surrounding rock. This additional heat and fluid forms an area of higher temperatures, partially molten rock, and liberated H<sub>2</sub>O (Annen et al., 2006). If such a process was occurring at Colima, seismic evidence should be in the form of increased travel times for waves passing through the hot zones, as both increasing temperatures and the presence of partial melt slow down seismic waves. Laboratory work demonstrated that in mantle olivine, P-wave velocities decrease by 0.5 m/s/°C for temperatures below 700°C (Anderson et al., 1992, Isaak, 1992) and increase variably as temperatures approach the solidus/liquidus boundary (Wiens et al., 2006). Due to dramatically increased compositional diversity, crustal rocks generally decrease non-linearly at temperatures greater than 700°C (Kern and Richter, 1981, Nishimoto et al., 2005), making the olivine values a good lower-bound estimate.

Based on these  $\Delta V_P/T$  ratios, the observed P-wave velocity reductions of 0.2 km/s could be explained by a temperature increase of approximately 400°C above background. Previous work by Currie et al. (2002) derived a thermal model for the Mexican subduction zone. In their model, background temperatures at depths of 25 km near Colima volcano should be around 500°C (Figure 5.26). The thermal model was derived numerically and attempted to fit the known parameters of the seismogenic zone such as oceanic plate age, convergence rate, and oceanic geotherms to temperature profiles. Assuming the velocity anomaly imaged is due solely to increased temperatures, these values would put temperatures in the lower crust under Colima at around 900°C. Figure 5.27 maps

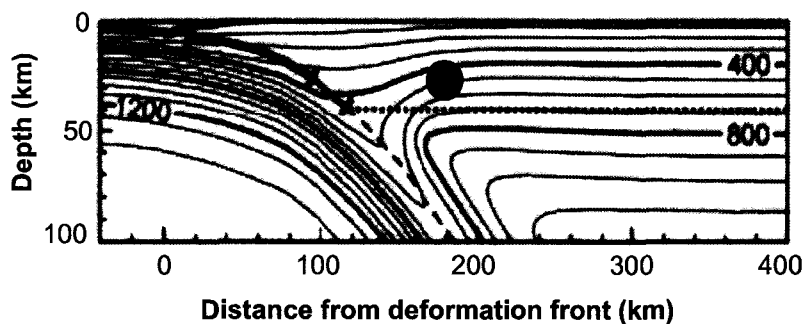


Figure 5.26: A thermal model profile of the Colima-Jalisco subduction zone. This figure was modified from Currie et al. (2002). The green circle is located near the deep low-velocity zone imaged by the tomographic inversion.

velocity variations to calculated temperatures for a depth slice at 25 km, assuming a background temperature of 500°C and the observed velocity perturbations follow the  $-0.5 \text{ m/s/}^\circ\text{C}$  relationship (Anderson et al., 1992, Isaak, 1992).

Any effects of partial melt are harder to quantify due to a strong dependence on melt geometry. Laboratory work has placed a lower limit on the  $V_p$  reduction at 3.6% per 1% partial melt for upper mantle compositions for an ellipse-shaped melt (Hammond and Humphreys, 2000). Given the large volume of the low-velocity zone and the relatively small velocity anomaly, it is unlikely that partial melt is playing a major role. Compositional variations may also play a small role in velocity variations. Nevertheless, uncertainties in the velocity structure due to both partial melt and composition, however limited, need to be considered, and even in small amounts could account for 50% (0.1 km/s) of the velocity perturbation. Translating this into error into the temperature estimates yields  $\pm 200^\circ\text{C}$  on the  $900^\circ\text{C}$  estimate.

Temperatures in the  $900\text{-}1000^\circ\text{C}$  agree well with petrological analyses of erupted material at Colima. Savov et al. (2008) showed from pyroxene-rim analysis conducted on 1999-2005 eruption products that melt temperatures for Colima andesite are around  $950^\circ\text{C}$ , suggesting that the entire low-velocity zone imaged is close to the melting temperatures of the eruptive andesite. It is highly unlikely that the entire  $20 \times 20 \times 15 \text{ km}$  volume of the low-velocity zone is due solely to the presence of magma. If the volume was magma, it would be comparable in size with volcanoes such as

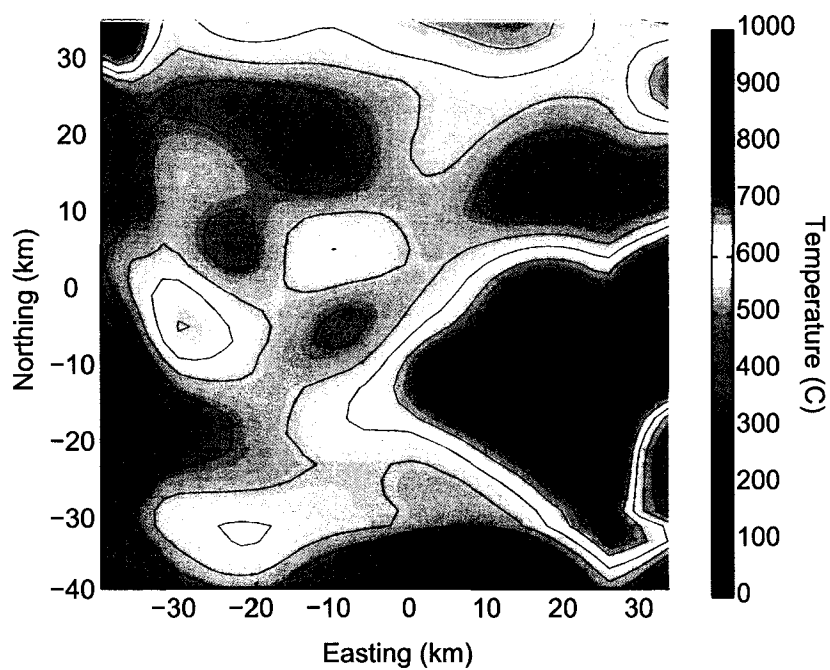


Figure 5.27: P-wave velocities mapped in terms of temperatures at 25 km depth. The initial starting temperature of  $500^{\circ}\text{C}$  was taken from Currie et al. (2002). Inverted variations in velocities were related to temperatures following the relations given in Anderson et al. (1992) and Isaak (1992).

Yellowstone (Smith et al., 2009).

However, the anomaly could be due to increased temperature conditions. The increase over background temperatures could be explained by the presence of limited amounts of magma for thousands of years in a hot zone-type feature described by Annen et al. (2006). The increased temperature conditions would, in general, be more conducive to the silicification of the magma through melting of crustal inputs, as the country rock would already be near its melting temperatures. Petrologic work such as isotope ratio analysis by Carmichael (2002) and Savov et al. (2008) conclude, however that the post-1913 eruptive materials at Colima show little evidence of basement rock assimilation. One explanation for this apparent contradiction is that magma flux through the lower crust is sufficiently fast to minimize the time for assimilation to occur, a conclusion that is consistent with Carmichael (2002).

We therefore conclude that the low-velocity zone running from 15-30 km depth southeast of Colima volcano could be due to an area of increased temperatures. This zone is deeper than magma chambers are generally seen at volcanoes. Over time, the heat from the long-term presence of magma has diffused into the surrounding crustal rock and increased the temperatures substantially above background.

#### Acknowledgments

This work was funded by NSF Grant EAR-0439882. We would like to thank Steve Grand and Jim Ni for supplying the MARS data. We would also like to thank Greg Chavez (PASSCAL/NMT), Silvio de Angelis (UAF/GI), Celso Reyes (UAF/GI), Helena Buurman (UAF/GI) and the Colima Volcano Observatory for assistance in installing and maintaining the stations. A major portion of this work could not have been completed without the tireless effort of Tonatiuh Dominguez at the Colima Volcano Observatory, whose help included, but was not limited to, scouting locations, securing land owner permissions, providing vehicle support, playing the role of local guide, helping install, maintain, and remove the stations, and providing insight, expertise, and discussions regarding the volcano.

## References

- Aki, K., Christoffersson, A., Husebye, E., 1977. Determination of the three-dimensional seismic structure of the lithosphere. *Journal of Geophysical Research* 82 (2), 277–296.
- Allan, J., Nelson, S., Luhr, J., Carmichael, I., Wopat, M., Wallace, P., 1991. Pliocene-recent rifting in SW Mexico and associated volcanism: an exotic terrane in the making. In: Dauphin, J., Simoneit, B. (Eds.), *The Gulf and Peninsular Province of the Californias*. Vol. 47 of American Association of Petroleum Geology Memoir. pp. 425–445.
- Anderson, O., Isaak, D., Oda, H., 1992. High-temperature elastic constant data on minerals relevant to geophysics. *Review of Geophysics* 30, 57–90.
- Annen, C., Blundy, J., Sparks, R., 2006. The genesis of intermediate and silicic magmas in deep crustal hot zones. *Journal of Petrology* 47 (3), 505–539.
- Atherton, M., Petford, N., 1993. Generation of sodium-rich magmas from newly underplated basaltic crust. *Nature* 362, 144–146.
- Carmichael, I., 2002. The andesite aqueduct: perspectives on the evolution of intermediate magmatism in west-central (105-99 w) Mexico. *Contributions of Mineralogy and Petrology* 143, 641–663.
- Carmichael, I., Frey, H., Lange, R., Hall, C., 2006. The pleistocene cinder cones surrounding Volcán Colima, Mexico re-visited : eruption ages and volumes, oxidation states, and sulfur content. *Bulletin of Volcanology* 68, 407–419.
- Currie, C., Hyndman, R., Wang, K., Kostoglodov, V., 2002. Thermal models of the Mexico subduction zone: Implications for the megathrust seismogenic zone. *Journal of Geophysical Research* 107 (B12).
- Davies, J., Stevenson, D., 1992. Physical model of source region of subduction zone volcanics. *Journal of Geophysical Research* 97, 2037–2070.

- DeMets, C., Stein, S., 1990. Present-day kinematics of the Rivera plate and implications for tectonics of southwestern Mexico. *Journal of Geophysical Research* 95, 21,931–21,948.
- DeMets, C., Wilson, D., 1997. Relative motions of the Pacific, Rivera, North American, and Cocos plates since 0.78 Ma. *Journal of Geophysical Research* 102 (B2), 2789–2806.
- DeShon, H., Thurber, C., Rowe, C., 2007. High-precision earthquake location and three-dimensional P wave velocity determination at Redoubt Volcano, Alaska. *Journal of Geophysical Research* 112 (B07312).
- Gardine, M., Dominguez, T., West, M., Grand, S., Suhardja, S., 2007. The deep seismic structure of Volcan de Colima, Mexico. *EOS Transactions AGU* 88 (23), Jt. Assem. Suppl. Abstract T51A–02.
- Gonzalez, M. B., Ramirez, J., Navarro, C., 2002. Summary of the historical eruptive activity of Volcan de Colima, Mexico, 1519–2000. *Journal of Volcanology and Geothermal Research* 117, 21–46.
- Grove, T., Elkins-Tanton, L., Parman, S., Chatterjee, N., Müntener, O., Gaetani, G., 2003. Fractional crystallisation and mantle-melting controls on calc-alkaline differentiation trends. *Contributions to Mineralogy and Petrology* 145, 515–533.
- Grove, T., Kinzler, R., 1986. Petrogenesis of andesites. *Annual Review of Earth and Planetary Sciences* 14, 417–454.
- Hammond, W., Humphreys, E., 2000. Upper mantle seismic wave velocity: effects of realistic partial melt geometries. *Journal of Geophysical Research* 105 (B5), 10,975–10,986.
- Husen, S., Smith, R., Waite, G., 2004. Evidence for gas and magmatic sources beneath the Yellowstone volcanic field from seismic tomographic imaging. *Journal of Volcanology and Geothermal Research* 131, 397–410.
- Isaak, D., 1992. High-temperature elasticity of iron-bearing olivines. *Journal of Geophysical Research* 97 (B2), 1871–1885.

- Izbekov, P., Gardner, J., Eichelberger, J., 2004. Comagmatic granophyre and dacite from Karymsky volcanic center, Kamchakta; experimental constraints and magma storage conditions. *Journal of Volcanology and Geothermal Research* 131, 1–18.
- Jödicke, H., Jording, A., Ferrari, L., Flores, J. A., Mezger, K., Rüpke, L., 2006. Fluid release from the subducted Cocos plate and partial melting of the crust deduced from magnetotelluric studies in southern Mexico: Implications for the generation of volcanism and subduction dynamics. *Journal of Geophysical Research* 111 (B09102).
- Jolly, A., Moran, S., McNutt, S., Stone, D., 2007. Three-dimensional P-wave velocity structure derived from local earthquakes at the Katmai group of volcanoes, Alaska. *Journal of Volcanology and Geothermal Research* 159, 326–342.
- Kern, H., Richter, A., 1981. Temperature derivatives of compressional and shear wave velocities in crustal and mantle rocks at 6 kbar confining pressure. *Journal of Geophysics* 49, 47–56.
- Lees, J., 1992. The magma system of Mount St. Helens; non-linear high-resolution P-wave tomography. *Journal of Volcanology and Geothermal Research* 53, 103–116.
- Lees, J., Crosson, R., 1989. Tomographic inversion for three-dimensional velocity structure at Mount St. Helens using earthquake data. *Journal of Geophysical Research* 94, 5716–5728.
- Luhr, J., 2002. Petrology and geochemistry of the 1991 and 1998-1999 lava flows from Volcán de Colima, México: implications for the end of the current eruptive cycle. *Journal of Volcanology and Geothermal Research* 117, 169–194.
- Luhr, J., Carmichael, I., 1980. The Colima volcanic complex, México: Part I, Post-caldera andesites from Volcán Colima. *Contributions to Mineralogy and Petrology* 71, 343–372.
- Menke, W., 1989. *Geophysical Data Analysis: Discrete Inverse Theory*, 2nd Edition. Vol. 45 of International Geophysics Series. Academic Press.
- Menke, W., 2005. Case studies of seismic tomography and earthquake location in a regional context. In: Levander, A., Nolet, G. (Eds.), *Seismic Earth: Array Analysis of Broadband Seismograms*. Vol. 157 of Geophysical Monograph Series. American Geophysical Union, Washington, DC, pp. 7–36.

- Mora, J., Macías, J., Saucedo, R., Orlando, A., Manetti, P., Vaselli, O., 2002. Petrology of the 1998-2000 products of Volcán de Colima, México. *Journal of Volcanology and Geothermal Research* 117, 195–212.
- Nishimoto, S., Ishikawa, M., Arima, M., Yoshida, T., 2005. Laboratory measurements of P-wave velocity in crustal and upper mantle xenoliths from Ichino-megata, NE Japan: ultrabasic hydrous lower crust beneath the NE Honshu arc. *Tectonophysics* 396, 245–259.
- Pardo, M., Suárez, G., 1995. Shape of the subducted Rivera and Cocos plates in southern Mexico: Seismic and tectonic implications. *Journal of Geophysical Research* 100 (B7), 12,357–12,373.
- Power, J., Villaseñor, A., Benz, H., 1998. Seismic image of the Mount Spurr magmatic system. *Bulletin of Volcanology* 60 (1), 27–37.
- Sánchez, J., Núñez-Cornú, F., 2009. Seismicity and stress in a tectonically complex region: the Rivera fracture zone, the Rivera Cocos boundary, and the southwestern Jalisco block, Mexico. *Bulletin of the Seismological Society of America* 99 (5), 2771–2783.
- Savov, I., Luhr, J., Navarro-Ochoa, C., 2008. Petrology and geochemistry of lava and ash erupted from Volcán Colima, Mexico, during 1998-2005. *Journal of Volcanology and Geothermal Research* 174, 241–256.
- Smith, R., Jordan, M., Steinberger, B., Puskas, C., Farrell, J., Waite, G., Husen, S., Chang, W.-L., O'Connell, R., 2009. Geodynamics of the Yellowstone hotspot and mantle plume: seismic and GPS imaging, kinematics, and mantle flow. *Journal of Volcanology and Geothermal Research* 188, 26–56.
- Waite, G., Moran, S., 2009. Vp structure of Mount St. Helens, Washington, USA, imaged with local earthquake tomography. *Journal of Volcanology and Geothermal Research* 182, 113–122.
- Wiens, D., Seama, N., Conder, J., 2006. Mantle structure and flow patterns beneath active back-arc basins inferred from passive seismic and electromagnetic methods. In: Christie, D., Fisher, C., Lee, S.-M., Givens, S. (Eds.), *Interactions Among Physical, Chemical, Biological, and Geological Processes in Back-Arc Spreading Systems*. Vol. 166 of *Geophysical Monograph Series*. American Geophysical Union, Washington, DC, pp. 43–62.

- Yang, T., Grand, S., Wilson, D., Guzman-Speziale, M., Gomez-Gonzalez, J. M., Dominguez, T., Ni, J., 2009. Seismic structure beneath the Rivera subduction zone from finite-frequency seismic tomography. *Journal of Geophysical Research* 114 (B01302).
- Yang, T., Shen, Y., 2005. P-wave velocity structure of the crust and uppermost mantle beneath Iceland from local earthquake tomography. *Earth and Planetary Science Letters* 235, 597–609.
- Zhang, H., Thurber, C., Shelly, D., Ide, S., Beroza, G., Hasegawa, A., 2004. High-resolution subducting-slab structure beneath northern Honshu, Japan, revealed by double-difference tomography. *Geology* 32 (4), 361–364.

## Chapter 6: Summary and concluding remarks

### 6.1 Summary

The previous chapters emphasize how seismology can be used to track magma movement and storage in the crust. A key benefit with using seismology is that, given the right data set, it has the ability to detect magma movement at many different length scales, from the near-surface to the Moho and beyond. Examples given in this thesis range from the deep crust at Colima in Chapter 5, to the shallow crust at Parícutin, and finally near the surface at Fourpeaked.

When studying magma in the upper crust, Chapter 2 gives a quantitative analysis of how the configuration of a seismic network directly influences the ability to detect and locate shallow volcanic earthquakes. Fourpeaked was an interesting example, because the seismicity contained multiple, short-lived bursts of activity spaced months apart, allowing for a snapshot analysis of seismic performance as the network evolved. The addition of multiple measurements of volcanic gas gives stronger support for the conclusion that a singular injection of magma was the most likely culprit for the activity.

Chapter 3 illustrates the difficulties facing many temporary seismic network deployments, namely, the creation of a local earthquake catalog. The automated technique outlined in this chapter has the ability to save countless hours of tedious data processing, and yet can still return quality data. The catalog created in this chapter was used heavily in both Chapters 4 and 5.

At Parícutin, a vigorous swarm of earthquakes, lasting about a month, was detected in the automated location catalog in Chapter 3. Using this data, I discovered a distinct upward migration in the hypocenters and a change in the stress patterns that were indicative of a dike intrusion of magma at depth. Unlike at Fourpeaked, the magma stalled at 5 km depth with no observed surface expression.

Finally, in Chapter 5, the focus shifts to the deep crust. Due to the requirements of a seismic array with a specialized aperture and a high-quality data set, the deep crust has, in general, remained under-studied from a seismic perspective. Using an array specifically deployed for this purpose, I carried out a P-wave travel time tomography study at Colima volcano, Mexico. Results from the study found a low-velocity zone in the lower crust under the volcano. This zone is possibly the result of localized increased temperatures due to the presence of magma, moving up from the mantle

wedge.

## 6.2 Concluding Remarks

With the increasing risk of human exposure to volcanic eruptions, a better understanding of the entire magmatic system under a volcano is needed. The results presented in this thesis are a small step forward towards this goal.

Unexpected eruptions or volcanic unrest at poorly monitored volcanoes are common around the world, such as at Fourpeaked volcano in 2006. While it is financially and logistically unreasonable to seismically monitor every known volcano worldwide, when a volcano of interest begins to show signs of unrest, a plan of attack for deploying a seismic network is often needed. To that end, the study at Fourpeaked illustrates the difference between a network solely designed to detect earthquakes versus one designed to carry out meaningful seismic analyses using the data. Far too often, instruments are rapidly deployed at a volcano without consideration for the ultimate purpose of the network. The study at Fourpeaked is a step towards quantifying the monitoring and research capabilities of a quick-response networks, and can be used as a starting model for networks at other volcanoes.

With notable earthquake swarms occurring every few years, the Michoacán-Guanajuato volcanic field is clearly an active region seismically and volcanically. While the study of one of these swarms using a regional seismic network was able to distinguish a strong temporal pattern in the seismicity indicative of a dike intrusion of magma, the lack of additional geophysical tools limited the robustness of the analysis. Further studies of the area could include merging a local seismic network with geodetic measurements to observe any uplift or subsidence associated with the seismicity. Adding a geodesy data set could help constrain intrusion volumes that seismicity alone cannot accurately constrain.

Working with Colima volcano, with a long history of previous research, presented a rare opportunity to join data from many different fields, including local and regional seismology, petrology, geochemistry, remote sensing, and geology, to further our understanding of a prodigious volcanic center. Nevertheless, further work, especially studying the lower crust with seismology, is needed in order to better grasp when, where, and why volcanoes erupt in the ways that they do.